12-2018

Development and Validation of Hybrid Continuum/Structural Finite Element Model for Evaluating Foot and Ankle Biomechanics

Saif Alrafeek
Western Michigan University, saif952003@yahoo.com

DEVELOPMENT AND VALIDATION OF HYBRID CONTINUUM/STRUCTURAL FINITE ELEMENT MODEL FOR EVALUATING FOOT AND ANKLE BIOMECHANICS

by

Saif Alrafeek

A dissertation submitted to the Graduate College
in partial fulfillment of the requirements
for the degree of Doctor of Philosophy
Mechanical and Aerospace Engineering
Western Michigan University
December 2018

Doctoral Committee:

Peter A. Gustafson, Ph.D., Chair
James R. Jastifer, M.D.
Koorosh Naghshineh, Ph.D
Daniel Kujawski, Ph.D.

ACKNOWLEDGEMENTS

I would like to express my deep and sincere gratitude to my supervisor, Associate Prof. Dr. Peter A. Gustafson, a faculty member at the mechanical engineering department at WMU. His wide knowledge and logical way of thinking have been of great value for me. His understanding, encouraging and personal guidance have provided a good basis for the present dissertation. Also, I am deeply grateful to my co-advisor, M.D. James R. Jastifer, a faculty member at Homer Stryker School of Medicine at WMU and an orthopedic surgeon at Borgess, for his detailed and constructive comments, and for his important support throughout this work. Besides, I would like to acknowledge my dissertation committee members: Dr. Koorosh Naghshineh and Dr. Daniel Kujawski for their enthusiasm to be members in my dissertation committee and for their help through my study. I would like to thank Dr. Gustafson's research lab members for their continuous support. Many thanks to my family (father: consultant engineer Ghazy Faisal Ibrahim Alrafiq, mother: Sahira Faaeq Tawfeeq, sister: Renaa Ghazy Faisal Alrafik, and finally, sister: Zinah Ghazi Faisal Alrafiq) who made sincere efforts to help me morally and logistically leading to this work. Lastly, I would like to thank my sponsors, the Iraqi Ministry of Higher Education and Scientific Research (MoHESR), the Iraqi Cultural Attaché – Washington DC, Homer Striker College of Medicine - WMU, WMU Graduate College and the Department of Mechanical and Aerospace Engineering staff.

Saif Alrafeek

DEVELOPMENT AND VALIDATION OF HYBRID CONTINUUM/STRUCTURAL FINITE ELEMENT MODEL FOR EVALUATING FOOT AND ANKLE BIOMECHANICS

Saif Alrafeek, Ph.D.

Western Michigan University, 2018

Bone is composed of two structures: compact bone and spongy bone. Spongy bone porosity highly affects the strength and the physical endurance of bone to carry loads. Most studies use continuum finite element (FE) approaches to model spongy bone and neglect porosity. Neglecting porosity may not efficiently assist orthopaedic surgeons to treat patients who experience bone physical disability. The purpose of this study is to demonstrate an inexpensive approach that simulates spongy bone with more accurate capturing of porosity and less requirements of bone information. The approach is developed through investigating the mechanical characteristics of spongy bone; that is, by creating and analyzing a structural FE model composed of stochastically oriented structural elements or "beams". Each beam element represents a trabecula. In addition, this study investigates the experimental complex biomechanics of foot and ankle bones loaded in eversion/inversion. Further, this study provides a structural-anatomical description that explains the effect of subtalar joint anatomy and screw constructs on its torsional rigidity.

TABLE OF CONTENTS

Table of Content—Continued

CHAPTER

Table of Content—Continued

CHAPTER

Table of Content—Continued

LIST OF TABLES

LIST OF FIGURES

List of Figures—Continued

List of Figures—Continued

CHAPTER I

INTRODUCTION

1.1 Biomechanics of foot and ankle

The human foot and ankle is crucial for locomotion and is one of the most complex structures of the human body. The main significant function of foot and ankle is to aid balance by carrying body loads to the ground while adapting to uneven surfaces. The human foot and ankle is an intricate structure and is made from a number of bones and joints [1], see Figure 1. The key movements of the ankle joint complex are plantarflexion/dorsiflexion, abduction/adduction and inversion/eversion, see Figure 2. Plantarflexion/dorsiflexion movement occurs in the sagittal plane, abduction/adduction movement occurs in the transverse plane and inversion-eversion movement occurs in the frontal plane [2], Figure 2. Subsequently, the ankle joint mainly has three axes of rotation (1) plantarflexion/dorsiflexion axis of rotation (2) abduction/adduction axis of rotation "transverse axis of rotation" (3) inversion/eversion axis of rotation. Combinations of these motions across the subtalar and other joint create three dimensional motions called supination and pronation of the foot and ankle, Figure 2. The subtalar joint is one of those joints of the foot and ankle. The subtalar joint is a distinct segment of this study. From geometry stand-point, the subtalar joint is challenging to study because there are few external landmarks in vivo. Generally, the subtalar joint is composed of two bones (talus and calcaneus) [1], Figure 3. The subtalar joint is a primary focus of this work and is the primary source of inversion/eversion motion. Also, subtalar joint cartilage between talus and calcaneus

may be damaged due several reasons, e.g., traumas, injuries and cartilage stiffening over time. Subtalar joint fusion can treat cartilage damage to eliminate pain.

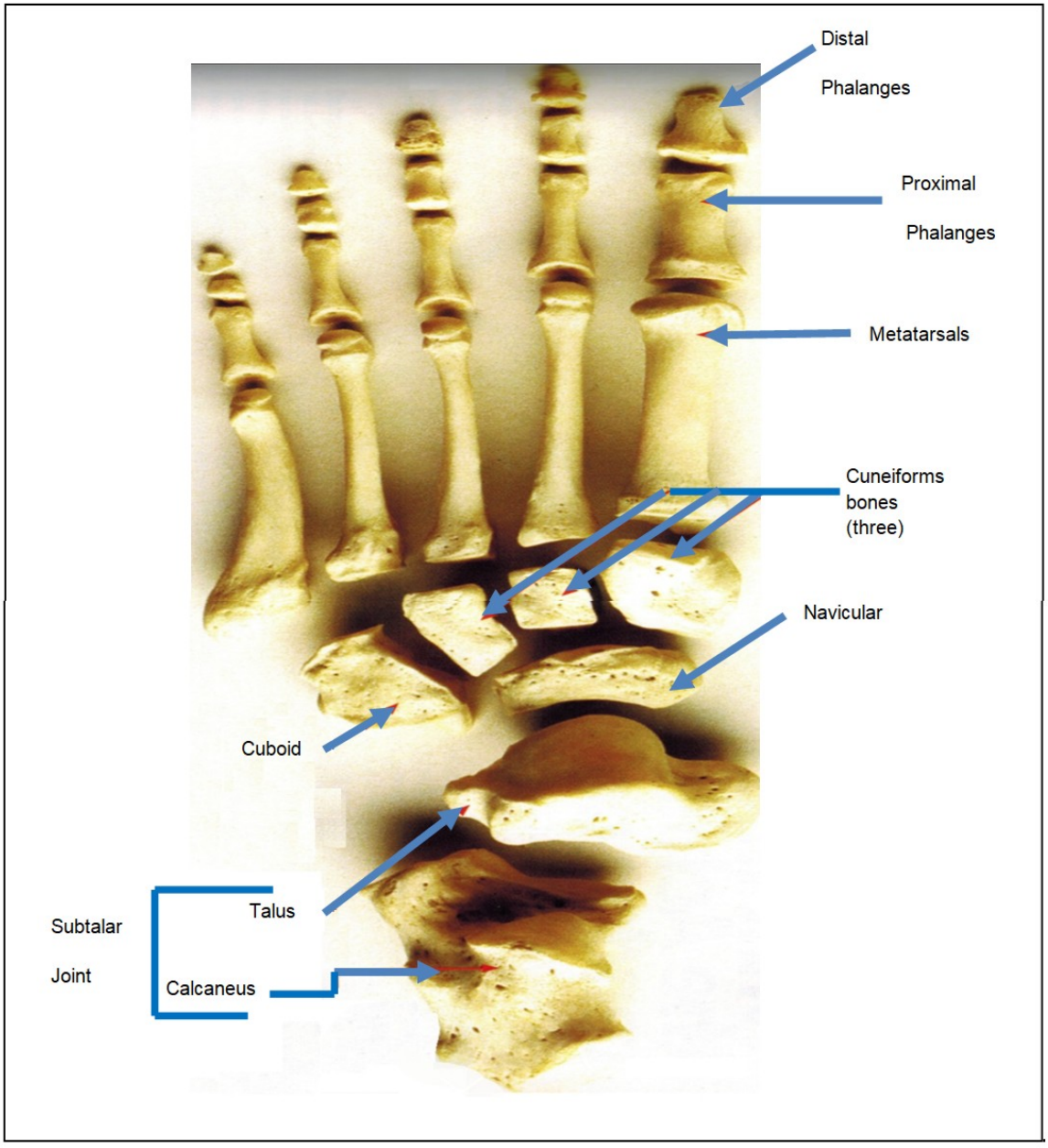

Figure 1: Bones of the foot [1]

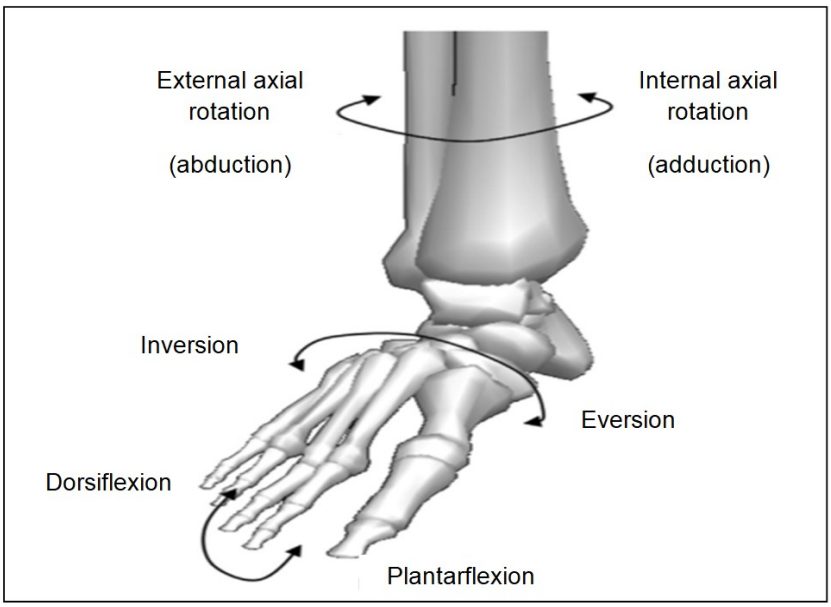

Figure 2: Illustrative diagram relative motions of the ankle joint complex [2]

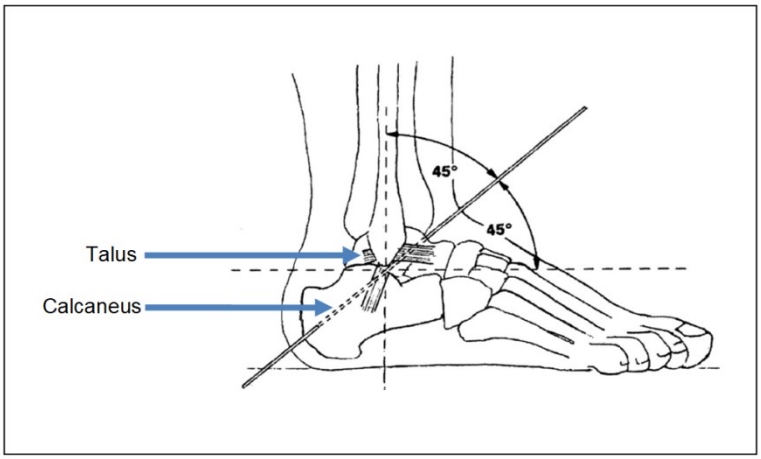

Figure 3: Ankle and foot / subtalar joint [3]

The Finite Element (FE) model that is discussed in a later chapter can be utilized to model complete skeletal bony parts including foot and ankle. Foot and ankle was chosen to be modeled, specifically, the subtalar joint. That is because it is of interest to the direct collaborators of the current study while also providing an appropriate test bed for the analytical techniques.

1.2 Bones structure

The internal structure of bone affects its bulk mechanical behavior. Bone can be described as a hierarchical composite. At the macrostructural scale, bone is composed of two structural types: cortical bone and trabecular bone. Cortical bone is also known as compact bone or dense bone. Trabecular bone is also known as cancellous bone or spongy bone. Generally, cortical bone surrounds trabecular bone. Trabecular bone has a high porosity [4], Figure 4.

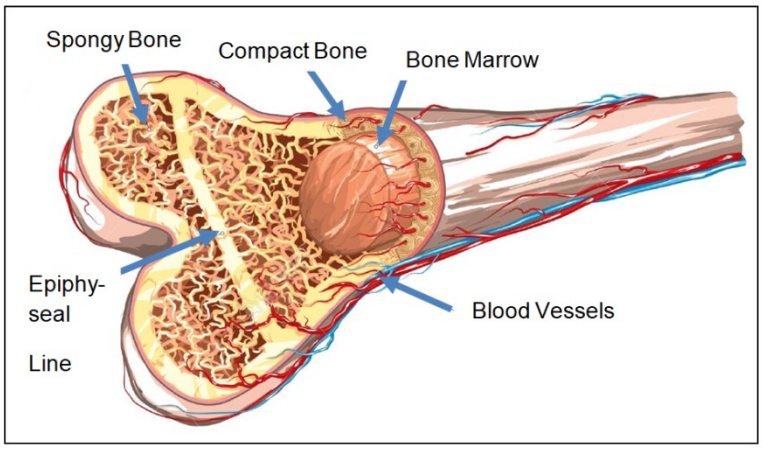

Figure 4**:** Long bone structure [5]

At micro-scale, cortical bone is primarily composed of a secondary cylindrical-shaped unit called osteons; while trabecular bone is composed of trabeculae, Figure 5. Trabecular bone

has a porosity that varies from forty percent to more than ninety percent. Trabecular bone consists of a three-dimensional network structure mainly composed of rod-shaped and plate-shaped fundamental units named “trabeculae”, Figure 6 and Figure 7.

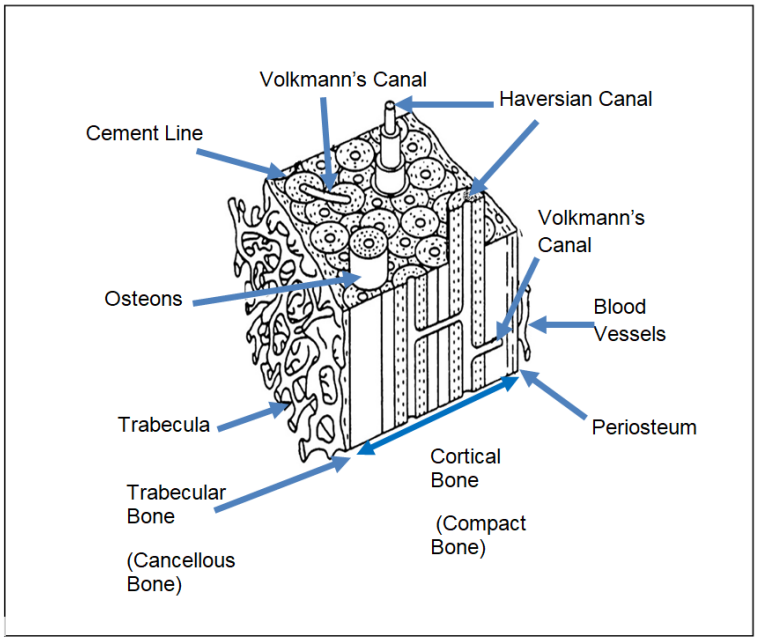

Figure 5: Schematic illustration of bone [6]

The micro-structure of both cortical and trabecular bones determines the gross mechanical properties of the bulk bone tissue [4]. If any changes happen in the micro-structure, that may affect bone total strength. Trabecular bone is highly affected by those changes; that is due to the high porosity of trabecular bone.

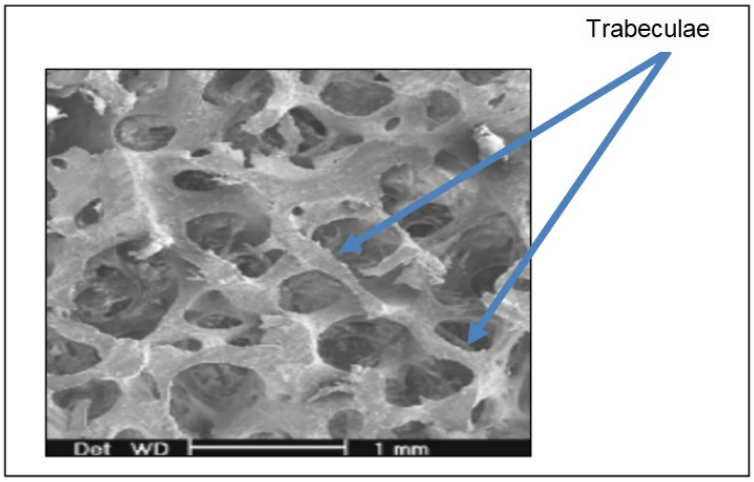

Figure 6: Micrographs of a bovine trabecular bone [7]

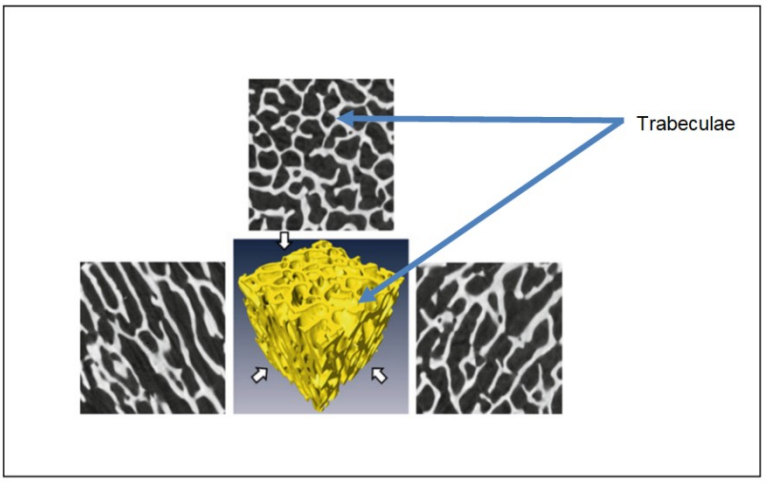

Figure 7: 3D-CT image of cancellous bone [6]

For instance, aging is one of the reasons that cause some changes in bones micro-structure. Bone fracture can happen due to aging. Age-related bone fractures are becoming a common health issue; about 1.5 million fractures are reported every year in the United States. The rate of fractures healing and their cost could highly increase in the near future [8]; because

most of the details of studying the mechanics of bones are still not promising . Thus, studying the mechanics of bone micro-structure and analyzing the structure effects on bone cross properties is advantageous to orthopeadic surgery community and public health.

Finite Element Analysis (FEA) is a computational tool for solving problems of engineering and mathematical physics. FEA has become a powerful tool for structural analysis typical problems [9]. Miller, 1979 [10] started to use FEA in the area of orthopaedic biomechanics. FEA was used to primarily determine stresses in human bones. Huiskes and Chao, 1983 [10] used FE analysis as a possible tool for addressing problems in orthopedics and other clinical applications. However, (Yin, 1985 [10]) identified a gap between the biomechanical models, which could be solved by the FE methods, and the clinical applications. The question was whether the FE method could aid the patients to reach optimal healing. Therefore, this significant difficulty played a crucial role in establishing collaboration between engineers and medical researchers. Other studies distinguished the lack of the bone definite three dimensional (3D) geometries, the bone material properties, and the loading conditions. For this reason, the FE method was accessible but the required input data were unavailable [11].

Access to computed tomography (CT) provided motivation for the generation of anatomy based FE models of various bone types through the 90's. Research on bone modeling utilizing the FE method has expanded during the past decade (2000–2010), Figure 8. Moreover, the increase in computer capabilities and processing speed enriched model validation [11]. Over the last ten years, developers have conducted research studies on modeling hierarchical materials. Hierarchical materials are complex and challenging to analysis. Therefore, investigators have been focusing on conducting research on such materials, e.g. bones.

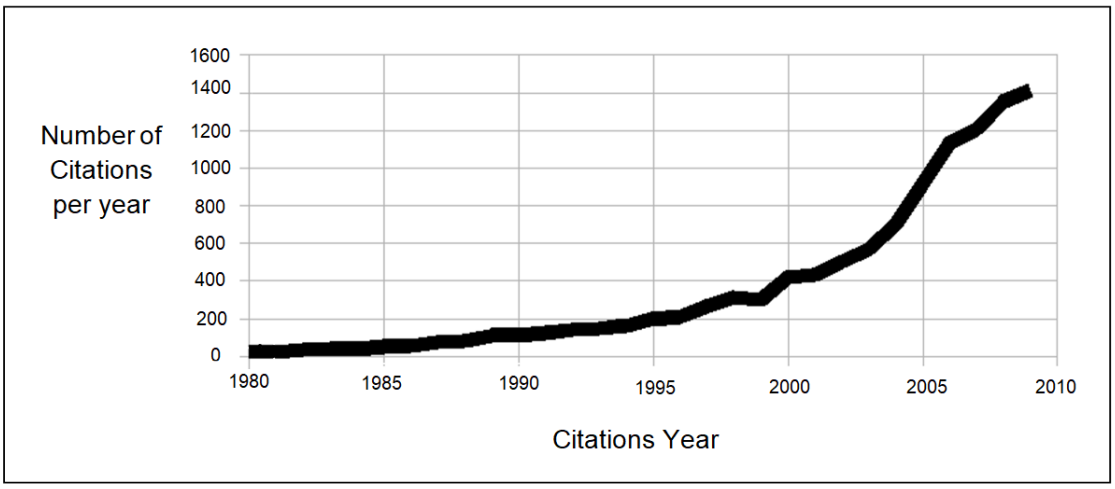

Figure 8: Published studies utilizing finite element analysis as a research tool (1980-2009) [10]

1.2.1 Trabecular bone FE simulation

Researchers have been extensively using classical continuum FE techniques in simulating trabecular bone structure. Classical continuum FE models cannot replicate the size effect commonly observed in micro-scale [12]. Classical continuum FE methods highly depend on medical images (CT / MRI) information. Classical continuum FE techniques include microscopic and macroscopic continuum FE methods:

1- The homogenized continuum FEA (macroscopic).

2- The high-resolution continuum micro FEA (microscopic).

3- Unit cell repetition and scaffolding FEA (microscopic).

Figure 9 illustrates the phenomena beyond the classical continuum FE models. Homogenized continuum models (Classical continuum theory) are the simplest continuum model and cannot incorporate micro -structural size effects [7]. The homogenized continuum FEA method does not consider the concept that demonstrates that the trabecular bone is a network of

trabeculae. Therefore, homogenized FE models do not fully simulate bone micro-structure and that can affect the bulk mechanics representation of bone, Figure 10.

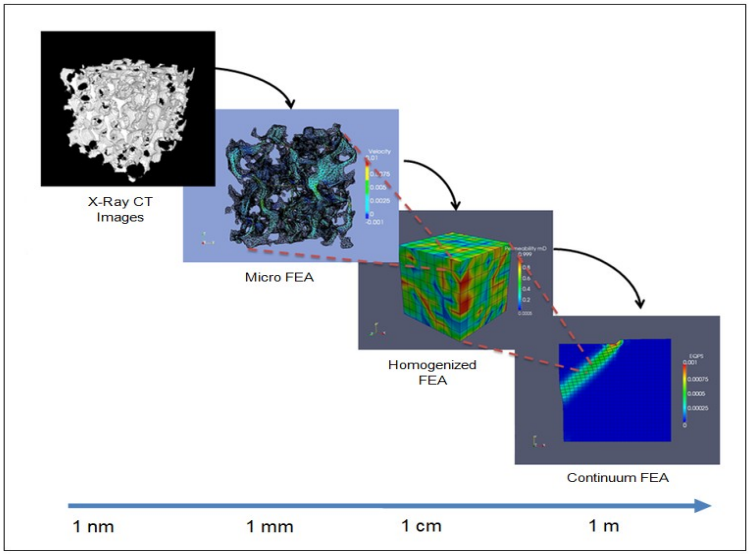

Figure 9: Homogenized FEA versus micro FEA [13]

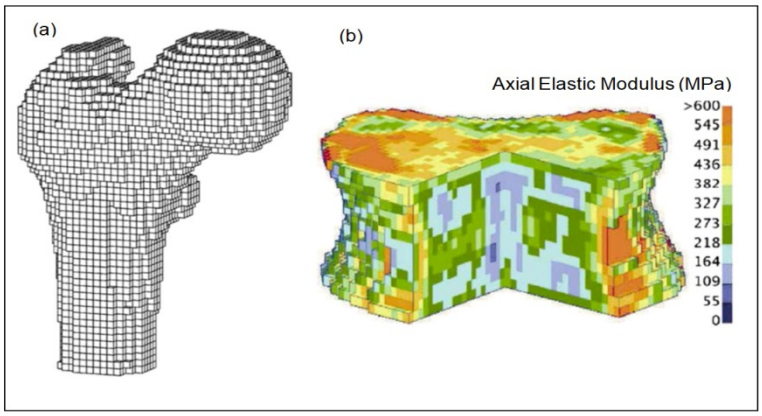

Figure 10: A typical mesh for a macro-scale FE model generated from a CT images, of (a) femur and (b) vertebra [7]

As an alternative, the high-resolution continuum micro FEA method can be used. It involves constructing a detailed μFE model that incorporates all the characters of the local

structure of the trabeculae in micro-scale, Figure 6. This helps to account all micro-structural effects easily. However, the micro FEA can be a highly time-consuming method [7]. Creating continuum micro-FEA at the level of trabecula is expensive and requires further details of trabecular bone micro-geometry , Figure 11. Furthermore, these details change per each patient. Creating models over large volumes is difficult. In addition, there are still no published studies using this method that can be adjusted for a parameterized sensitivity study.

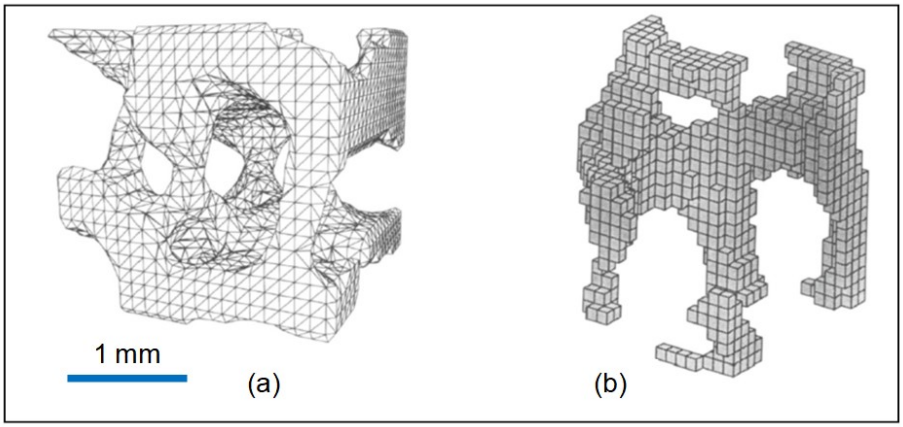

Figure 11: μFE analysis of trabecular structures: (a) tetrahedral meshing, and (b) hexahedral “brick” element meshing

Because trabecular bone has a high porosity, the most commonly used continuum FE methods do not provide a good representation of the trabecular bone network. Hence, porosity and structural anisotropy are not fully incorporated. There is a characteristic structure in trabecular bone architecture that is strongly linked to the bone mechanical function. Considering this structure may help to obtain optimal biomechanical modeling. In the region of a small volume fraction, the majority of the trabecular structure is rod shaped trabeculae. While in the region of high volume density, there are plate shaped trabeculae. In this way, a cell structure

model can investigate the mechanical properties of trabecular bone architecture. Several cell models that characterize the geometrical structure of cancellous bone are made of rod and plate units [6], Figure 12. A model for spongy bone with distinct trabecular structure could be achieved by creating a three-dimensional continuum lattice. For instance, a study (Adachi, T. 1999 [14]) proposed a three-dimensional continuum lattice, that was composed of a distinct arrangement of linear elastic bar elements rigidly interconnected to each other, Figure 13. The model in this study was an analytical model created based on the couple stress theory [14]. On the other hand, the bar elements were repeated periodically, Figure 13; element repetition did represent the corresponding trabecular bone structure. In sum, most classic models of entire bones do not consider trabecular geometry and represent bone as a non-porous structure. Also, the lattice models do not provide a good distribution and biasing of trabecular bone structure. To overcome this pitfall, non-continuum method is proposed in this dissertation.

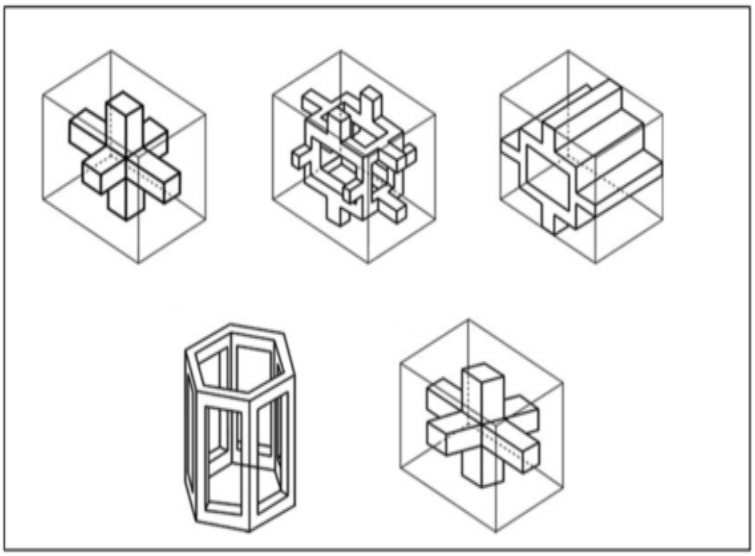

Figure 12: Typical unit cells for structural model of trabecular architecture [6]

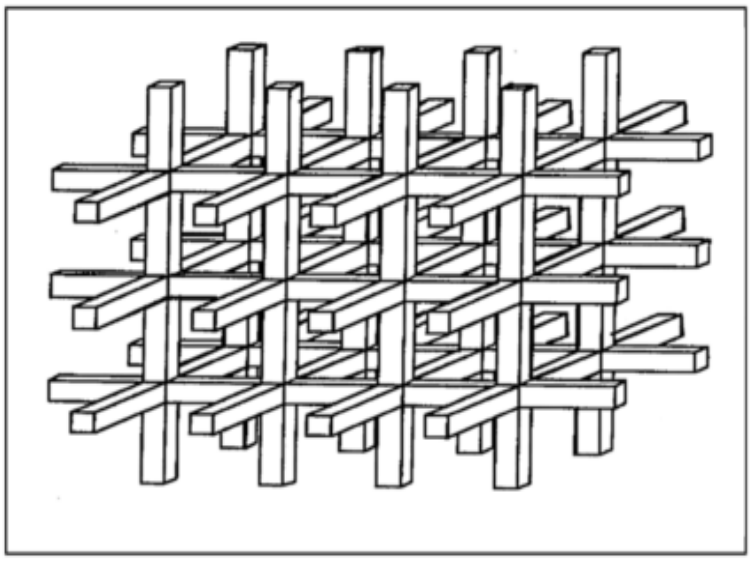

Figure 13: A three dimensional lattice continuum of spongy bone [14]

1.2.2 Cortical / Trabecular bone FE simulation

A number of studies modeled trabecular bone separately. Modeling the behavior of completely human bone including trabeculae requires information about cortical / trabecular regions interface. Overall, continuum FE methods can adequately represent cortical bone; while non-continuum FE methods may be employed to simulate trabecular bone. Non-continuum FE methods, i.e. structural FE, may give a good representation of bone; because structural FE may present enough details of trabecular bone micro-structure. A non-continuum FE method is proposed in this dissertation. Thus, a combination of the continuum and structural FE methods may help together to simulate the entire bone. Such methods may be called FE hybrid continuum/structural methods. This dissertation may address such hybrid model. The hybrid model reduces the gap between the homogenization continuum method that is applied to macro-

scale and the micro FE method that is applied directly to micro-scale [7], Figure 14. A hybrid model can employ multiscale method to model cortical bone (macroscale) and trabecular bone (microscale) together as a cohesive bony tissue unit.

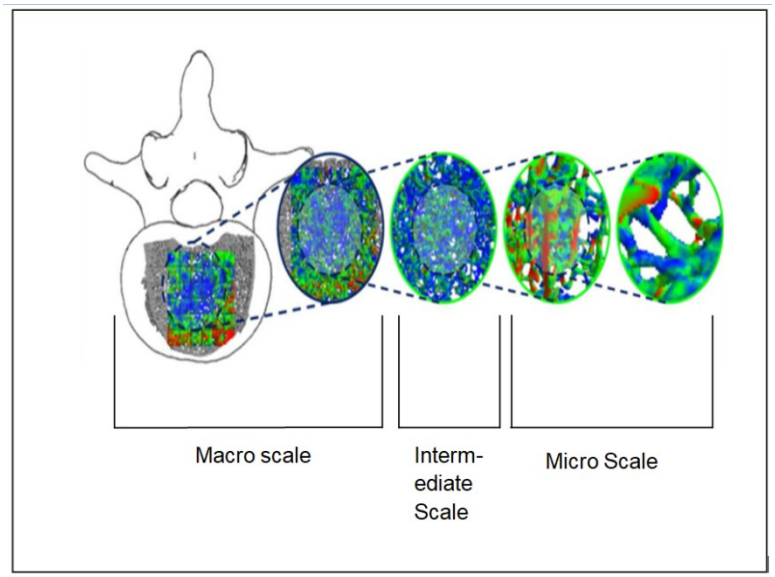

Figure 14: Continuous multiscale approach: macro-scale, intermediate scales and micro-scale levels [7]

1.3 Dissertation objective and layout

This study investigates the complex biomechanics of foot and ankle bones by conducting experimentation. Also, the current work demonstrates the simulation of spongy bone with less dependency on medical images, fewer meshing features and more accurate capturing of spongy bone porosity. The method was developed through investigating the mechanical characteristics of spongy bone; that is by creating and analyzing a structural FE model composed of

stochastically oriented structural elements "beams". The dissertation chapters can be succinctly summarized as follows:

- Chapter 1: presents brief backgrounds about foot-ankle (anatomy and biomechanics), bone anatomy, bone mechanical structures, and FE methods of modeling bony structures.
- Chapter 2: presents cohesive state-of-the-art literature of foot-ankle biomechanics and FE methods to modeling bone as mechanical structures.
- Chapter 3: gives details about experimental setup of foot-ankle biomechanical testing. Also, it presents a structural-anatomical description of subtalar joint.
- Chapter 4: describes the methods and results of a developed FE technique to modeling spongy bone.
- Chapter 5: describes the future work of development of FE methods to modeling bone tissue. Also, it presents some prospective future developments of the dissertation.

1.4 Publications related to this dissertation

Journals:

1- Saif Alrafeek, James R Jastifer, and Peter A Gustafson. “A Stochastic Structural Finite Element Method for Simulating Trabecular Bone.” , ASME, Journal of Biomechanical Engineering (2018). TO BE SUBMITTED SOON.

2- James R Jastifer, Saif Alrafeek, Peter Howard, Peter A Gustafson, and Michael J Coughlin. “Biomechanical Evaluation of Strength and Stiffness of Subtalar Joint Arthrodesis Screw Constructs.”, American Society of foot and ankle, Foot & ankle international 37.4 (2016), pp. 419–426. PUBLISHED [15].

Conference technical papers:

3- Saif Alrafeek, James R. Jastifer and Peter A Gustafson. “A Stochastic Structural Finite Element Model For Trabecular Bone and Other Structural Foams.” In: ASC 33rd Annual Technical Conference, 18th US-Japan Conference on Composite Materials, ASTM Committee D30 Meeting. Seattle, Washington, Sept. 2018. PUBLISHED [16].

4- Saif Alrafeek, James R. Jastifer and Peter A Gustafson. “A Stochastic Finite Element Model For Simulating Trabecular Bone.” In: ASME 2018 International Mechanical Engineering Congress & Exposition IMECE2018, Pittsburgh, Pennsylvania, Nov. 2018. PUBLISHED.

Conference podiums:

5- Saif Alrafeek, James R Jastifer, and Peter A Gustafson. “A Stochastic Finite Element Method for Simulating Patient Specific Trabecular Bone.” In: 36thAnnual Kalamazoo Community Medical and Health Sciences Research Day. May 2018.

6- Saif Alrafeek and Peter A Gustafson. “A Stochastically and Biomechanically Accurate Finite Element Approach for Patient Specific Modeling of Cancellous Bone.” In: 35th Annual Kalamazoo Community Medical and Health Sciences Research Day. May 2017.

7- Saif Alrafeek, James R Jastifer, and Peter A Gustafson. “Development a Structural Finite Element Model of Trabecular Bone.” In: 2017 Midwest Regional Meeting of the American Society of Biomechanics. Feb 23–24, 2017. Grand Valley State University, Feb. 2017.

8- Saif Alrafeek, James R Jastifer, Peter Howard, and Peter A Gustafson. “The Influence of Screw Placement in Subtalar Joint Arthrodesis.” In: 33st Annual Kalamazoo Community Medical and Health Sciences Research Day. May 2015.

Conference posters:

9- Saif Alrafeek, Peter A Gustafson, and James R Jastifer. “A Stochastic Structural Finite Element Model for Trabecular Bone.” In: Summer Biomechanics, Bioengineering, and Biotransport Conference (SB3C), Dublin, Ireland, July 2018.

10- Saif Alrafeek, James R Jastifer, and Peter A Gustafson. “Development of a Structural Finite Element Model of Cancellous Bone.” In: American Society of Biomechanics East Coast Meeting. Poster: April 20–21, 2018; PennState Berks,Reading, PA, USA. Apr. 2018.

11- Saif Alrafeek, Peter A Gustafson, and James R Jastifer. “Development of Stochastic Structural Finite Element Model for Trabecular Bone.” In: Summer Biomechanics, Bioengineering, and Biotransport Conference (SB3C), P139, Tucson, Arizona, 2017.

CHAPTER II

LITERATURE REVIEW

2.1 Introduction

The foot and ankle complex provides an important function permitting efficient bipedal gait. Trauma and degeneration of the joints in the ankle significantly hampers human mobility. Hence, foot and ankle biomechanics have been studied for many years. Early work started in 1935 about foot and ankle. Researchers started making an accurate comparison between the method of function of the chimpanzee foot and that of man, Elfman and Manter, 1935. Research about foot and ankle has been developing since then. In this chapter, studies about subtalar joint as an important part of foot and ankle are reviewed.

2.2 Studies of FE modeling application in foot and ankle bones

Parr et al. [17] presented Finite Element Analysis (FEA) of a human ankle bone that included trabecular network geometry. A healthy adult human talus was scanned using a micro CT. A 3D model representing the cortical bone and trabecular network was created, see Figure 15. Three load and restraint configurations simulating physiological loadings were applied to each FEM. Tetrahedral elements were employed to mesh the model. The model outcome was compared with results from non-porous models. The findings of this study showed that models that included trabecular geometry were considerably stiffer than non-porous whole bone models; wherein the non-cortical component had the same mass as the trabecular network, suggesting inclusion of trabecular geometry was desirable. The authors concluded that if FEM accuracy

increased, FEM might allow prediction of relationships between cortical and trabecular bone remodelling rates. Yuan et al. [18] investigated the effects on subtalar joint stress distribution after cannulated screw insertion at different positions and directions. A healthy right foot was digitized by radiographs and magnetic resonance imaging (MRI), see Figure 16.

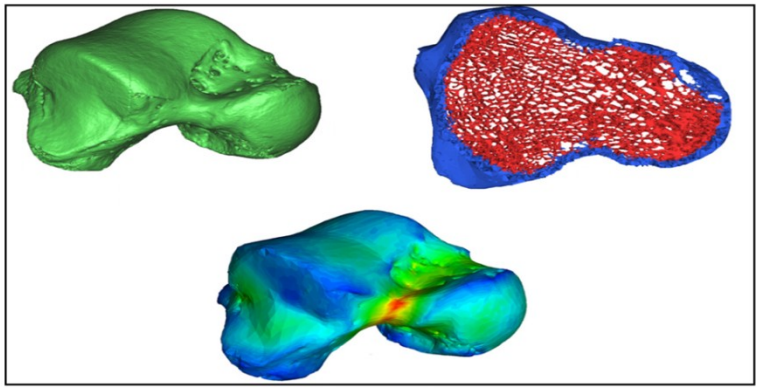

Figure 15: A) Talus CT data (B) Talus FE model (cortical/trabecular bones) (C) Talus FE model (only cortical) [17]

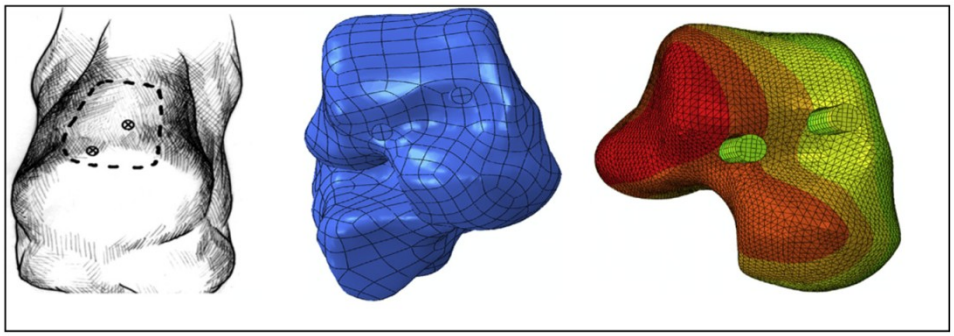

Figure 16: Calcaneal - Talar 3D - FE modeling [18]

The foot (calcaneus and talus) model was created by curve reconstruction. Common size of screws for clinical insertion were considered and assembled in the model. Hexahedral and tetrahedral elements were utilized to mesh talus, calcaneus and the screws. The foot FE model created in this study was continuum and solid. The designed FE model had been ideal and

feasible for screw insertion method. However, the 3D finite element analysis of the internal fixation modes for subtalar fusion in the present study was only a preliminary attempt.

2.3 Foot and ankle biomechanical testing studies

Foot and Ankle FE models can be validated through conducting biomechanical tests and comparing the results of both: computational and experimental outcomes. Conducting experimental biomechanical testing of foot and ankle has been the focus of numerous studies.

Also, subtalar joint fixation and fusion have been the focus through the literature. In this section, a couple of foot and ankle biomechanical studies were reviewed. Chuckpaiwong et al. [19] studied the effect of screws configuration on subtalar joint stiffness using forty-two fresh-frozen cadaveric subtalar joint specimens. Rotation was sequentially applied in two opposing directions to produce internal and external rotation (abduction/adduction) of the talus relative to the calcaneus, see Figure 17. Torsional stiffness in each rotation direction was calculated from the acquired torque. Among the common screw configurations evaluated, double diverging screws achieved the highest torsional stiffness. The results of this biomechanical study might provide guidelines for obtaining optimal torsional loading and fixation technique. Hungerer et al. [20] assessed different screw configurations in terms of their rotational and bending stability in artificial and cadaveric subtalar joint specimens.

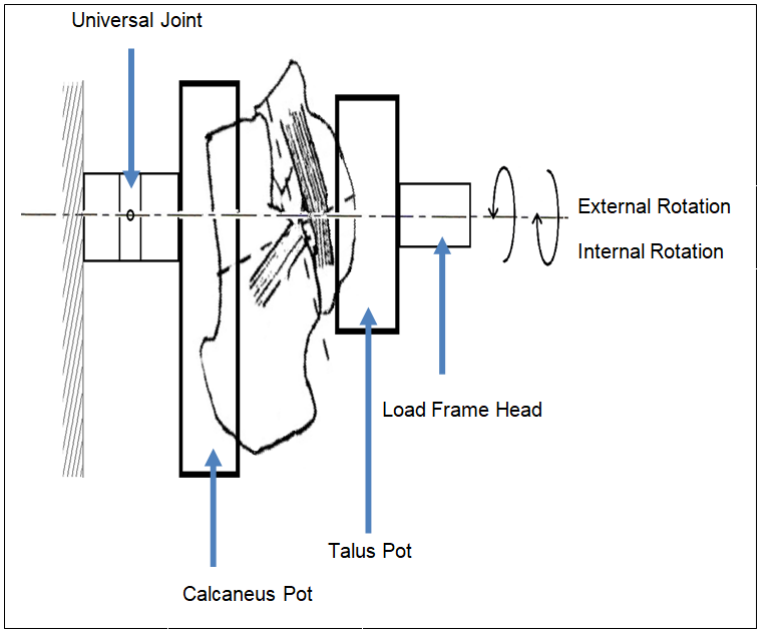

Figure 17: Schematic diagram of Chuckpaiwong study [19]

The fixed subtalar joints were loaded in two different directions: (1) supination and pronation, Figure 18, (2) internal and external rotation (abduction/adduction), Figure 19. The torque rotation was measured at a frequency of 100 Hz. The findings showed that a delta screw configuration provided a significant torsional mechanical advantage for subtalar arthrodesis, Figure 18.

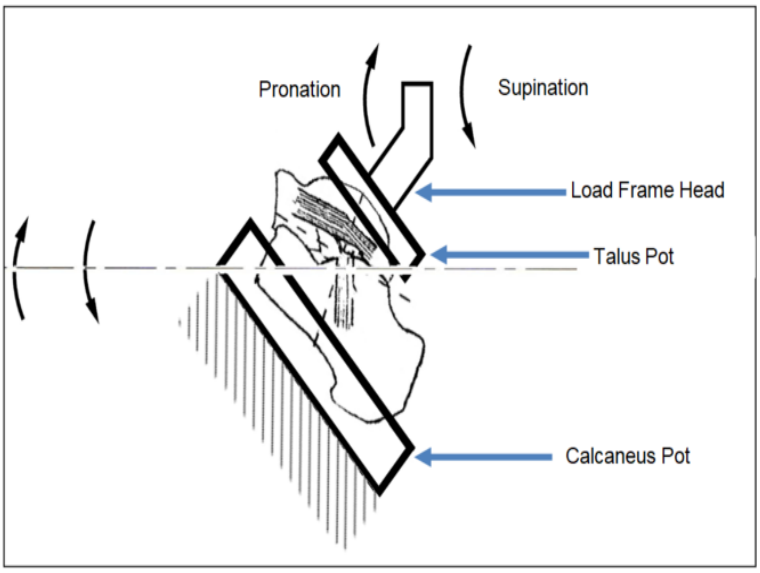

Figure 18: Schematic diagram of Hungerer study [20]

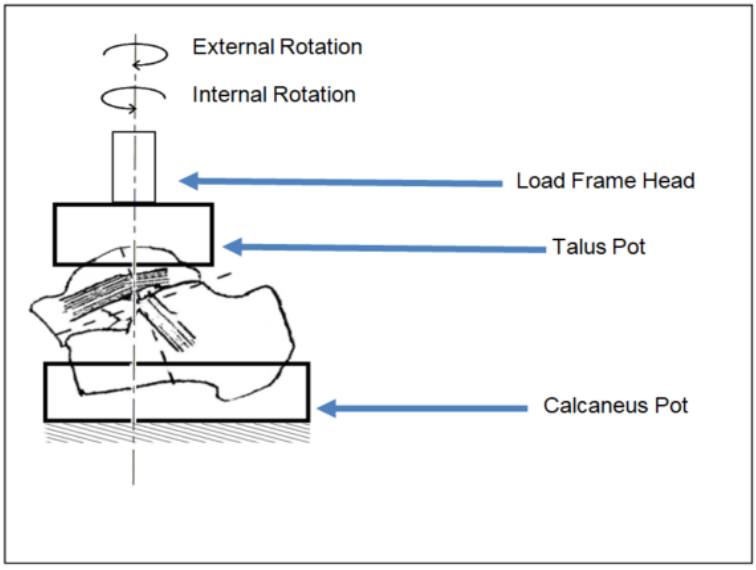

Figure 19: Schematic diagram of Hungerer study [20]

Riedl et al. [21] quantified the torsion resistance of 2-screw and 3-screw subtalar joint fixation. Ten pairs of cadaveric subtalar joints were prepared for arthrodesis. Rotation was applied sequentially in both directions to produce internal and external rotation (abduction/adduction) of the talus relative to the calcaneus, see Figure 20. Torque and rotation were recorded at a sampling rate of 250 Hz throughout each test. The outcome showed that the two screws construct provided a high torsional stiffness compared to three screws construct.

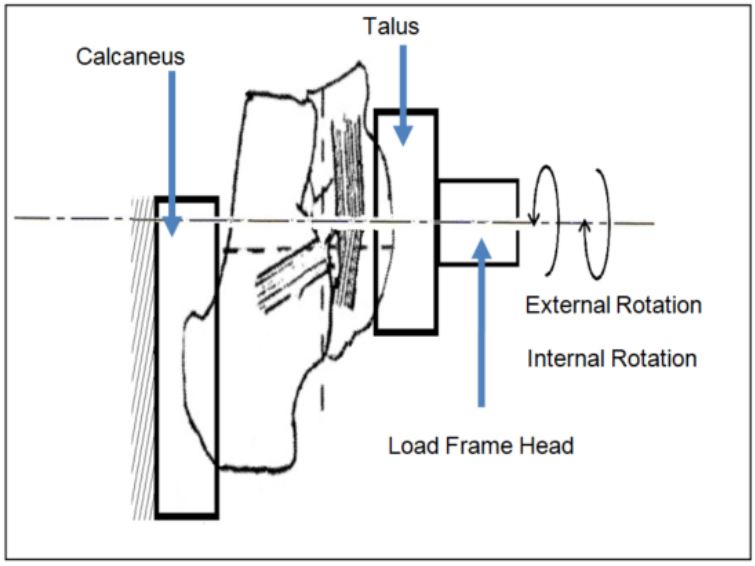

Figure 20: Schematic diagram of Riedl study [21]

2.4 Trabecular bone FE modeling

2.4.1 Continuum micro-FE modeling studies

Complex materials that are composed of hierarchical structure, such as bones, give improved mechanical characteristics different from the individual components. Full understanding of the mechanical behavior of such materials through modeling them is beneficial.

Researchers have been using micro FE methods in analyzing such structures. D. Ulrich et al. [22] investigated the ability of finite element (FE) analyses micro images based of human trabecular bone to provide relevant information about the bone mechanical properties. Three micro CT scan images of femoral head were used. The models were meshed utilizing hexahedral elements. For the coarser resolutions, this resulted in a loss of trabecular connections and a subsequent loss of stiffness. To reduce this effect, a tetrahedral element meshing based on the marching cubes algorithm and modified hexahedron meshing were employed, Figure 21. The calculated mechanical properties could be inaccurate for certain bone morphologies. That is the results can be improved by using correcting factors depending on the bone morphology. Using advanced meshing techniques in this study helped to provide mechanically relevant information, which could not be obtained from methods based only on bone density measurements.

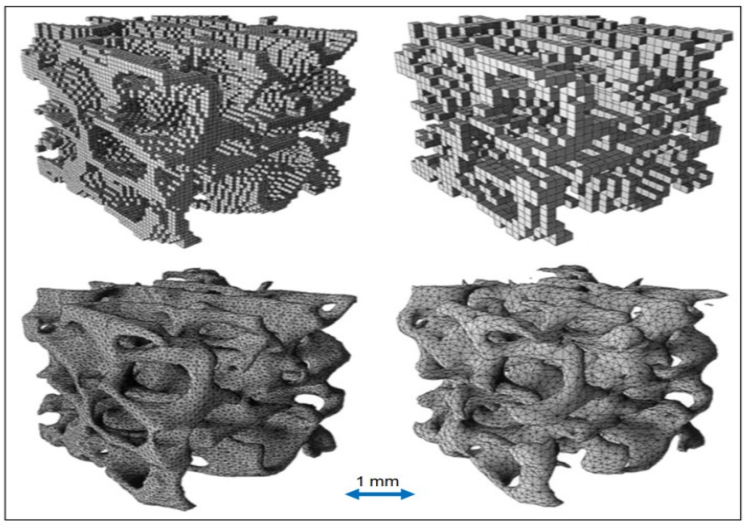

Figure 21: Finite element (FE) models of the femoral head specimen created at a voxel resolution of 84 lm (left) and 168 lm (right) [16]

Vanderoost et al. [23] developed a skeleton-based FE-model in which individual trabeculae were represented by single elements (beams + shells). Skeleton-based method meant the dataset included trabecular bone samples from each skeletal site: calcaneus, lumbar vertebra, iliac crest and femoral head. Samples were scanned using a micro CT. Through skeletonisation and classification, voxel-based models of trabecular bone samples were simplified into a complex structure of rods and plates. Employing the optimized skeletonisation procedure, rod-plate intersections were developed. By relating the skeleton to the original structure each rod and plate were characterized by local morphometric parameters, Figure 22. The resulting model might allow fast assessment of bone mechanical properties and help to analyze the effect of bone microstructure on bone strength. Some of Young moduli values of this study fall within the range of the Young moduli of the current dissertation outcome.

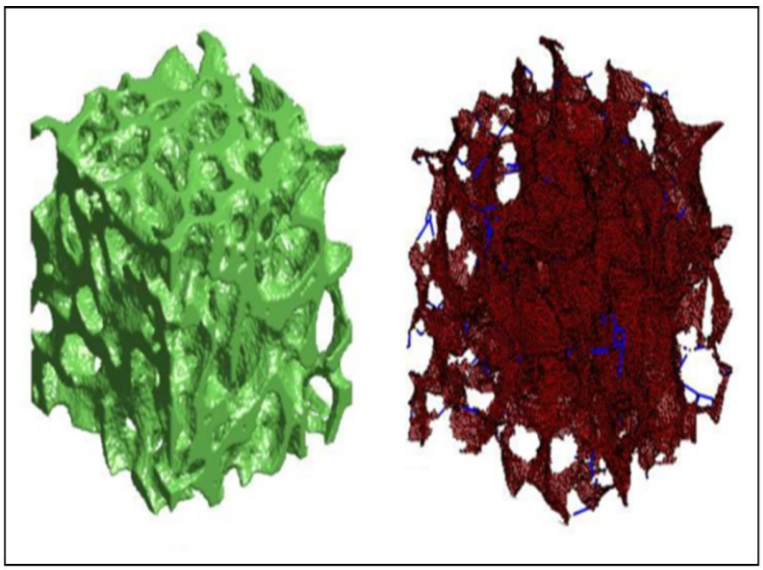

Figure 22: µCT-scan of a femoral trabecular bone sample (left) and its respective skeleton based mesh (right)

Althomali et al. [24] hypothesised that ultrasound computed tomography (UCT) might be combined with micro FEA to predicting the stiffness of bone. Bone samples were 3D-printed from four anatomical sites (femoral head, lumbar spine, calcaneus andiliac crest). Each sample was scanned by X-ray μCT and a UCT system. The models were meshed using tetrahedral and hexahedral elements. This study demonstrated that UCT-FEA based upon quantitative attenuation images provided a comparable estimation of gold standard mechanical-test stiffness of 84% compared to μCT-FEA. The limitation of this study was using 3D-printed replica bone samples that did not represent real human bones. Furthermore, a single material was used to create the samples.

Evans et al. [25] validated a FEM of a rat tibia including trabecular network geometry. That was by testing a material through using microCT images. Also, novel landmark based morphometric approaches was applied to more effectively compare modelled and experimental results. Four node tetrahedral elements were used to mesh the samples. Validation was achieved to an average experimental accuracy of 34.9%. Experimental results showed a good qualitative and quantitative correlation with the experimental data. Average accuracy of 34.9% likely signified that the FEM replicated the microCT results with still higher relative accuracy than possible with 2D validation attempts.

Depalle et al. [26] analyzed the effect of hexahedral elements formation on the assessment of mechanical stress applied to trabeculae bone during a compression test simulation. Trabecular bone geometries were taken from vertebrae. Samples were micro-CT scanned as isotropic voxel size. Micro-CT images were sub-sampled to make a cubic FEM. For each sample, a compression test FEM was created, using either 8-nodes linear hexahedral elements

with full or reduced integration or 20-nodes quadratic hexahedral elements fully integrated. Bone mechanical properties were assumed isotropic, homogenous and linear elastic. This literature found that element formation was almost crucial as element size when evaluating trabecular bone mechanical behavior at trabeculae scale. For this reason, element type should be chosen carefully when evaluating trabecular bone behavior using FEM.

2.4.2 Continuum homogenized and structural FE modeling studies

Schwiedrzik et al. [27] implemented a nonlinear model for trabecular bone as a cohesive-frictional material in a large-scale computational framework and validated the model by comparison micro FE simulations with experimental tests in uniaxial tension and compression. Samples of trabecular were obtained from femur, radius and vertebra. Models were meshed using eight node hexahedral element. A good correspondence of stiffness and yield points between simulations and experiments was found for a wide range of bone volume fraction and degree of anisotropy in both tension and compression.

Goda et al. [28] developed a 2D micropolar continuum model of cancellous bone accounting for the influence of microstructure-related scale effects on the macroscopic effective properties. That was using unit cell of struts (beams). Aiming for the same purpose of this study [28], the authors Goda et al. [29], developed a 3D anisotropic micropolar continuum model of vertebral trabecular bone accounting for the influence of microstructure-related scale effects on the macroscopic effective properties. Vertebral trabecular bone was modeled as a cellular material. That was through the repetition of a unit cell. The unit cell was hexagonal composed of five struts. The micromechanical approach relied on the discrete homogenization technique

considering lattice microrotations as additional degrees of freedom at the microscale. The articulated struts (beams) captured axial, transverse shearing, flexural, and torsional deformations of the cell struts. A finite element model of the local architecture of the trabeculae gave values of the effective moduli that were in satisfactory agreement with the homogenized moduli.

Vaughan et al. [30] presented a three-scale finite element homogenisation scheme. The scheme enabled the prediction of homogenised effective properties of tissue level bone from its fundamental nanoscale constituents of hydroxyapatite mineral crystals and organic collagen proteins. Two independent homogenisation steps were performed on representative volume elements which described the local morphological arrangement of both the nanostructural and microstructural levels. This approach could provide a more accurate description of bone tissue properties in continuum/organ level finite element models by incorporating information regarding tissue structure and composition from advanced imaging techniques.

Ilic et al. [31] presented a method of applying multiscale homogenization FE modeling on cancellous bone. That included converting real bone microstructure to its corresponding RVE. The assumed RVE was consisting of thin walls and marrow core. The process of osteoporosis was simulated by varying the geometrical parameters. Hexahedral elements were used in meshing the geometrical parts. The simulations at the micro level allowed the comparison with experimental results; thus a reliable analysis yielded optimal geometrical parameters.

Tanaka and Adachi [32] developed a 3D lattice continuum as a structural model of cancellous bone with the trabecular architecture of the vertebral body. The model was composed of a discrete system of linear elastic bar elements rigidly interconnected at right angles to each

other. The model was meshed using hexahedral elements consisting of five tetrahedra. The proposed model could be useful to predict the adaptive remodeling of bone phenomenologically. The proposed lattice model was expected to function as a gap-filler between the macroscopic and microscopic levels in remodeling mechanics of cancellous bone.

Vanderoost et al. [33] conducted an extended study of [23]. Vanderoost et al. improved the FE methodology of representing trabecular bone as a micro-computed tomography-based beam model by representing plate-like trabeculae in a way that better reflected their mechanical behavior. That was by improving the intersection regions of beams and plates. Using an optimized skeletonization and meshing algorithm, voxel-based models of trabecular bone samples were simplified into a complex structure of rods and plates. Rod-like and plate-like trabeculae were modeled as beam and shell elements, respectively. The values for the trabecular morphometrical properties, and thus the apparent elastic modulus, were strongly influenced by the way they are calculated. A number of (4 mm x 4 mm x 4 mm) trabecular bone cubes was used in this study. In contrast to earlier skeleton-based beam models [23], the novel beam–shell models predicted elastic modulus values equally well for structures from different skeletal sites. It allowed performing detailed parametric analyses that covered the entire spectrum of trabecular bone microstructures.

Wirth et al. [34] modeled bone as a continuum material and examined how peri-implant strain distribution and load exchange between the implant and bone were influenced by the continuum hypothesis. Micro CT images of human humeral heads were obtained. Discrete trabeculare structures were created by determining bone volume fraction (BV/TV) and direct structural indices; such as the structure model index (SMI), mean trabecular thickness (Tb.Th),

mean trabecular separation (Tb.Sp) and mean trabecular number (Tb.N). The models were generated by direct voxel-to-element conversion ; hexahedral elements were used. For trabecular bone the continuum assumption seemed even more problematic as in contrast to the continuum-like cortical bone. A computational study was conducted as cancellous screws were embedded in continuum and discrete models of trabecular bone. Noticeably, axial loading was imitated. Profound discrepancies in bone-implant stiffness between the discrete and continuum bone models were found. In addition, the load exchange from the screw to the surrounding bone was found to differentiate strictly between the continuum and discrete models, particularly for low-density bone. This literature demonstrated that strain distribution in peri-implant trabecular bone could not be resolved correctly utilizing a continuum bone model. This was true for the bones of low and high densities. Accordingly, finite element analysis could only be used if trabecular bone was represented in adequate details.

Wang et al. [35] constructed plate–rod (PR) finite element (FE) models based on ITS-individual trabecular segementation method of plates and rods. PR FE models were generated for each μCT image and corresponding voxel-based FE models were also generated. Individual trabecular plates and rods were meshed into shell and beam elements, respectively. Human trabecular bone cores from proximal tibia, femoralneck and greater trochanter were scanned by μCT. It was concluded that trabecular plates and rods accurately determined elastic modulus and yield strength of human trabecular bone. Some of Young moduli values of this study fall within the range of the Young moduli of the current work results.

Zhao et al. [36] hypothesized that there existed a commonality in the underlying probabilistic distributions of microstructural features of trabecular bones, whereas the

microstructural differences among individuals are primarily described by a set of scalar parameters. Femoral neck and vertebral body trabecular bone samples were scanned using a CT scan. The number, size, spatial location, and orientation of individual plates and rods in the trabecular bone specimens were determined via volumetric decomposition of 3D μCT images using the Individual Trabecula Segmentation (ITS) technique. This finding suggested that the probabilistic distributions of microstructural features in trabecular bone most likely followed common rules associated with underlying natural design. In addition, the results of this study revealed that the differences in trabecular microstructure among individual bone specimens could be described by a set of scalar parameters that define the number, mean size, and mean spatial arrangement of individual plates and rods in trabecular bone.

2.5 Cortical / trabecular bone FE mutli-scale modeling studies

Podshivalov et al. [37] provided continuous bi-directional transition between macro and micro scales using intermediate scales. The intermediate scales were equivalent to zooming from a dense trabecular structure to an identifiable group of trabeculae, and finally to a singular trabecula. The geometric model preserved the prominent structural features of the material, and the computational model can be solved without requiring extensive parallel computing. High resolution images of vertebra were obtained. The procedure of this study was: (1) reconstructing a 3D mesh (2) converting a 3D mesh into voxels (3) building an octree representation of the 3D volume (4) processing the volumetric model for visualization. This new method closed the gap between the classic homogenization approach that was applied to macro scale models and the

modern micro finite element method that was applied directly to micro scale high resolution models.

Kwon et al. [38] developed multiscale modeling technique to predict mechanical properties of human bone, which utilized the hierarchies of human bone in different length scales from nanoscale to macroscale. This was achieved through incorporating a hierarchy of complex geometries composed of three major materials: hydroxyapatite, collagen and water. The hierarchical structures of bone were hydroxyapatite, tropocollagen, fibril, fiber, lamellar layer, cancellous bone and cortical bone. Collagen was represented by a helical spring model. Fibrils, fibers and lamellar layers were modeled as micro unit cells. Cancellous bone and cortical bone were modeled as laminated composite. It has been concluded that having little information about bone in nanoscale and microscale, a model encompassing the complete hierarchy of bone could be used to help validate assumptions or hypotheses about those structures.

2.6 Shortcomings of existing literature

Studies in the literature [19] [20] [21] have experimentally tested only (adduction / abduction) and (supination / pronation) motions of ankle joint. Eversion / inversion motion of ankle joint has not been tested and modeled yet in the literature. Despite the fact that these studies have made a review of the anatomical and biomechanical aspects of the ankle joint, a structural – anatomical description was not likely provided that could help to demonstrating the relationship among the mechanical stiffness of the joint, the joint anatomical impact and screw configurations.

Most models have not exactly mimicked the anatomical functionality of a natural ankle joint. Therefore, creating a 3D FEA model that covers simulating cortical and trabecular bones of the ankle and foot joint is critical. Studies showed that the provided 3D FEA models of a human ankle and foot are good to some extent [17] [18]. Nonetheless, there are some shortcomings that include considering continuum methods in modeling the trabecular bone with high dependency on medical image information.

It is observed in the literature review that the researchers created the continuum FEA simulations of bone tissue were based on specific structured geometries. These models presented an accepted agreement with the literature outcome developed from certain algorithms and/or experimental work ([22], [23], [24] , [25] and [34]). Nevertheless, creating continuum FEA at micro-scale, the level of trabecula, is expensive and requires details and information on trabecular bone geometry at micro-scale. These details change per each patient. Creating the model at micro-scale is difficult to achieve in an adequate way over the large volumes of whole bones. Moreover, the models cannot be easily adjusted for a parametrized sensitivity study.

Another accepted method that can be utilized is continuum FEA with "homogonized or averaged trabecular properties". However, this method does not account for trabecular bone as a network of trabeculae. That may influence characterizing bulk mechanical properties and failure mechanisms of bones.

The developers in ([22], [33], [26] and [39]), created models depending on medical images, computed tomography scans (CT scans) and some radiation techniques. Those methods do not completely assist in giving detailed information about the true bone morphology. Such models lack the details quality of the bone network during image conversion.

The spongy bone was modeled by making a repetition of a hexagonal unit cell structured from struts connected at different angles. Other shapes of unit-cells were constructed for further accuracy in representing the spongy bone [29] [32]. Also, there were studies that modeled the trabecular bone as rods and plates [23] [35]. The studies used a continuum mesh rather than a discrete mesh to solve the FEA problem. The studies used continuum elements, tetrahedral and hexagonal elements. Other discrete structural elements, such as beams and shells, can be used instead. These elements may provide an adequate characterization of trabecular bone mechanical properties if they are used in a technique that facilitates conducting parametric – sensitivity study. Structural element can be more efficient in representing trabecular bone if they are utilized in a representative volume that contains enough information about trabecular bone, such as stochastic geometries. The downside of using such elements is that they may not capture the true mechanical behavior once the there is lack in geometries information or geometries inaccuracies exist.

The previous work conducted a number of micro FEA methods to facilitate an adequate modeling of the bone [22] [33] [24] [25] [27] [34] [35] [36]. However, these techniques do not aid to capture bone mechanical properties precisely and the characterization output lacks true bone features. The techniques can be handled for further solutions. The initial micro-scale level highly relies on the resolution of the medical images. Thus, high resolution medical images are critical for mimicking the initial micro-scale model. Furthermore, the literature has assumed computational model elastic material properties. Inelastic, plastic, effects of the bone marrow can be considered.

Based on the previous literature, not all ankle joint motions were studied. Also, there was no structural-anatomical description of subtalar joint provided in the literature that explained the impact of anatomical geometry of the joint on its mechanical rigidity. In addition, investigating a structural non-continuum FEA model that simulates trabecular bone is significant to support the literature. The next chapters help to solve some of those difficulties.

2.7 Literature summary

A brief summary of the previous literature is listed in the following tables, Table 1 and Table 2 . The developed methods in this dissertation are highlighted in bold:

Table 1: Foot and ankle biomechanical experiments

Reference	**Targeted ankle motion**	**Sample (type / number)**	**No. of Screws Configurations**	**Structural – Anatomical Description**
Chuckpaiwong et al. [19]	Abduction / Adduction	Cadaveric (42)	1- Single screw (talar neck). 2- Single screw (talar dome). 3- Double parallel screw configuration. 4-Double divergent screw configuration.	N/A
Hungerer et al. [20]	(Abduction / Adduction) and (Supination / pronation)	Cadaveric (18) and synthetic (48)	1-Double divergent screws. 2- Two parallel screws configurations (parallel – counter parallel)	N/A
Riedl et al. [21]	Abduction / Adduction	Cadaveric (20)	1-Double divergent screws. 2- Triple divergent screws.	N/A
[current study] [15]	***Eversion / inversion***	***Synthetic (59)***	***1- Single screw (talar dome)*** ***2- Double parallel screw configuration*** ***3- Double divergent screw configuration***	***Provides a structural – anatomical description***

Table 2: Trabecular bone modeling techniques

Source	Methodology / Element type	Unitcell	Medical image	Special algorithms
D. Ulrich et al. [22]	Continuum micro FE / hexahedral and tetrahedral	no	yes	Marching
Vanderoost et al. [23]	Continuum micro FE / beams and shells	no	yes	Skeletonisation
Depalle et al. [26]	Continuum micro FE / hexahedral	no	yes	no
Schwiedrzik et al. [27]	Continuum homogenized FE / cohesive frictional hexahedral	no	yes	(ABQ-Drucker) and (ABQ-UMAT)
Goda et al. [29]	Continuum homogenized FE / hexahedral	yes	no	Discrete homogenization technique
Ilic et al. [31]	Continuum homogenized micro FE / hexahedral	no	no	Multi scale homogenization
Tanaka et al. [32]	Continuum homogenized structural / beam	yes	no	Couple stress theory
Wirth et al. [34]	Continuum discrete / hexahedral	no	yes	Volume fracture / direct structural indices
Podshivalov et al. [37]	Multi scale / tetrahedral voxels	no	yes	Continuous bi-directional transition
[current study] (trabecular bone)	***Structural FE***	***no***	***no***	***Stochastic method***

CHAPTER III

A BIOMECHANICAL STUDY OF SUBTALAR JOINT ARTHRODESIS TECHNIQUES WITH ANATOMICAL CONSIDERATIONS

3.1 Introduction

The subtalar joint serves to provide the inversion/eversion motion of the foot and ankle complex [2], Figure 2 and Figure 3. In this chapter, the biomechanics of subtalar joint athrodesis is evaluated using experimental quantification of torsional stiffness and strength in response to eversion / inversion loads, Figure 23 and Figure 24. Three screw constructs are compared. Further, the impact of anatomy on the stiffness and strength are considered.

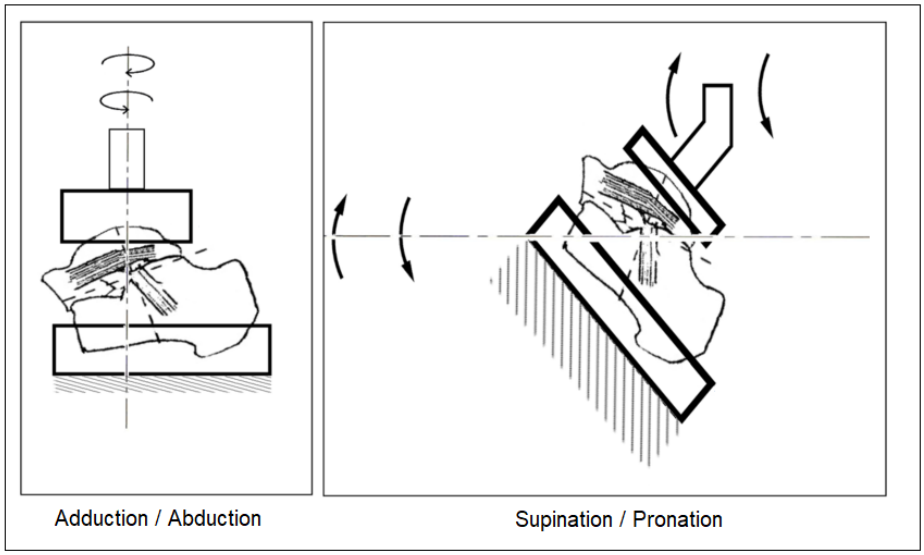

Figure 23: Literature ankle joint motion testing

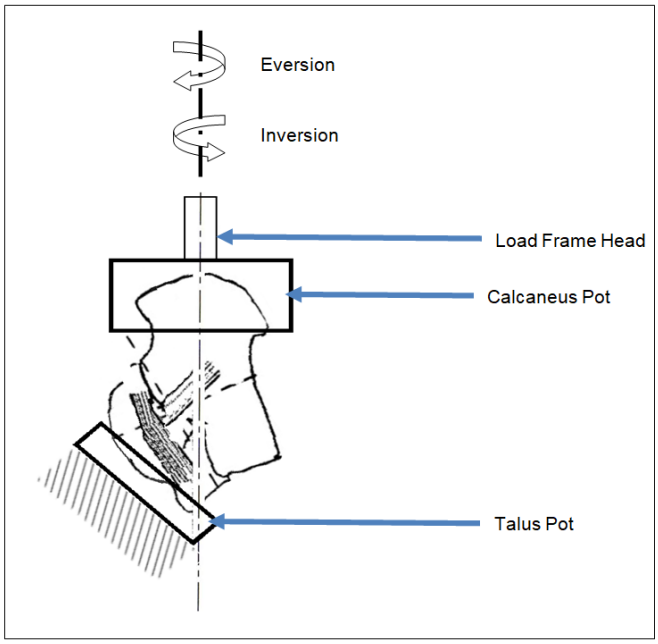

Figure 24: Current work ankle joint motion testing

3.2 Axis of rotation

Motion about the ankle and subtalar joint is difficult to understand. Replicating the axis of rotation and range of motion of the subtalar joint has been a challenge through the literature [3] [40] [41] [42]. The inward rotation of the sole of the foot that results from subtalar joint motion is named inversion, while the reciprocal outward rotation is called eversion [3], Figure 25. The joint axis of rotation for inversion-eversion is replicated in this chapter. From anatomy-wise, subtalar joint axis of rotation for inversion – eversion passes through two landmarks: talar head and calcaneal tuberosity [3] [43], Figure 26. The next section describes the methods of replicating the subtalar joint axis of rotation.

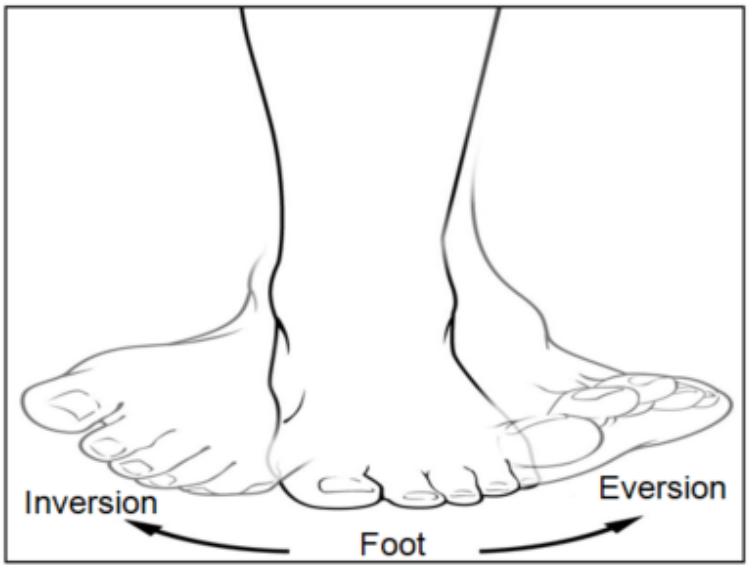

Figure 25: Eversion / inversion of motion [43]

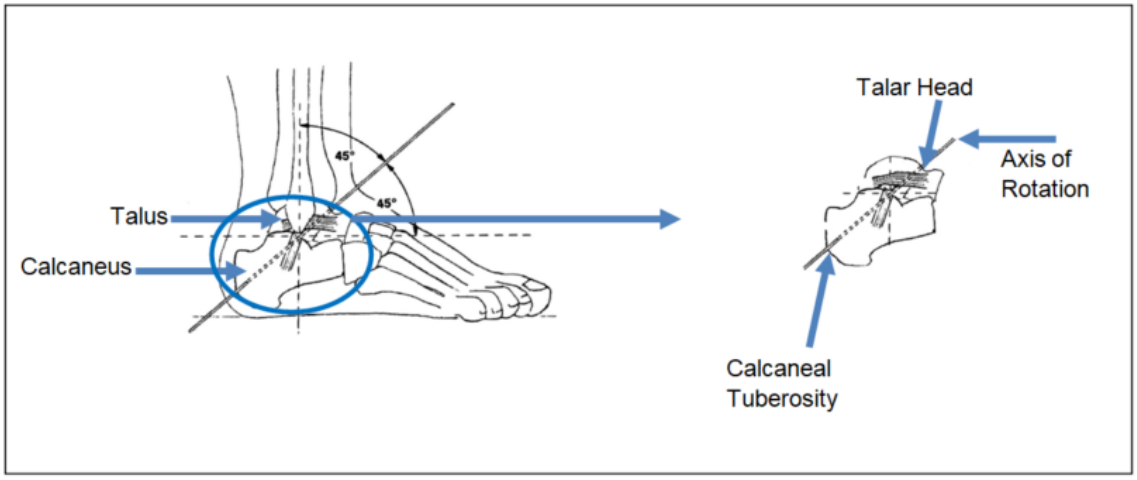

Figure 26: Subtalar joint functional axis relative to the sole of the foot (orientation and landmarks) [3] [43]

3.2.1 Materials

Synthetic calcaneus and talus were used: (calcaneus 1123-1 and talus 1124-1; sawbones, Pacific research laboratories, Vashon Island, Washington, DC, USA). The synthetic specimens contained a cortical shell and a foam cancellous bone surrogate core, Figure 27. The shell and core mechanical properties are listed in Table 3 .

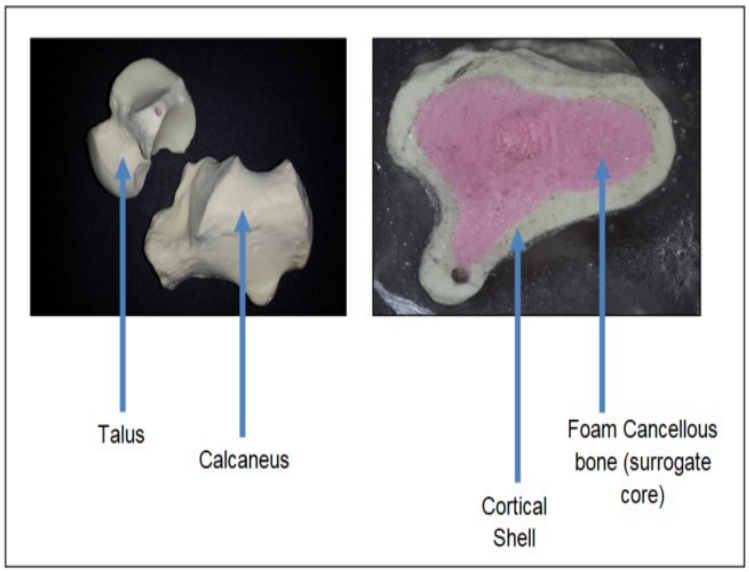

Figure 27: Artificial Calcaneus and Talus specimens

Table 3: Material properties sawbones specimens used

	Strength (ultimate strength / MPa)	**Modulus (Young Modulus / GPa)**	**Poisson's ratio approx.**	**Density (kg/ m3)**
cortical outer layer	8 - 18	0.20 - 0.45	0.3	320 - 480
spongy inner core	1.5 - 3.2	0.038 - 0.081	0.3	130 - 200

The synthetic talus and calcaneus were connected and fixed to each other to construct subtalar joint. Subtalar joint specimens were constructed by a fellowship trained foot and ankle orthopedic surgeon [15], Figure 28.

Figure 28: Subtalar joint construction

The orthopedic surgeon used 7.5 mm cannulated partially threaded screws, Figure 29 and Table 4. They were manufactured from Titanium alloy: Ti-6Al-4V, ISO 5832-3 ASTM F136.Three screw configurations were considered in this study: Double Divergent (DD), Double Parallel (DP) and Single Screw (SS) [15], Figure 30. Having all of that, subtalar joint fixation and fusion have also been the focus of the literature [20] [19] [44].

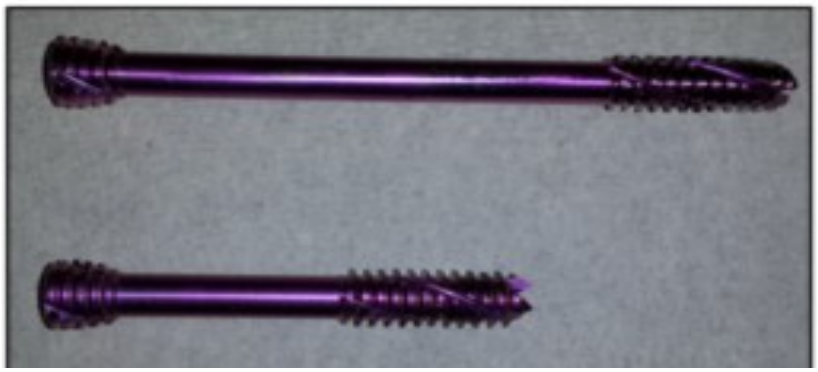

Figure 29: Fixation screws

Table 4: Fixation screws (Integra Extremity Reconstruction, New Jersey, USA)

	Model	diameter	Length
Large	111 785 SND, Qwix Fixation Screw	7.5mm	085 mm
Small	111 755 SND, Qwix Fixation Screw	7.5mm	055 mm

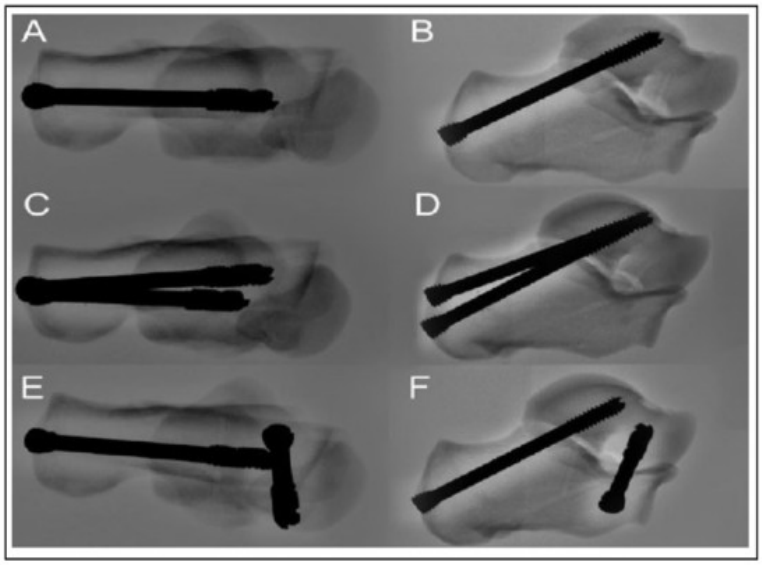

Figure 30: A. anterior-posterior, B. lateral image of the single screw construct (SS), C. and D. double parallel construct (DP), E. and F. double divergent construct (DD)[15]

3.2.2 Methods

Subtalar joint specimens were marked by the trained orthopedic surgeon [15]; hence two landmarks were located on the surface of the subtalar joint (talar head and calcaneal tuberosity). Once the landmarks were located, any straight line drawn between the two landmarks represents the axis of rotation, Figure 26. [15]

Next, small eyelet screws were inserted at the points defining the axis of rotation, Figure 31. A string was wound around one of the eyelet screw and pulled in tension. Another string was positioned and pulled in tension alongside the specimen, Figure 32. In this case, the strings represented the axis of rotation.

Pots of appropriate dimensions were prepared. The pots (calcaneus pot: length = width = 55 mm, height = 51 mm) , (talus pot: length = width = 55 mm, height = 22.22 mm) were cut from an S235 low carbon steel square tube of (2mm) wall thickness.

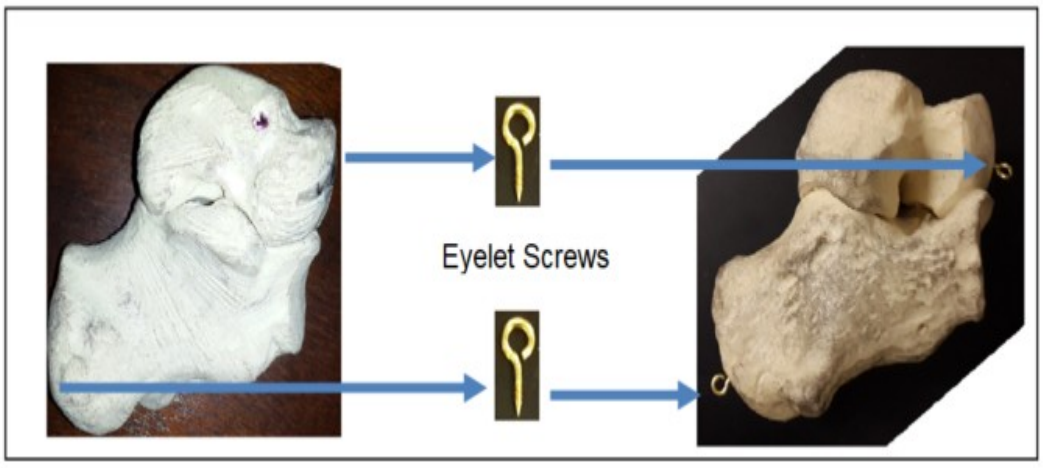

Figure 31: Inserting small eyelet screw

Figure 32: Winding strings around the eyelet screws and pulling in tension (strings = axis of rotation)

The pots were used later to poxy the specimen to them. Square pieces of wood were placed on one end of the pots to leaving suitable room for gluing the specimen. Also, a hole was made at the center of the pieces to make enough space for the strings (axis of rotation) to be aligned. In addition, the pieces were calked with the wall of the pots to prevent the poxy from leaking, Figure 33.

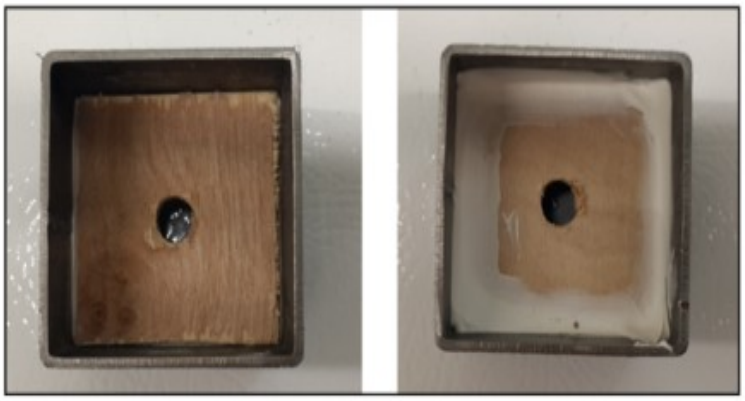

Figure 33: Pots: (left) uncaulked (right) caulked

Subsequently, an assembly (Jig) was designed and manufactured from wood to accurately have the axis of rotation in place vertically. The jig consisted of an assembly made from wood and two long screws, Figure 34. One of the long screws was placed at the upper end of the jig and the other was placed at the lower end, Figure 34. The long screws were placed in one vertical plane using a protractor; such that any string tensioned between the two long screws, the string would be aligned vertically, Figure 35.

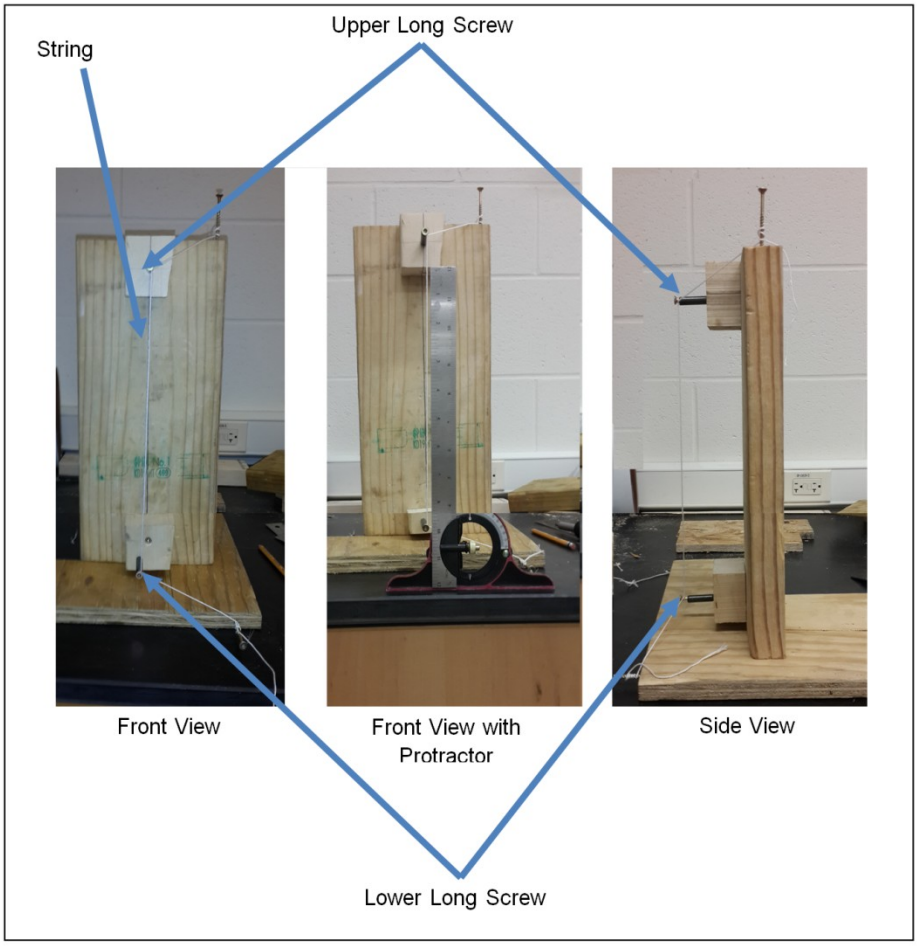

Figure 34: Specially designed jig for subtalar joint axis alignment

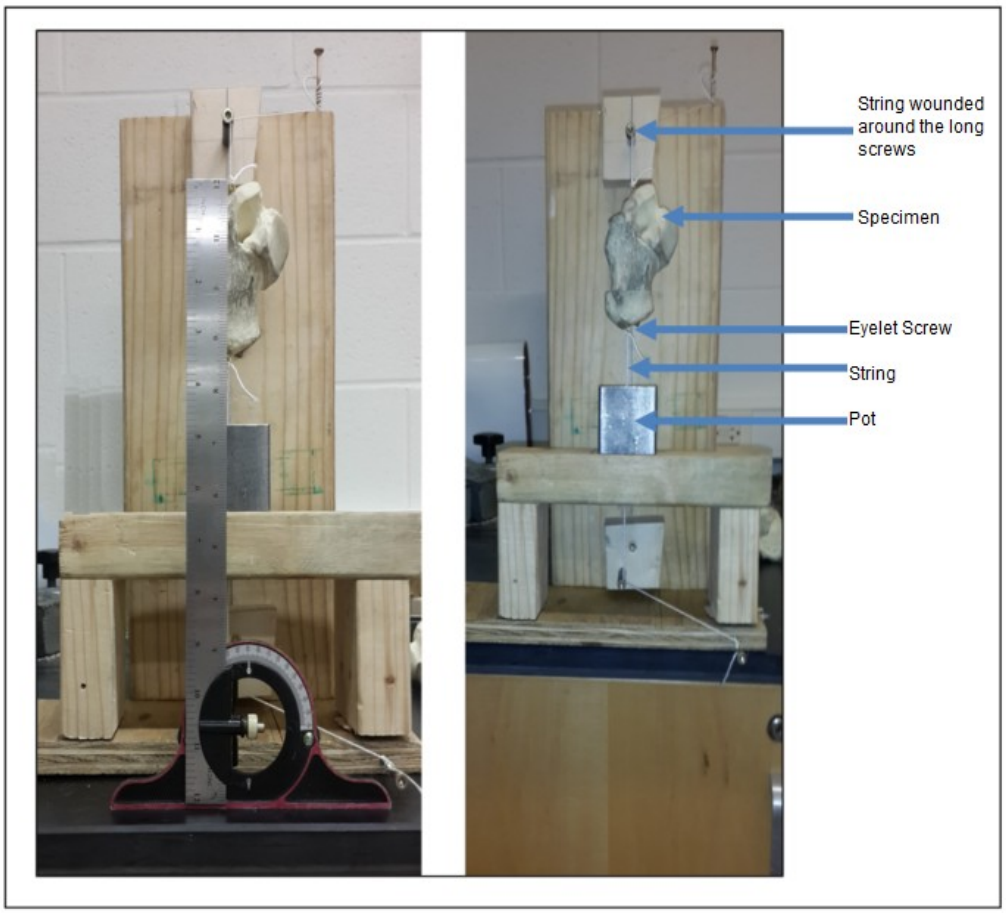

Figure 35: Subtalar joint axis of rotation alignment using the jig

Subtalar joint specimen's strings were wound around the upper and lower long screws of the jig, such that the strings (axis of rotation) were aligned vertically, Figure 35. After doing those procedures, the subtalar joint specimen was free to rotate around the axis of rotation and it could be moved up and down. Next, calcaneus pot was placed close to the lower long screw and the specimen was moved downward until a portion of the calcaneus occupied the room of the pot, Figure 36.

Figure 36: Fitting the specimen to pot the Calcaneus

As the specimen was free to rotate about the axis of rotation, another string was utilized to control specimen rotation. The string was placed in slight contact with the specimen at two points. Hence, contacting the specimen did not change the axis of rotation alignment vertically. This controlled the rotational alignment and assured that it was the same every testing attempt. Eventually, the specimen would be aligned axially and rotationally, Figure 37 and Figure 38.

Further, the clearance between the specimen and the internal wall of the square tube was approximately (1mm).

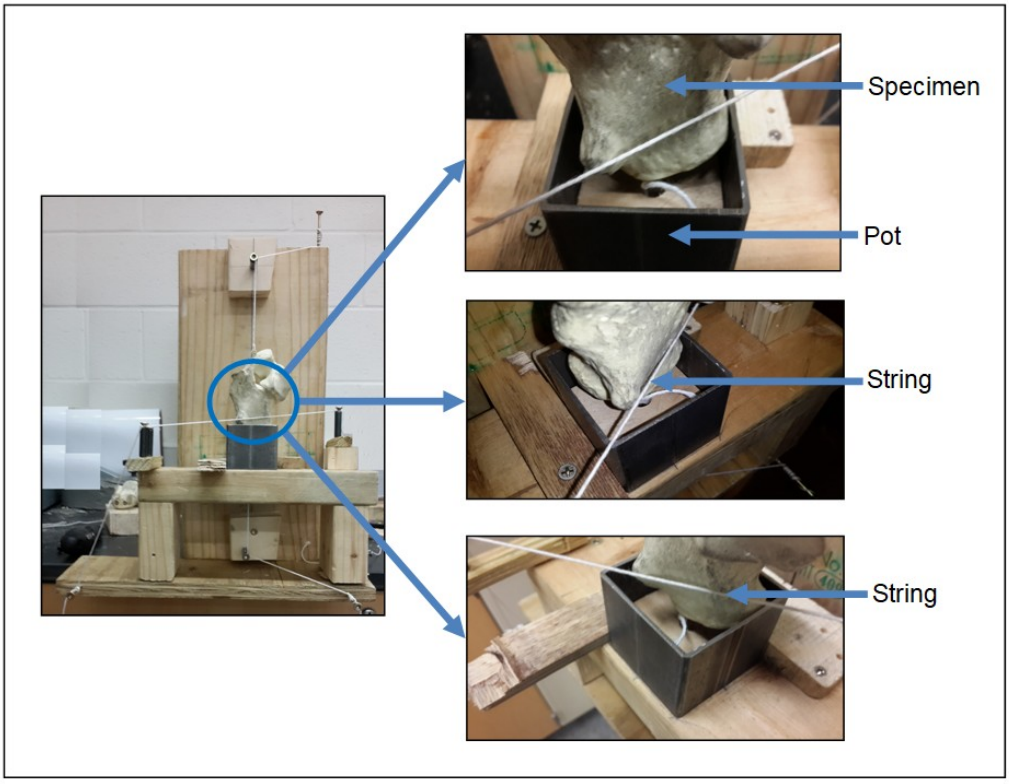

Figure 37: The feature of controlling specimen rotation

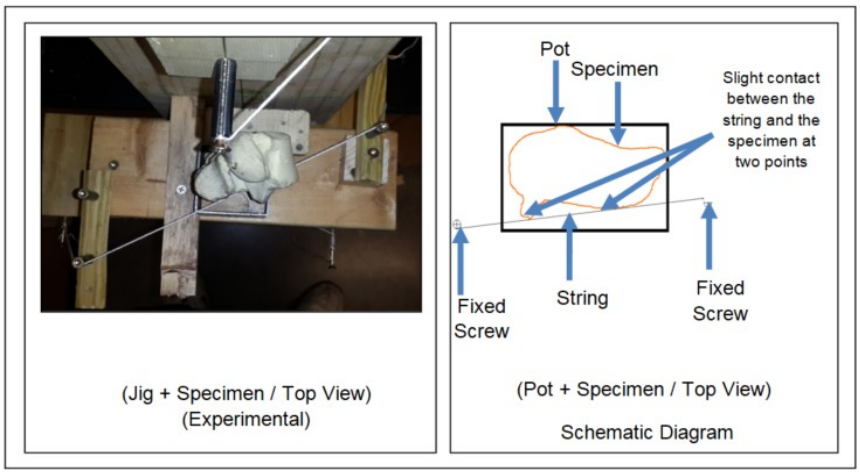

Figure 38: Illustration of the feature of controlling specimen rotation

After having the specimen loaded into the jig, the specimen was potted in epoxy. A Scientific Denture Material / Clear Self Curing (Fricke Dental International, Inc.); was poured into the tube, Figure 39. The epoxy took about 45 min's to solidify and was allowed to cure for an additional two hours prior to completion of any testing. The same whole procedure was repeated to pot the talus, Figure 40.

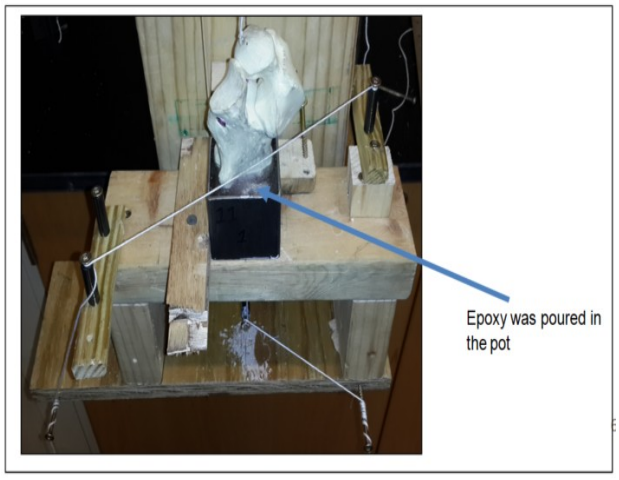

Figure 39: Subtalar joint alignment and gluing (Calcaneus)

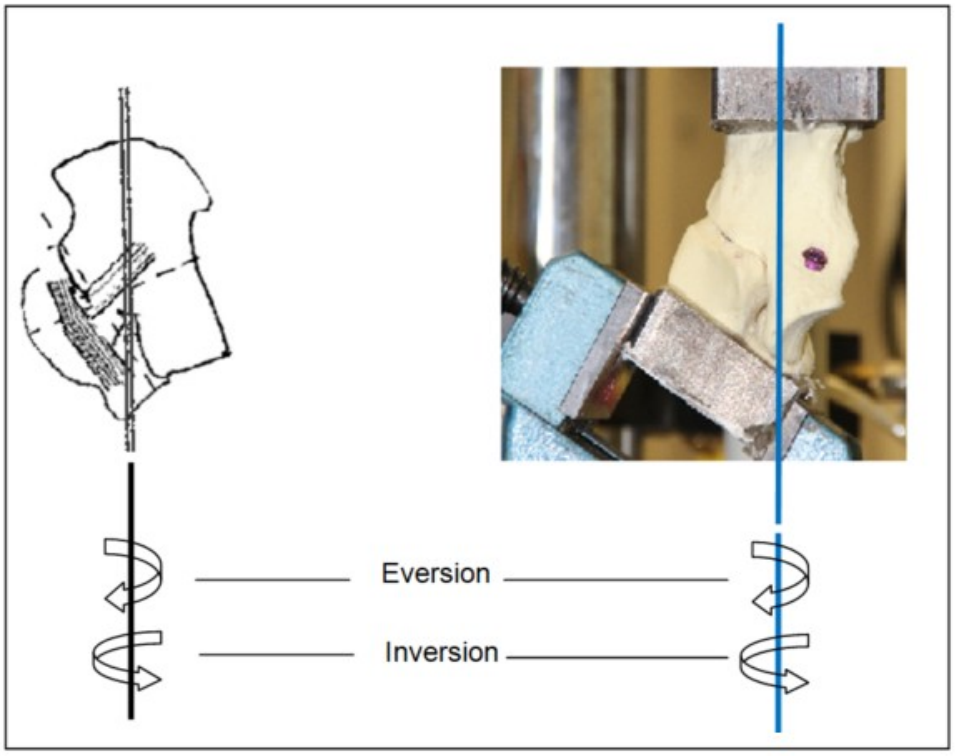

Figure 40: Subtalar joint alignment and gluing (Talus) [complete potted subtalar specimen]

3.3 Mechanical testing

Once the specimen potting was complete, the specimen was ready to be mechanically tested. The goal of the mechanical testing was to compare the fixation construct stiffness and strength as measured by relative motion of the fixed joint. The specimen were tested in eversion and inversion, Figure 40 and Figure 41 [15].

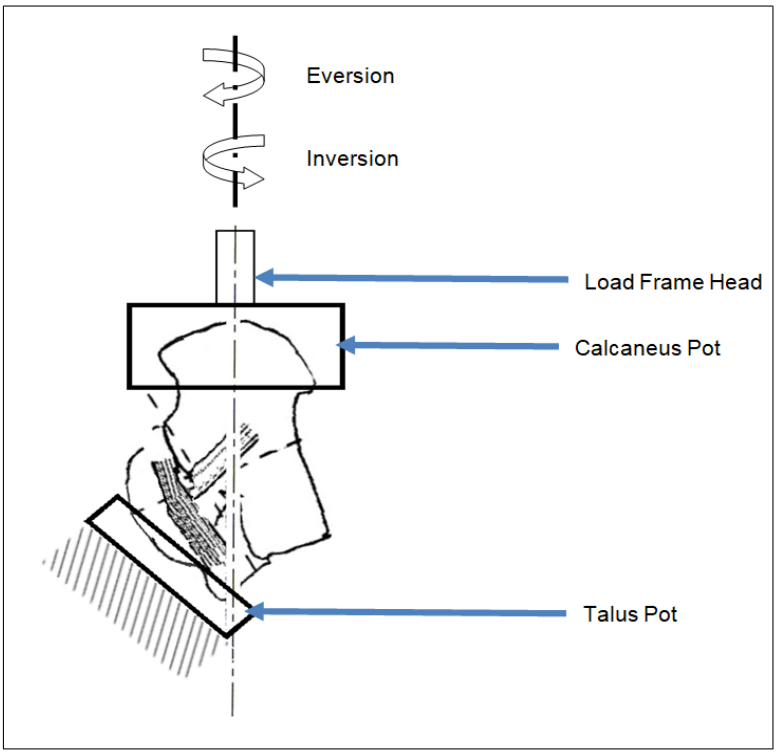

Figure 41: Schematic diagram of the mechanical testing

Torque load would be applied on the specimen. A double universal joint was used to assure torque load transmission to the potted specimen and to overcome the effects of misalignment, Figure 42. Two flanges were designed and manufactured. The flanges transmitted load to the double universal joint. The computer aided designs of the universal joint and the flanges were designed using Autocad 2014. An electromechanical servo-hydraulic machine load frame (MTS Bionix Model 370.02 table top servohydraulic test system, MTS Systems Corporation, MN, USA) that provided torque to stress the constructs, Figure 43. Torsion was applied at rate of 10 Degree / min until failure. Torque and angle of twist were acquired at 102.4 Hz. Specimens tested in eversion and inversion are shown in Figure 44 and Figure 45, [15].

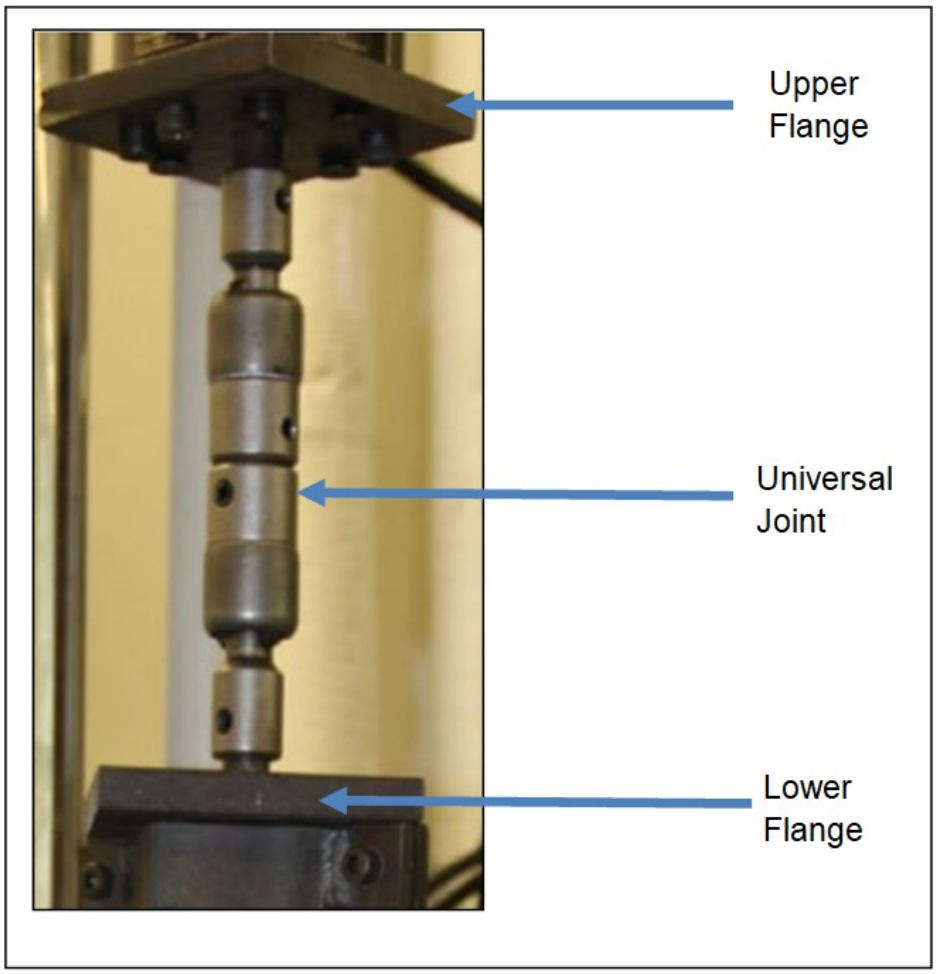

Figure 42: Double universal joint assembly

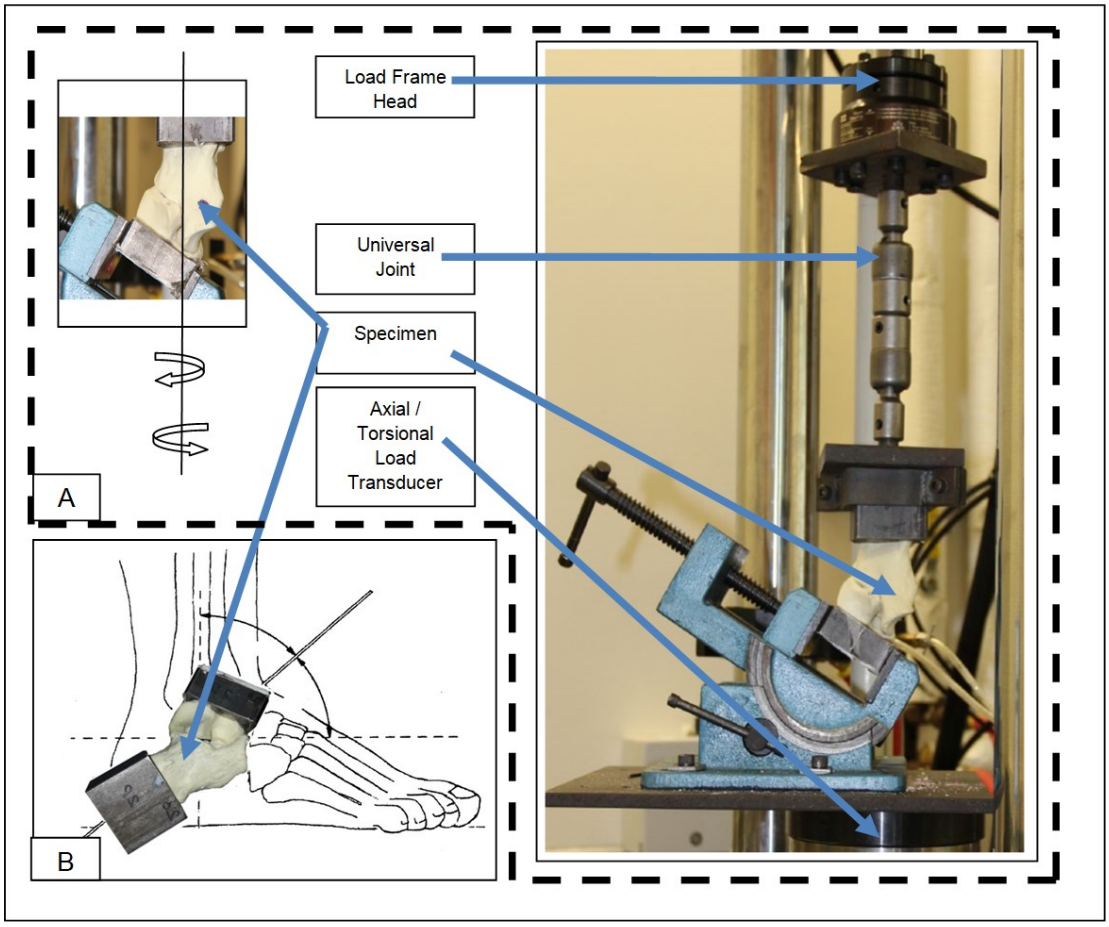

Figure 43: (A): testing assembly. (B): human representation [3]

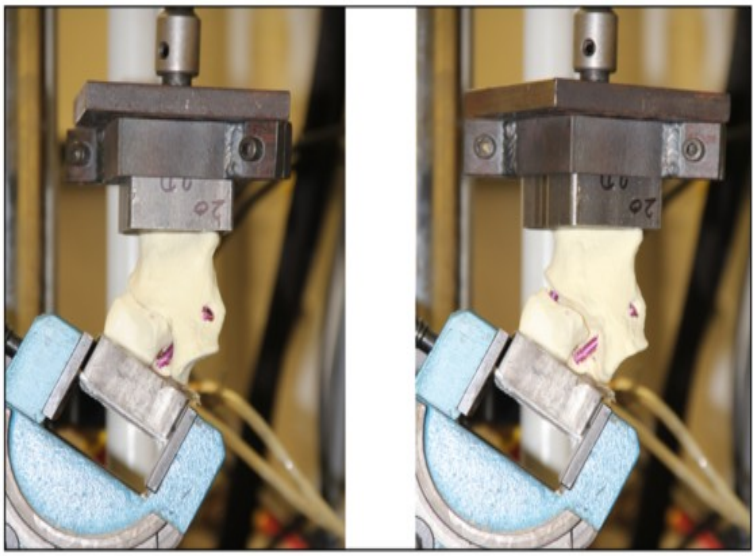

Figure 44: Testing DD specimen in inversion

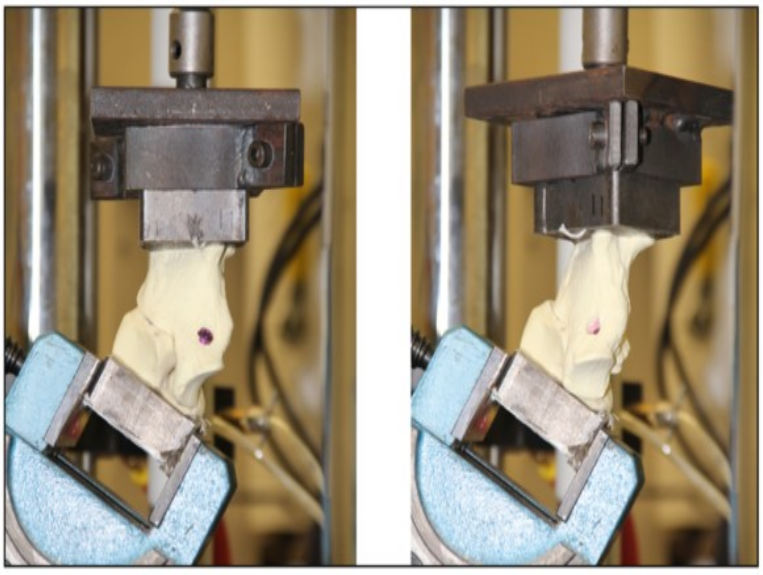

Figure 45: Testing DD specimen in eversion

3.4 Results

Ten specimens were prepared and tested per each screw configuration group and torque direction. Hence, group referred to (screw configuration: DD / PD / SS) and direction referred to (inversion / eversion), Table 5. Therefore, 60 specimens were prepared and tested. One specimen from group (DP screw configuration) and direction: eversion was discarded due to errant application of load. Hence, the overall number of specimens tested was 59.

Table 5: Grouping tested specimen according to screw configuration type and load direction

Double Screws (Divergent) (DD)		**Double Screws (Parallel) (DP)**		**Single Screw (SS)**	
inversion	*eversion*	*Inversion*	*Eversion*	*Inversion*	*eversion*
10 specimens	10 specimens	10 specimens	9 specimens	10 specimens	10 specimens

The aim of the mechanical testing was to examine: (1) maximum torque (2) torsional stiffness of the constructs. Torque in (N.mm) and angle of twist in (deg.) data were obtained during conducting the mechanical testing. Torque versus angle of twist were plotted per each group type.

Maximum torque value was obtained by picking the maximum point of (torque vs. angle of Twist) curve, Figure 46. Also, the start and end segment of the linear region of the (torque – angle) curve was picked. Torsional stiffness was gained by calculating the slope of the linear region.

Means, quartiles and ranges of maximum torque and torsional stiffness values of all groups of screws configurations and directions were plotted accordingly, Figure 47 and Figure

48. For specimens tested in eversion, the maximum torque carried by double divergent screw configuration (DD) specimens was (mean 22 206.8 N mm; SD 2725.1 N mm/degree).

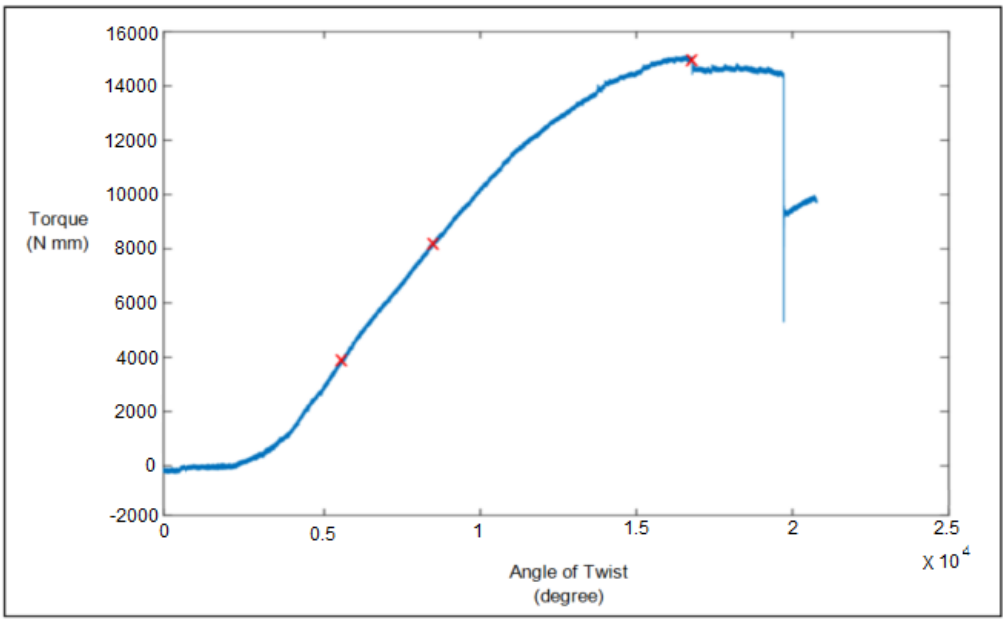

Figure 46: Picking maximum torque and linear region. The curve is for a certain specimen (illustration purposes)

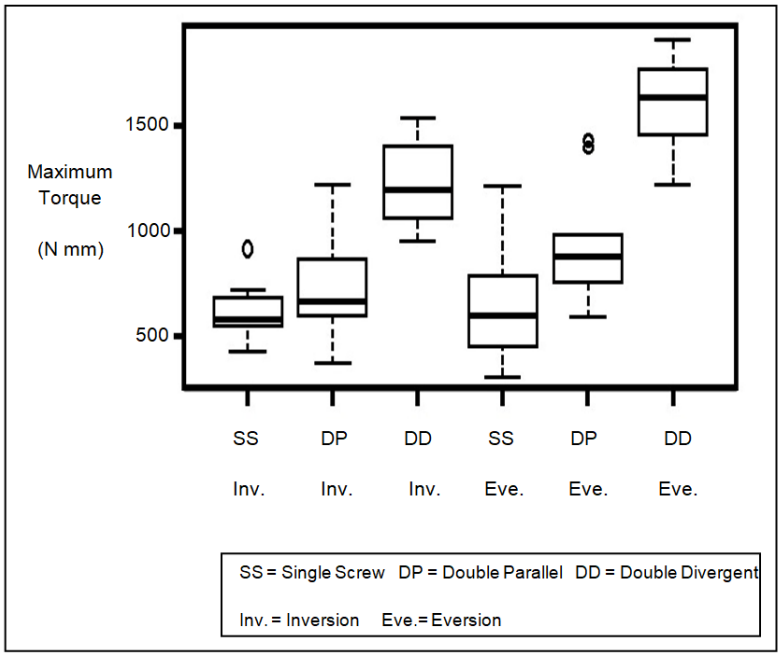

Figure 47: Maximum torque values. Mean, quartiles and ranges

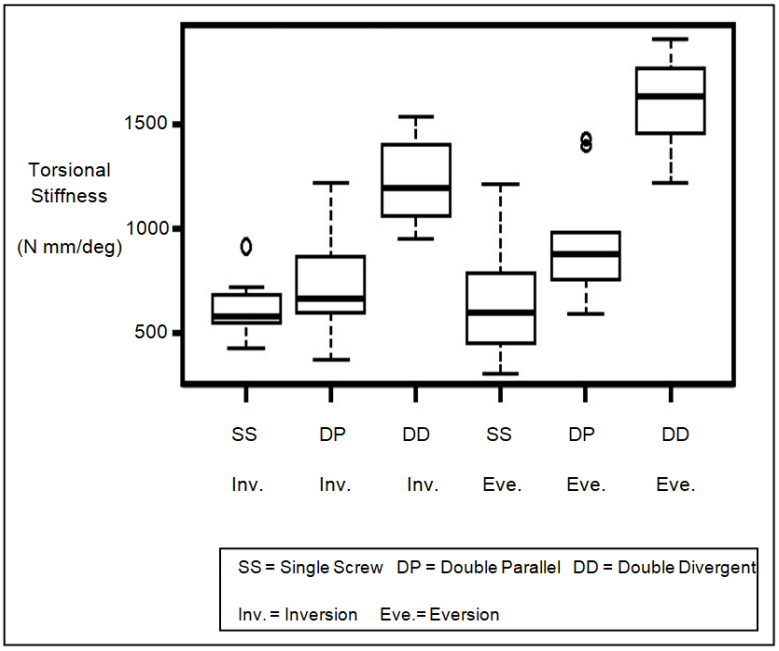

Figure 48: Torsional stiffness values. Mean, quartiles and ranges

It was higher than those of double parallel configuration (PD) (mean 12 607.6 N mm; SD 1630.6 N mm/degree) and single screw configuration (SS) (7543.3 N mm; SD 1517.7 N mm/degree). For specimens tested in inversion, the maximum torque of double divergent screw configuration (DD) specimens was (mean 19 613.3 N mm; SD 2324.2 N mm/degree). It was also greater than those of double parallel configuration (PD) (mean 13 198.6 N mm; SD 2563.2 N mm/degree) and single screw configuration (SS) (10 642.2 N mm; SD 1879.5 N mm/degree). As a result, the DD construct carried the highest torque among other groups and directions constructs, Figure 48.

For specimens tested in eversion, the torsional stiffness of the double divergent screw configuration (DD) specimens was (mean 1601.5 N mm/degree; SD 217.4 N mm/degree). It was higher than those of double parallel configuration (PD) (mean 944.7 N mm/degree; SD 288.3 N mm/degree) and single screw configuration (SS) (664.4 N mm/degree; SD 277.2 N mm/degree). For specimens tested in inversion, the torsional stiffness of double divergent screw configuration (DD) specimens was (mean 1233.0 N mm/degree; DP 205.9 N mm/degree). It was also greater than those of double parallel configuration (PD) (mean 717.0 N mm/degree; SD 228.9 N mm/degree) and single screw configuration (SS) (618.4 N mm/degree; SD 135.1 N mm/degree). As a result, the DD construct had the highest torsional stiffness among other groups and directions constructs, Figure 48.

3.5 Statistical study

A statistical study has been performed on the mechanical test data. Statistical calculations were completed using R: A Language and Environment for Statistical Computing, version 3.0.1 (R Foundation for Statistical Computing, Vienna, Austria). The Tukey's Honestly Significant Difference (Tukey HSD) was determined for both screw configuration group and torsion direction [15]. For screw configuration group, Tukey test showed that maximum torque and torsional stiffness among all pairings of screw configurations specimens were significantly different (P <.001); except (DP-SS) pair for torsional stiffness had (p=.05). Hence, that was also significantly different, Table 6. For torque direction, Tukey test demonstrated that maximum torque between inversion and eversion was not significantly different, Tukey HSD P = .57, Table 7. While, Tukey test showed that torsional stiffness between inversion and eversion was significantly different, Tukey HSD P < .001, Table 7.

Table 6: Tukey Honestly Significant Differences for screw configuration type

Tukey Honestly Significant Differences	Pairwiase Comparison	Difference in Means	95 % Confidence Lower Bound	95 % Confidence Upper Bound	P Adjusted
Stiffness (N mm/degree)	DP-SS	183.42	1.39	365.45	.05
	DD-SS	775.84	596.16	955.53	<.001
	DD-DP	592.43	410.40	774.46	<.001
Maximum torque (N mm)	DP-SS	3825.94	1936.44	5715.44	<.001
	DD-SS	11817.29	9952.17	13682.41	<.001
	DD-DP	7991.34	6101.84	9880.84	<.001

Table 7: Tukey Honestly Significant Differences for Torque direction

Tukey Honestly Significant Differences Eversion Inversion	Difference of Means	95% Confidence Lower Bound	95% Confidence Upper Bound	P Adjusted
Stiffness (N mm/degree)	213.65	90.55	336.76	<.001
Maximum torque (N mm)	-361.24	-1639.11	916.64	.57

3.6 Discussion

The double divergent (DD) screw configuration specimen gave the highest maximum torque among other screws configurations, followed by DP specimen then SS specimen. It was also noted that DD specimen was stiffer than other screws configurations, DP specimen followed by SS specimen. Overall, DD specimen was the most rigid construct such that it provided the highest maximum torque and torsional stiffness. Structurally, the DD screw configuration heavily supported the bone tissue (cortical + trabecular). That was because the double divergent construct (DD) had two screws placed inside the longest anatomical length of subtalar joint geometry; such that the screws presented extra support to the whole bone. As a result, the bone tissue became more rigid to resist rotation. Anatomically, the geometry of the subtalar joint along with the DD construct also helps to add extra rigidity to resist rotation.

Maximum torques between eversion and inversion could not be compared because they were not significantly different (Tukey HSD P = .57). While, specimens tested in eversion were stiffer than those specimens tested in inversion. In eversion, the calcaneus slightly moved where the posterior talar articular surface of calcaneus came into greater contact with the posterior process of talus, see Figure 49. As eversion load application continued, a contact at the critical

angles facets between calcaneus and talus happened. That also increased the stiffness of the construct. Whereas, in inversion, the calcaneus slightly moved less where the middle talar articular surface of calcaneus came into greater contact with the head of talus, see Figure 50. As inversion load application continued, a contact took place at the facets of sustentaculumtali of calcaneus and the head of talus. That presented a certain resistance to the relative motion between the calcaneus and talus. This added a stiffness but less than the one that accumulated in eversion. The anatomy of critical angles (in case of eversion scenario) were more acute than those of sustentaculum tali, thus, offering greater resistance to rotation in eversion.

The limitation of this study: (1) synthetic bone specimens were used in this biomechanical test, (2) the vivo axis of motion about the subtalar joint (eversion/inversion load) was complex and difficult to conceptualize.

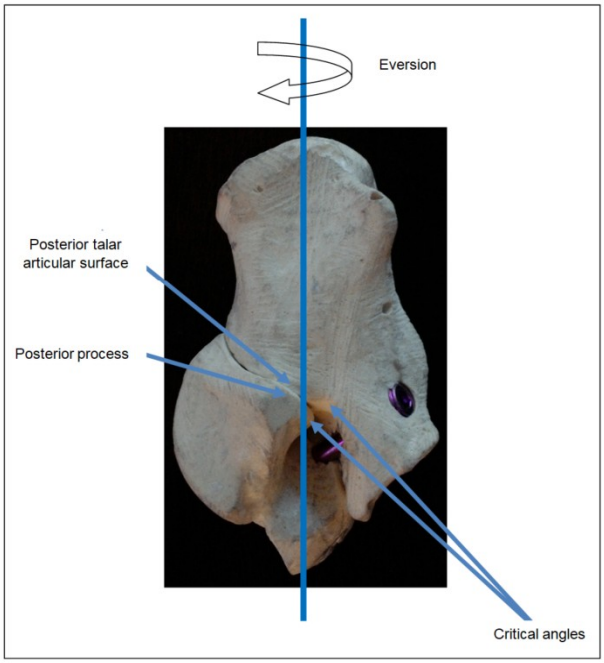

Figure 49: Subtalar structural - anatomical description (eversion)

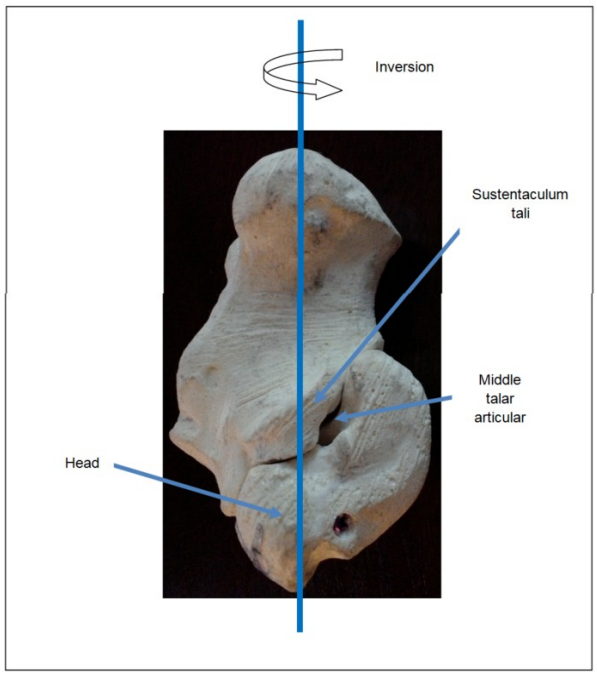

Figure 50: Subtalar structural - anatomical description (inversion)

3.7 Conclusion

This chapter provides a contribution to understanding the complex biomechanics of subtalar joint loaded in eversion/inversion. The results demonstrate the fact that the stiffness of subtalar joint in eversion is higher than that in inversion. Also, a structural–anatomical description of subtalar joint loaded in eversion/inversion emphasized the fact above. That is because of the screw configuration and the anatomy of subtalar joint. In addition, this study supports the hypothesis: double divergent screw configuration is a biomechanically more effective and potentially safe replacement for fusion and fixation goals. Furthermore, the designed experimental fixture and jig can be used for additional studies.

CHAPTER IV

A STOCHASTIC FINITE ELEMENT METHOD FOR SIMULATING TRABECULAR BONE

4.1 Introduction

In chapter 3, the biomechanics of subtalar joint arthrodesis was explored. The subtalar joint consists of the talus and calcaneous and subtalar joint arthrodesis fuses these two bones using screws. The screws must interact with both the cortical and cancelous tissue of these bones; hence, these individual tissues also impact the biomechanics of the fusion. However, the techniques to model these tissues are still rudimentary. In this chapter, a new method of modeling trabecular bone is proposed and evaluated.

4.2 Background

As trabecular bone is a main component of foot and ankle bones and is a complex structure, trabecular bone is simulated in this chapter. Although trabecular bone is a highly porous heterogeneous composite, most studies use homogenized continuum finite element (FE) approaches to model trabecular bone. Such models neglect the porous nature of the tissue. When microstructural models are desired, the use of continuum elements may require costly CT/MRI imaging and detailed meshing. This chapter demonstrates an approach that simulates trabecular bone with less dependency on medical images while capturing the effect of porosity.

4.3 Structural stochastic model of trabecular bone

Trabecular bone consists of a three-dimensional network structure mainly composed of rod-shaped and plate-shaped fundamental units named trabeculae [4]. In this work, the trabeculae were modeled as beam elements [33]. The method assumed randomly oriented beams within a 4 mm cube [33]. Random seed positions were used to compute a Voronoi diagram that defined the trabecula [45], [46]. Hence, trabeculae were created algorithmically so that trabeculae properties could be applied stochastically, Figure 51. The algorithm is general to apply a stochastic approach to all trabeculae properties. However, in this article, the randomized seed generates a distribution of trabecular lengths and orientations while the cross section was assumed square. The beam element type was a two node linear beam element (B31). Homogeneous isotropic material properties of trabecular bone were assigned to each trabecula element (E=6800 MPa, ν=0.3) [34] [47]. Abaqus (V. 6.16, Simulia Ltd) was used as the FE solver. Trabecular bone was modeled assuming a quasi-static load in an implicit model. Displacement control boundary conditions were applied on the "cube surface" nodes of the trabeculae structure to attain effective axial and shear loads on the specimen. For axial load, constraints were placed on two parallel faces of the specimen. Only normal degrees of freedom were fixed for nodes of one face and a small displacement of 0.0008 mm was perpendicularly imposed on the nodes of the opposite face, Figure 52 [48]. For shear load, the constraints were placed on four orthogonal faces of the specimen in opposing pairs. Only normal degrees of freedom were fixed for nodes of the lower left edge of the specimen. Also, a small displacement of 0.0008 mm was imposed on the nodes of each face and parallel to the face; such that pure shear was consistently applied to the

specimen ,Figure 52. As the displacement load was applied on the trabecular bone, the bone deforms axially and in shear as shown in Figure 53.

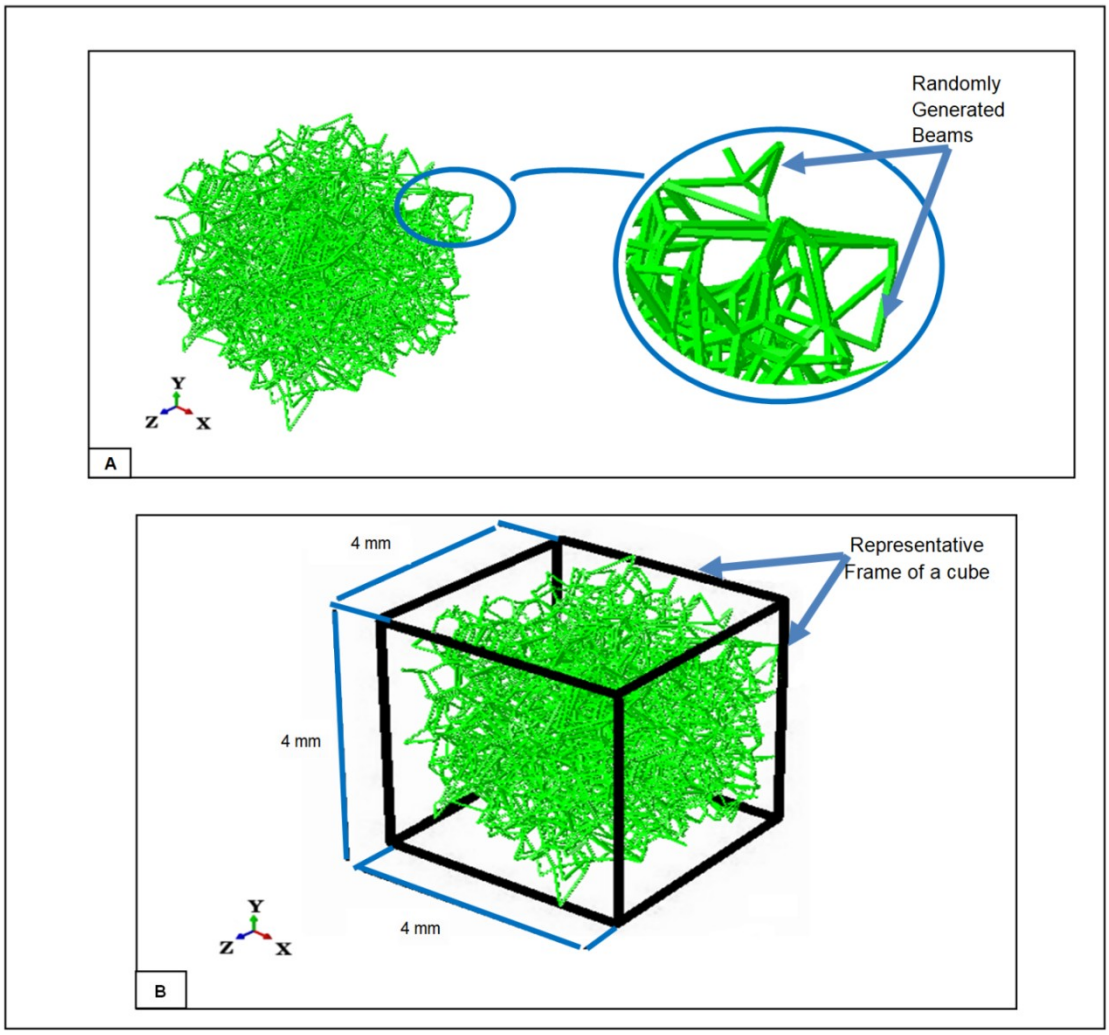

Figure 51: (A) Trabecular bone specimen (structured from randomly generated trabeculae) / (three dimensional Voronoi model), (B) Trabecular bone cube (representative cube)

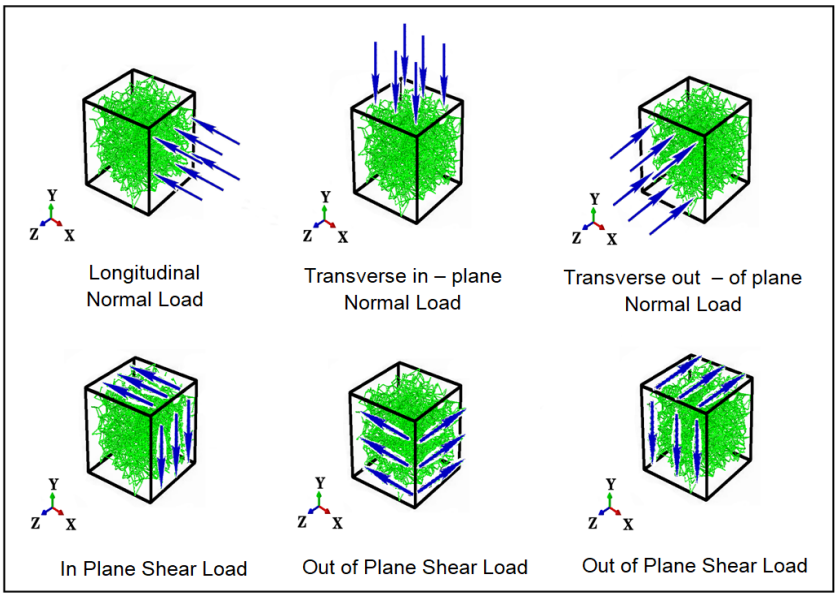

Figure 52: Directions and planes of loadings - trabecular bone specimen (normal test / shear test)

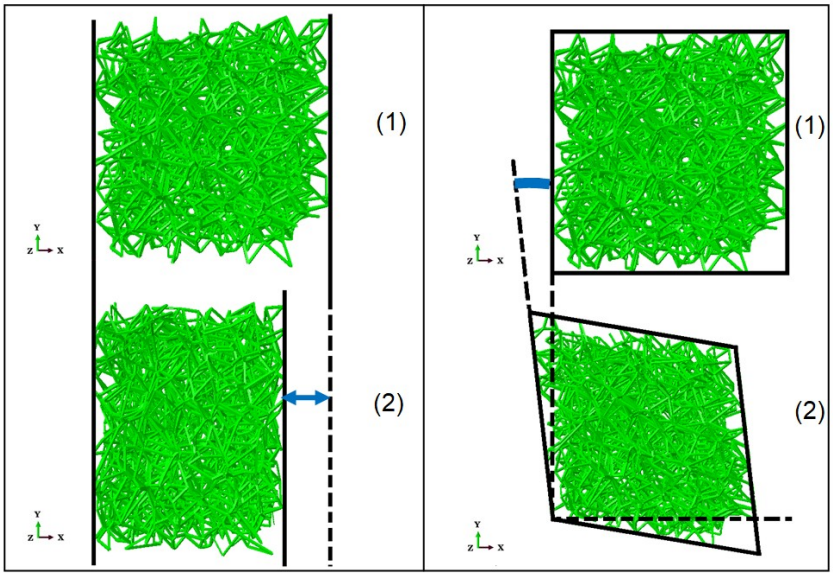

Figure 53: (Left) Axial deformation: (1): no load, (2): with axial load, (Right) Shear deformation: (1): no load, (2): with shear load

The contour of deformations and reactions forces is indicated in Figure 54. For axial loading (0.0008 mm), all the nodes on one face "plane" were displaced (0.0008 mm) in the normal direction (blue, Figure 54). While the opposite face nodes were fixed (red) in the normal direction. All other side faces nodes were constraint only in the normal directions. Similar displacements were enforced to impose shear load (colored from green to red, Figure 54. The nodes that were in bottom left corner are fixed (blue color). Reaction forces were accordingly produced on the peripheral/constrained nodes of the cube (see Figure 54). Apparent stress was calculated by dividing the summed nodal reaction forces by the apparent area of the relevant face.

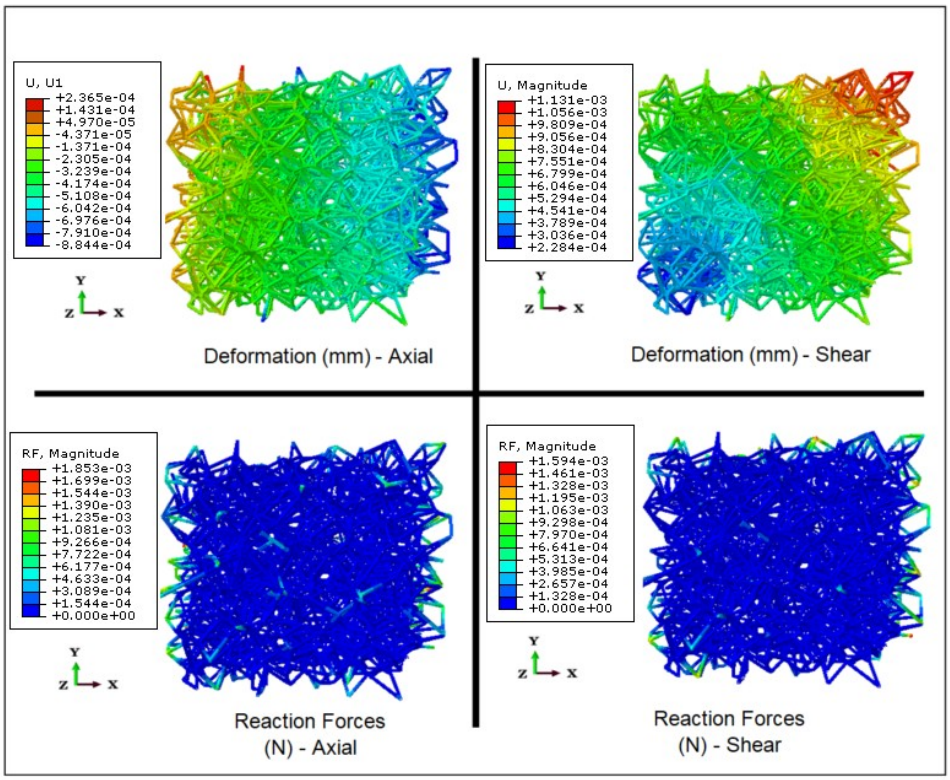

Figure 54: Deformation and reaction forces contours (axial / shear)

Apparent strain was obtained by calculating the ratio of resulting displacement of the moving nodes to the original side length of the specimen (i.e., change in length over length) (see Figure 52). Furthermore, apparent moduli were computed from apparent stress and apparent strain. Apparent densities were calculated by obtaining the ratio of the trabeculae s' total mass to the volume of the unit cube. Moreover, anisotropy ratio was calculated by dividing the maximum normal modulus by the minimum normal modulus of each individual model [49]. A distribution of model outcomes was obtained by running (4050) models sequentially by script. The script was written employing Python and Matlab (see Figure 55). Each model simulated axial and shear responses, as well as tension and compression (see Figure 53). Five apparent densities were targeted; (0.2, 0.4, 0.6, 0.8, 1) g/cm^3 in the proposed clinical study. Models were run per number of seeds, hence, each apparent density was targeted.

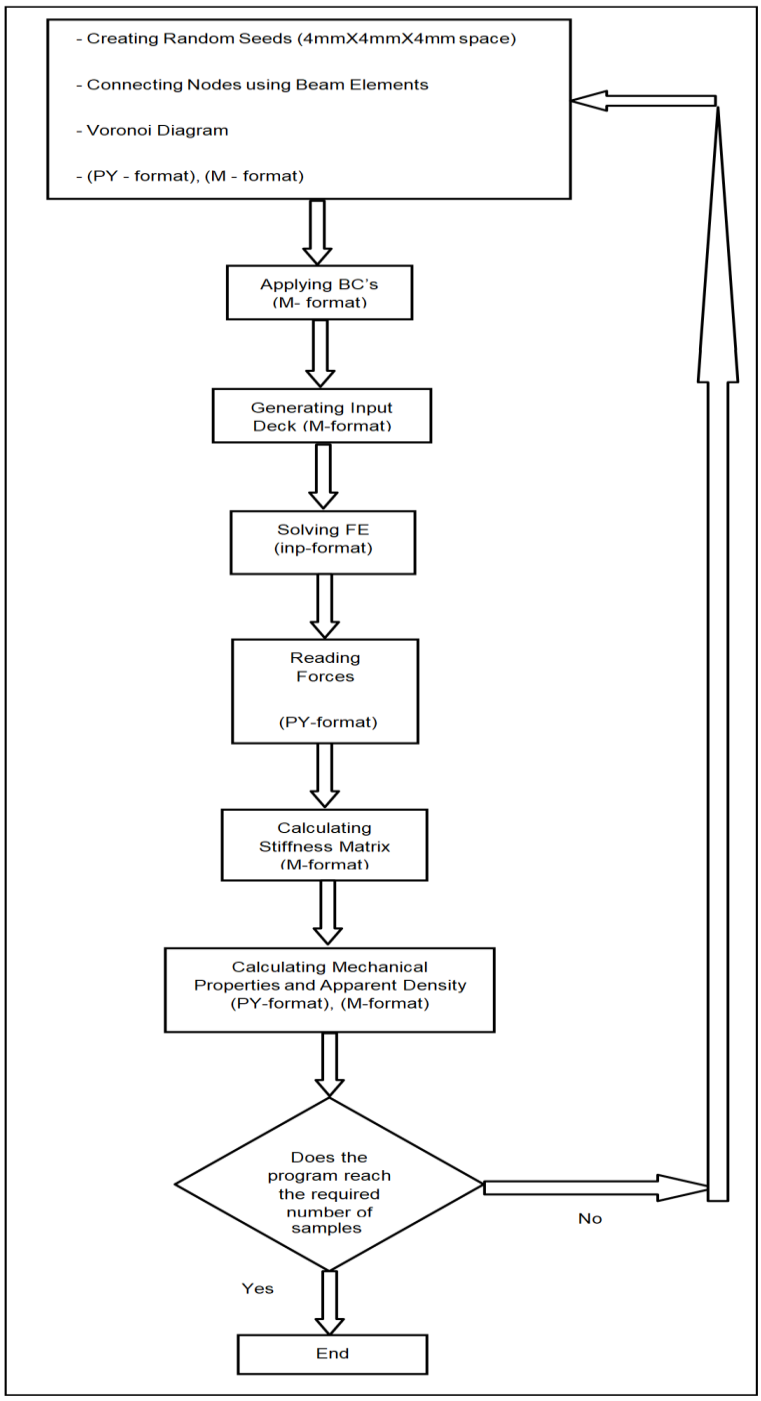

Figure 55: Script file, file conversion flow-chart diagram, required for input into ABAQUS software

4.4 Identifying FE model parameters

In this study, the trabecular bone parameters that were considered include: apparent density, Voronoi diagram number of seeds points, trabeculae cross section area, trabeculae mean length and number of trabeculae. Other related modeling parameters were implicitly implemented; such as: trabeculae orientation and trabeculae connectivity. Because each trabecula was represented by a beam element, the parameters were denoted in terms of trabeculae, Table 8:

Table 8: Model parameters definition

Parameters	Definition
ρ_{app}	Apparent density
N_S	Voronoi diagram-number of seeds points
A_T	Trabecula cross section area
L_T	Trabecula length
N_T	Number of Trabeculae

(N_S), (N_T) and (L_T) are dependent on each other "quasi-stochastic relationship" [50]. (N_S) was selected as an input control parameter. (N_T) and (L_T) are highly dependent on (N_S) and its points coordinates in space. As (N_S) changes, (N_T) and (L_T) change quasi-stochastically. Porosity, (ρ_{app}) and volume fraction (Vf) are dependent on each other as indicated in eq. (1) and eq. (2) below [4]:

$$V_f = \frac{\text{Vol .of actual tissue } (V_{tiss})}{\text{Vol .of bulk bone } (V_{bulk})} = \frac{\rho_{app}}{\rho_{bulk}} \quad (1)$$

$$\%V_f = 1 - p \quad (2)$$

In real bones, tissue density varies across the network structure of the bone; hence, volume fraction and apparent density are related but not perfectly correlated. However, in this

work, each trabecula was assigned the same tissue density. Hence volume fraction and apparent density are directly proportional.

As a result, (ρ_{app}), (N_T) and (L_T) were chosen as indicating parameters. Overall, the control parameters used to conduct a parametric investigation are: (N_S) and (A_T). Only for the purpose of conducting the parametric study, (N_S) and (A_T) were set as input's to the model, while (ρ_{app}), (N_T), (L_T) and the mechanical properties (E_{xx}, E_{yy}, E_{zz}, G_{yz}, G_{xz}, G_{xy}, ν_{yz}, ν_{zy}, ν_{xz}, ν_{zx}, ν_{xy}, ν_{yx}, AIratio (Anisotropic Ratio)) were considered as output's from the model (see Figure 56 (A)). (ρ_{app}), (N_T), (L_T) were provided by the model, (ρ_{app}) was utilized to check the value of the model trabecular bone apparent density. Some of the ranges of the described parameters were reported in the literature, Table 9. Those ranges were utilized for comparison and validation of the current work. Also, the mechanical properties of the trabecular bone were reported in the literature, Table 10. The predicted mechanical properties from the current FE model were expected to be within the ranges of Table 10.

Table 9: Target parameter ranges to be consistent with existing literature [29] [51] [52][53]

Parameter	Range
A_T	0.003 to 0.05 (mm^2)
L_T	0.074 to 1 (mm)
ρ_{app}	0.05 to 1.1 (g/cm^3)

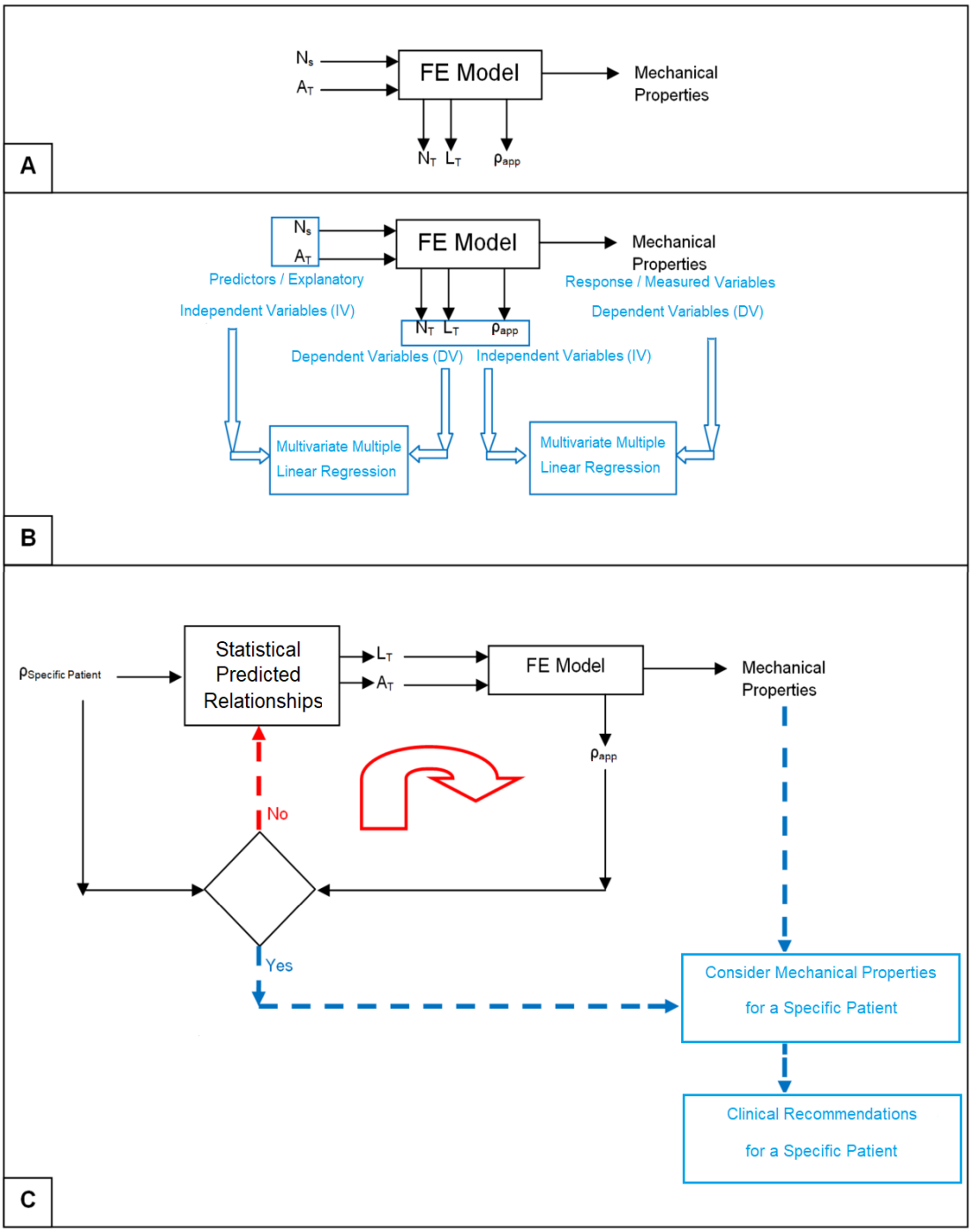

Figure 56: (A) Identifying parameters setup, (B) Stochastic statistical study setup, (C) Proposed clinical procedure setup

Table 10: Target trabecular bone mechanical property ranges to be consistent with existing literature [4] [54] [27] *

Independent Elastic Constants	Range
E	31(22.5) to 1107(634) (MPa)
G	18.4(12.9) to 134(49) (MPa)
ν	0.063(0.217) to 0.423(0.356)
AIratio	1.22 to 1.91

* Paraenthesis indicate standard deviation.

The cross sectional area (A_T) was set to the range (0.01 to 0.02 mm^2) in the FE model and was assumed square, Table 9. Assuming (A_T) square has not been reported in the literature before; that may help to investigate the effects of other shapes of (A_T). (ρ_{app}) was calculated by obtaining the ratio of the trabeculae s' mass to the volume of the cube.

The mass was directly proportional to the volumes of the trabeculae, and the apparent density was a relative measure of both volume and density which could be compared to the literature. The calculated apparent density (ρ_{app}) from the model was typically expected to be within the range from 0.05 to 1.1 g/cm^3, Table 9. Also, the predicted mechanical properties from the model were expected to be within the ranges in Table 10. The parametric study was performed by holding (A_T) fixed and varying (N_S) and vice versa, (see Figure 56 (A)). This was to investigate how each parameter affects trabecular bone apparent density and mechanical properties (model output). The parametric study was conducted taking into consideration the ranges of all the described parameters in Table 9 and Table 10 to estimate (N_S). (N_S) was found ranging (from 150 to 900 seed "point in 3D"), which is the final outcome of identifying the model parameters.

4.5 Stochastic statistical study

In this study, (N_S) and (A_T) have been randomly selected from a normal distribution in each model. (N_S) normal distribution was centered on a mean 200; that results in average trabeculae elements length (L_T =0.33 mm) and average number of trabeculae (N_T =1500). (A_T) normal distribution was also centered on a mean (0.05 mm^2); such that it provided reasonable ranges of the model output. Namely, the current study presentd models for a trabecular bone of (0.8 g/cm^3) apparent density. For the current statistical study, the cross section was square. (N_S) was input into the Python script. (A_T) was input into Abaqus input-file by importing trabeculae square cross section side length; in turn, the model delivered data of (ρ_{app}), (N_T), (L_T) and the mechanical properties (see Figure 56 (A)).

Descriptive statistics were calculated from the model results. Linear regressions was conducted to estimate the strength of the relationship among the FE model parameters "variables". The variables include: (N_S), (A_T), (ρ_{app}), (N_T), (L_T) and the mechanical properties (see Figure 56 (A)). Also, the analysis helped to predict the value of a response variable or outcome from the known values of one or more explanatory variables or predictors. Two regression analyses have been conducted. For the first regression analysis, " N_S " and " A_T" were set as independent variables. (ρ_{app}), (N_T), (L_T) were set as dependent variables. For the second regression analysis, (ρ_{app}), (N_T), (L_T) were set as independent variables. The mechanical properties were counted as dependent variables, (see Figure 56 (B)). Calculations were completed using R: A Language and Environment for Statistical Computing, version 3.4.3 (R Foundation for Statistical Computing, Vienna, Austria). A multivariate multiple linear

regressions was employed to determine if (N_S) and (A_T) are accurate predictor of mechanical properties and apparent density, see Figure 56 (B).

4.6 Proposed clinical procedure

Mechanical properties of bone are strongly dependent on the density and trabeculae property at micro-level. The most common measures of bone density are tissue density and apparent density. Density is essential in indicating bone condition changes (like, osteoporosis, aging and mineral content) [4]. As apparent density is easier to measure, it is a commonly indicator of bone porosity. Hence, apparent density (ρ_{app}) is utilized to estimate the bone health. A proposed clinical parametric study was described utilizing the results of the previous stochastic statistical study. Once bone density scan provided $\rho_{app\ -scan}$, (N_S) and (A_T) were set as inputs to the model. (N_S) and (A_T) were set as inputs to the model such that $\rho_{app} =\sim \rho_{app\ -scan}$. ($N_S$) and ($A_T$) control ρ_{app} and the mechanical properties delivered from the model, see Figure 56 (C).

In this study, (N_S) and (A_T) have been set to certain values; such that they serve to provide a distribution of apparent density. Only two values of A_T were selected (0.01 mm^2 and 0.02 mm^2). (N_S) was selected individually per each intended apparent density (270, 635, 390, 580 and 800) seed point; that was for (0.2, 0.4, 0.6, 0.8 and 1) g/cm^3 apparent density, respectively. The model was run 623 times for each target apparent density. A random unique mesh was generated at each model run. Hence, the trabeculae parameters were different at every run. (N_S) was input into the Python script. (A_T) was input into Abaqus input-file by importing trabeculae square cross section side length. In turn, the model delivered data of (ρ_{app}), (N_T), (L_T) and the mechanical properties, see Figure 56 (A).

4.7 Results

4.7.1 Stochastic statistical study

" N_S " and " A_T " were imported to the statistical model. The quantitative variation of the variables of the FE model is presented in (Figure 57- Figure 66). All the delivered mechanical properties were within the ranges specified in the literature, Table 9 and Table 10. The cross sectional area (A_T) was set to the range (0.01 to 0.02 mm^2) in the FE model and was assumed square, Table 9. Assuming (A_T) square has not been reported in the literature before; that may help to investigate the effects of other shapes of (A_T). (ρ_{app}) was calculated by obtaining the ratio of the trabeculae mass to the volume of the cube.

N_S was of symmetric normal distribution (mean 200 seed point; SD 30 seed point), (see Figure 57). A_T had symmetric normal distribution of (mean 0.053 mm^2; SD 0.014 mm^2), (see Figure 57). "N_T" was also normally distributed (mean 1530 trabecula ; SD 270 trabecula); (see Figure 58). ρ_{app} appeared to be normally distributed (mean 0.82 g/cm^3; SD 0.238 g/cm^3), (see Figure 59).

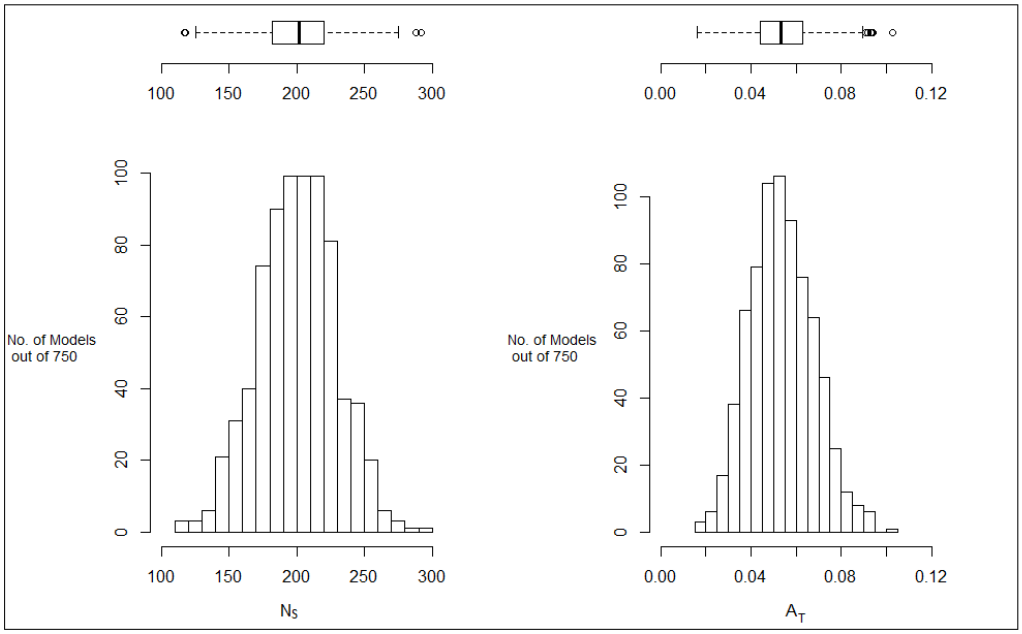

Figure 57: "No. of seeds", "Trabeculae cross section area" distributions

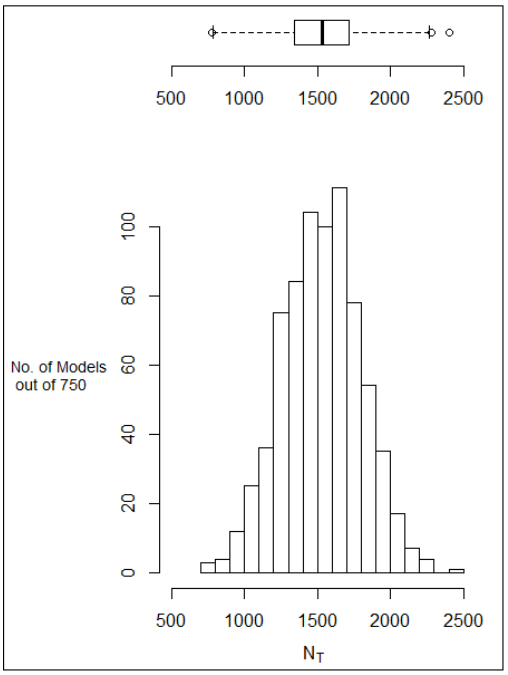

Figure 58: "No. of trabeculae" distributions

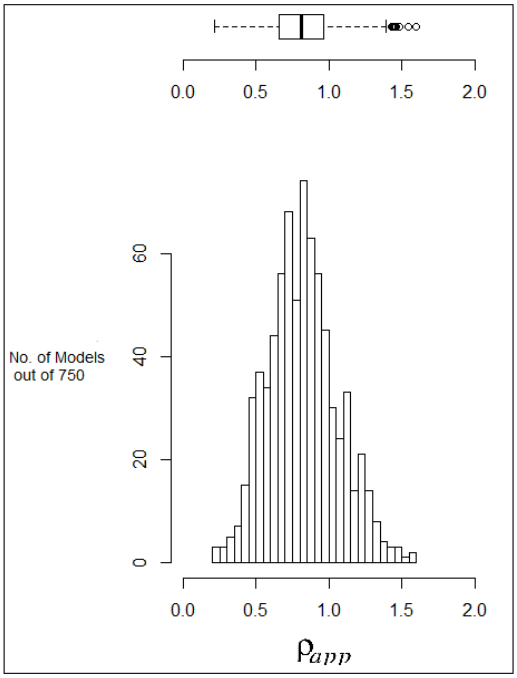

Figure 59: "Apparent denstiy" distribution

E_{xx}, E_{yy} and E_{zz} were internally consistent, (see Figure 60 and Figure 61). The distribution of Young modulus values in x direction (E_{xx}) was right-skewed (skewness coefficient 1.23 MPa). Also, E_{yy} distribution was also right-skewed (skewness coefficient 0.617 MPa). E_{zz} was right-skewed (skewness coefficient 0.461 MPa) as well. The distribution of shear modulus values in yz plane (G_{yz}) was right-skewed (coefficient of skewness 1.11 MPa), (see Figure 62). G_{xz} was again right-skewed (coefficient of skewness 0.271 MPa), Figure 62. Also, G_{xy} was right-skewed (coefficient of skewness 0.832 MPa), Figure 63.

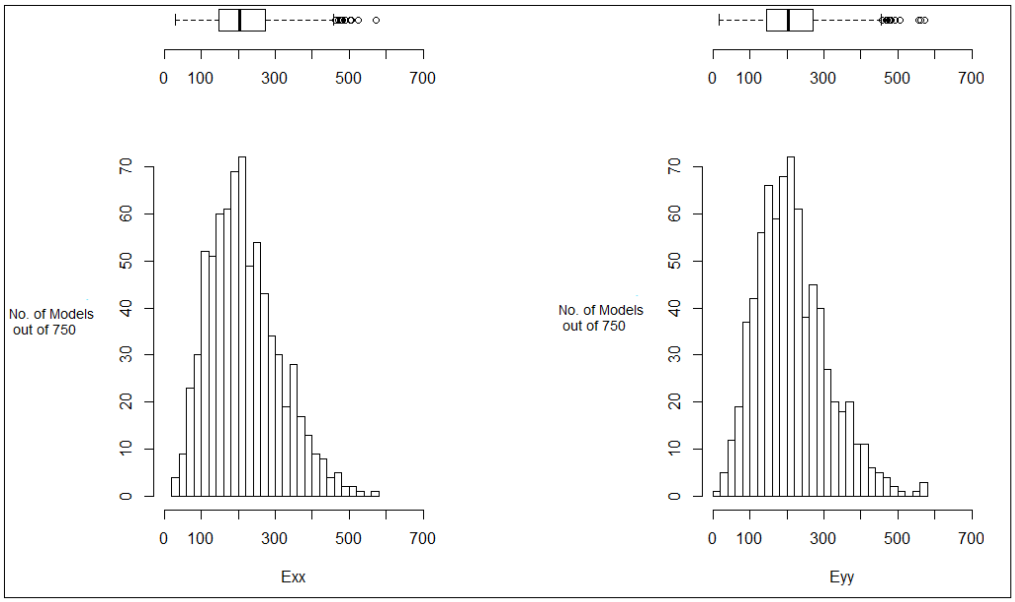

Figure 60: "E_{xx}" , "E_{yy}" distributions

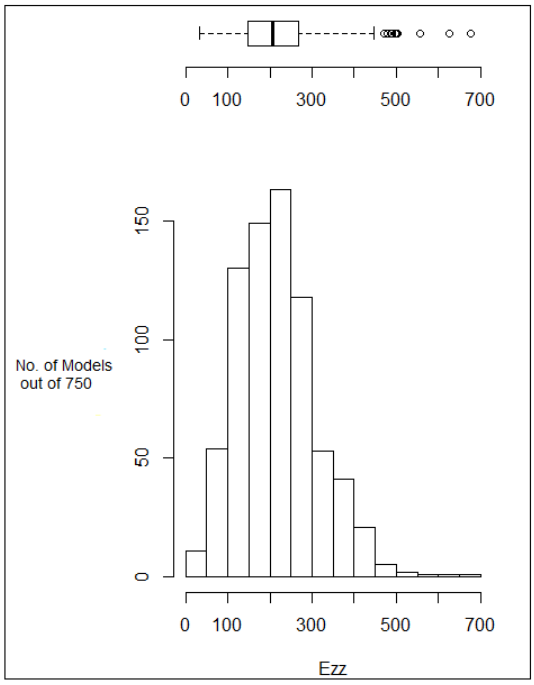

Figure 61: "E_{zz}" distribution

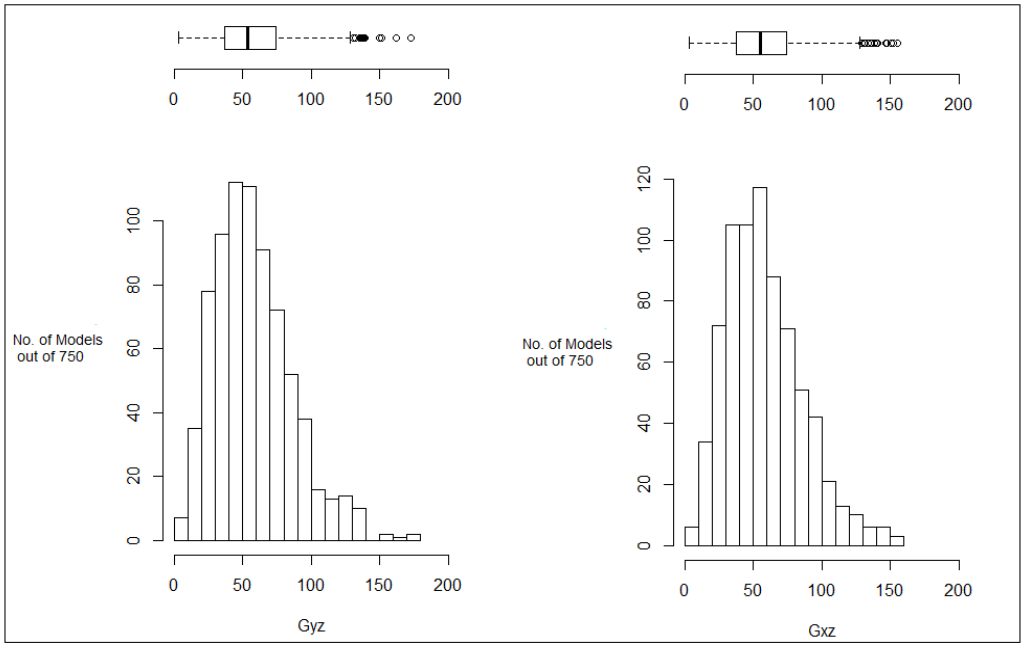

Figure 62: "G_{yz}" , "G_{xz}" distributions

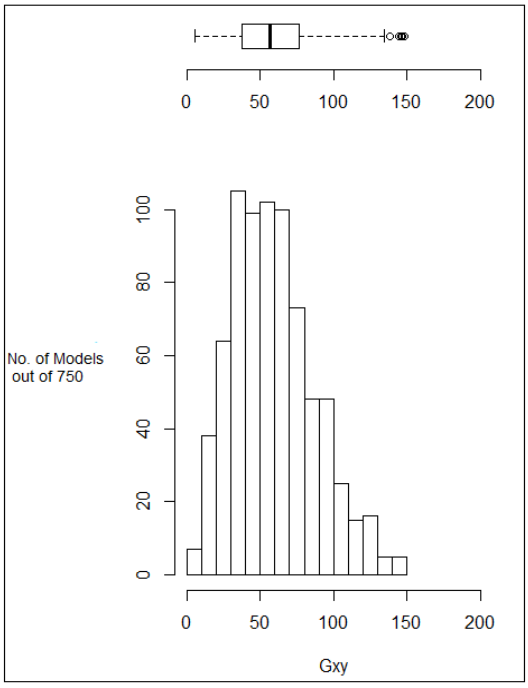

Figure 63: G_{xy} distribution

All Poisson's ratios appeared normally distributed; see Figure 64 and Figure 65. ν_{yz} (mean 0.18, SD 0.048), ν_{zy} (mean 0.182, SD 0.048) , ν_{xz} (mean 0.182, SD 0.046), ν_{zx} (mean 0.183, SD 0.047), ν_{xy} (mean 0.185, SD 0.048), ν_{yx} (mean 0.182, SD 0.047). Anisotropic ratio was found to be right-skewed; coefficient of skewness 1.27 (see Figure 66).

Distributions that exist due to random processes are often normally distributed. Skewness in the results suggests that an underlying physical mechanism is causing the random input to have a non-normal output. For instance, the orientation of the trabeculae (beams), i.e., for any randomized model the trabecula orientations are not uniform. It is likely that the non-uniformity of trabecula has a non-linear impact on the predicted mechanical properties. That is to say, when the trabecular are biased in one direction, the stiffness is non-linearly related to the degree of bias.

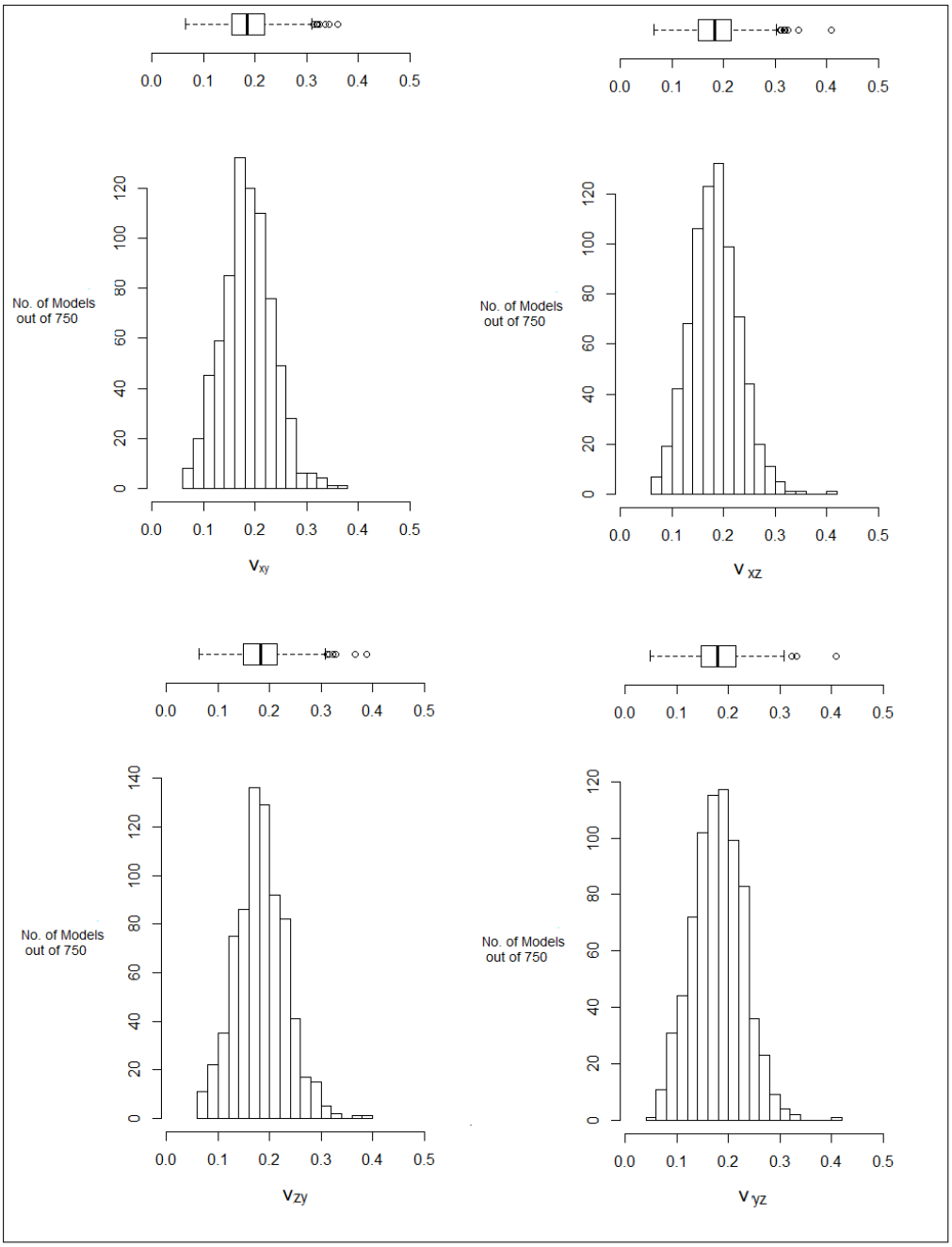

Figure 64: Poisson's ratios distributions

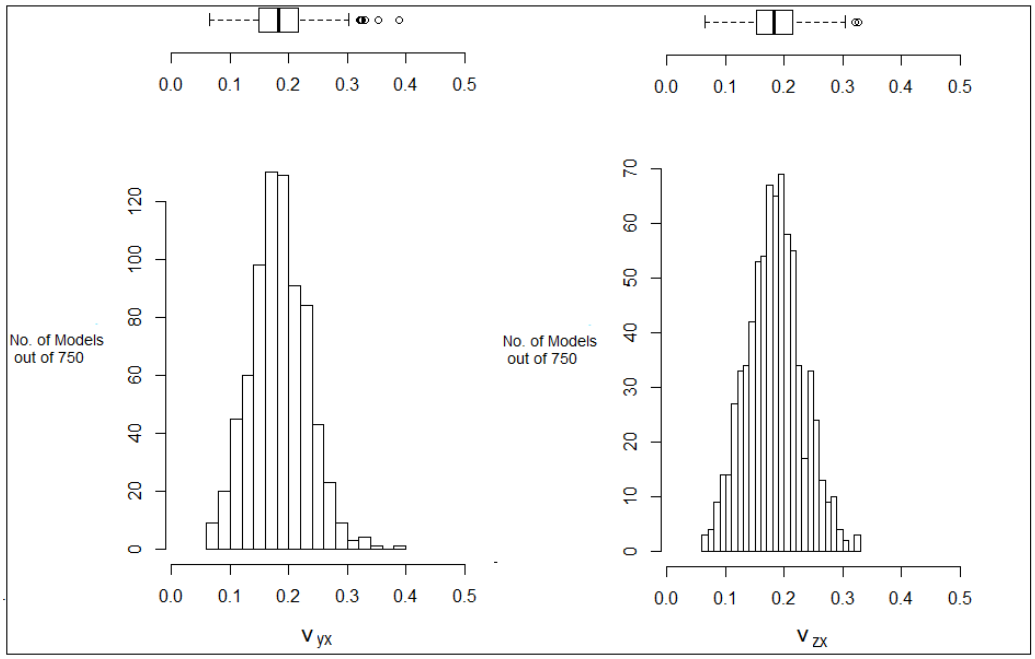

Figure 65: Poisson's ratios distributions (continued)

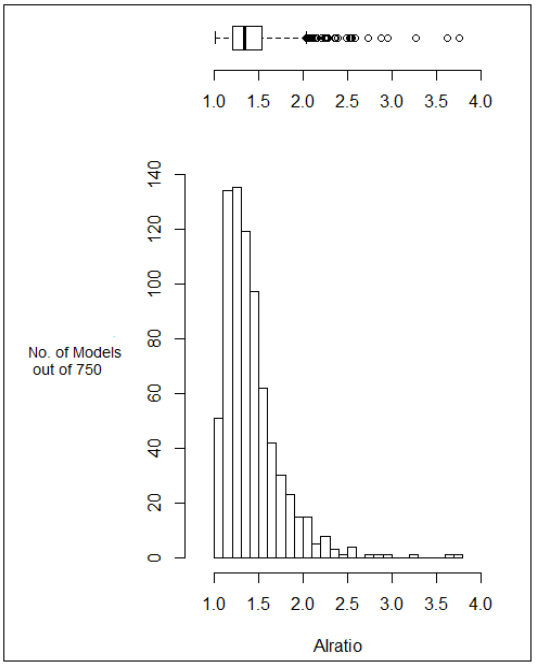

Figure 66: Anisotropic ratio distribution

Multivariate multiple linear regression resulted in statistical significant regression output. N_S was found highly correlated and significant to N_T (r=0.969, p< 2e-16), L_T (r=0.863, p< 2e-16) and ρ_{app} (r=0.978, p< 2e-16), (see Figure 67 and Figure 68). There was a low correlation and significance between A_T and (N_T, L_T). N_T (p=0.516), L_T (p=0.426) . On the contrary, A_T was found highly correlated to ρ_{app} (r=0.978, p< 2e-16), (see Figure 69 and Figure 70). E_{xx} was found correlated and significant to N_T (r=0.838, p=6.62e-10) and L_T (r=0.838, p=3.04e-6). Also, it was highly correlated to ρ_{app} (r=0.838, p< 2e-16), (see Figure 71 and Figure 72).

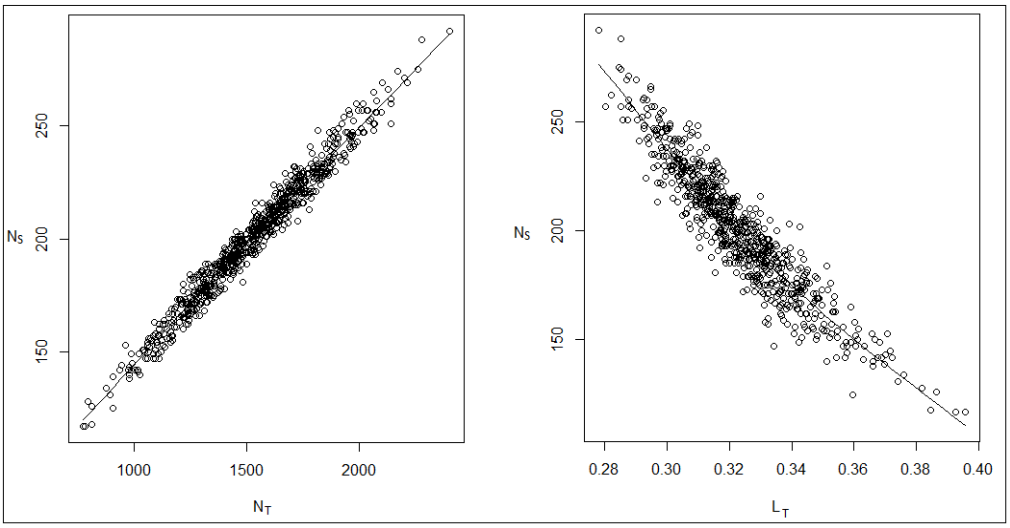

Figure 67: “No. of seeds” correlations with “No. of trabeculae” and “Trabeculae length”

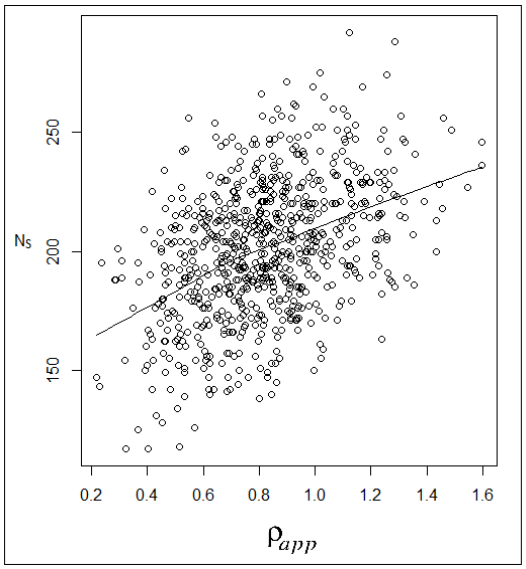

Figure 68: “No. of seeds” correlations with “Apparent denstiy”

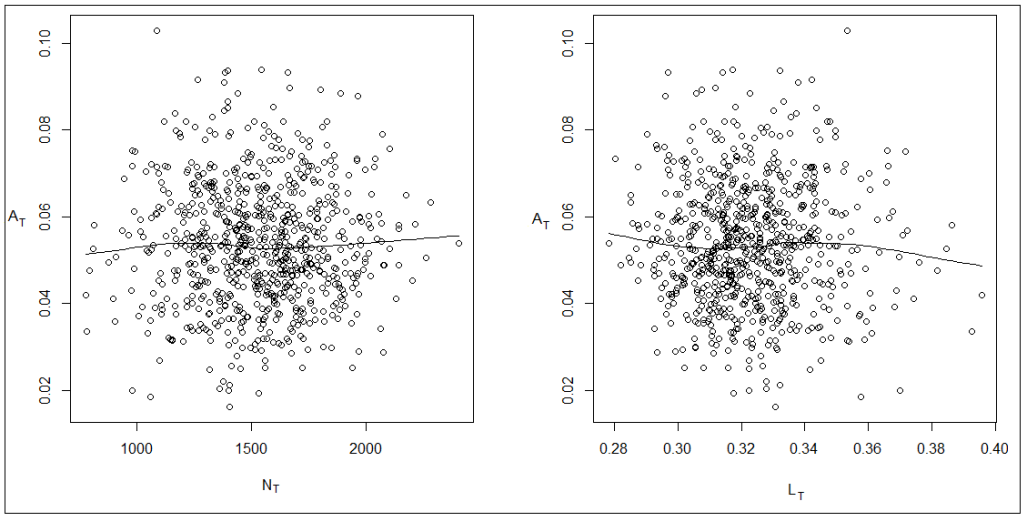

Figure 69: “Trabeculae cross section area” correlations with “No. of trabeculae” and “Trabeculae length”

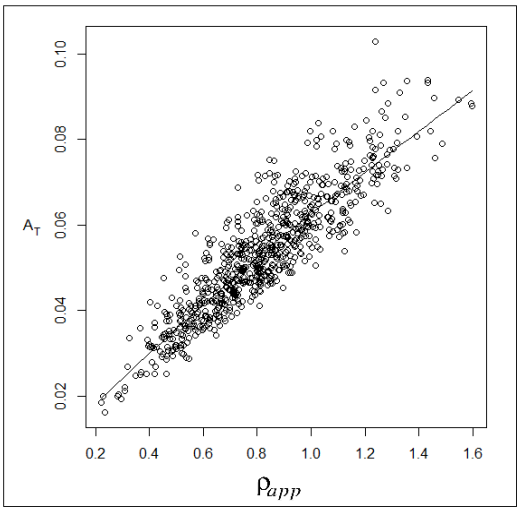

Figure 70: “Trabeculae cross section area” correlation with “Apparent denstiy”

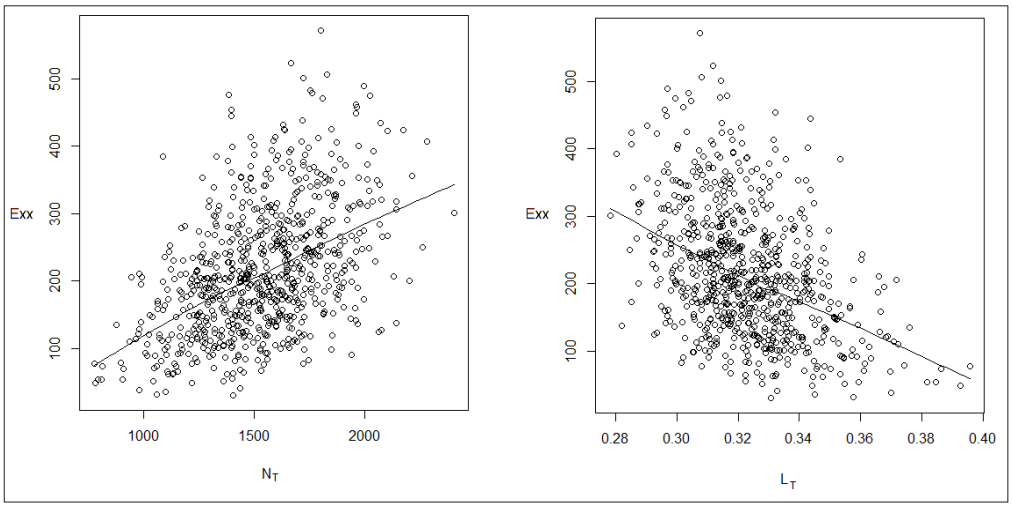

Figure 71: E_{xx} correlations with “No. of trabeculae” and “Trabeculae length”

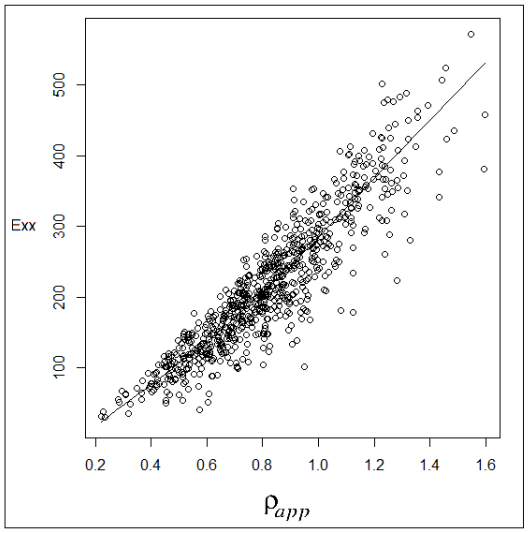

Figure 72: E_{xx} correlation with "Apparent denstiy"

All other normal and shear moduli were found correlated to N_T, L_T and ρ_{app} approximately the same correlation strength of E_{xx}. See other Young and shear moduli correlations in Appendix (A).

Poisson's ratio (ν_{xy}) was found not correlated but statistically significant to N_T (r=0.062, p=2.46e-07) and L_T (r=0.062, p=0.0002). Also, it was not correlated but significant to ρ_{app} (r=0. 062, p<7.82e-08), (see Figure 73 and Figure 74). Generally, ρ_{app} had no effect on Poisson's ratios; as ρ_{app} varied, Poisson's ratios were approximately constant, e.g. ν_{xy}. There was a value of N_T where Poisson's ratios reached a certain peak value.

For example, Poisson's ratio (ν_{xy}) reached a peak of (0.2) as N_T was close to (1600 trabecula), see Figure 73. Also, Poisson's ratios reached the same peak value (0.2) as L_T was close to (0.315 mm), e.g. ν_{xy}. All other Poisson's ratios had approximately the same correlation level of ν_{xy}. See Appendix (A).

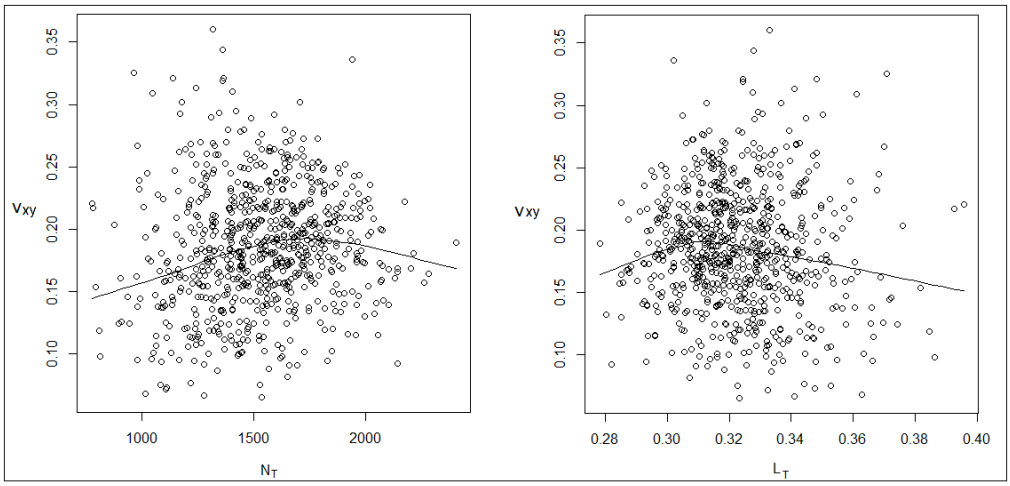

Figure 73: ν_{xy} correlations with "No. of trabeculae" and "Trabeculae length"

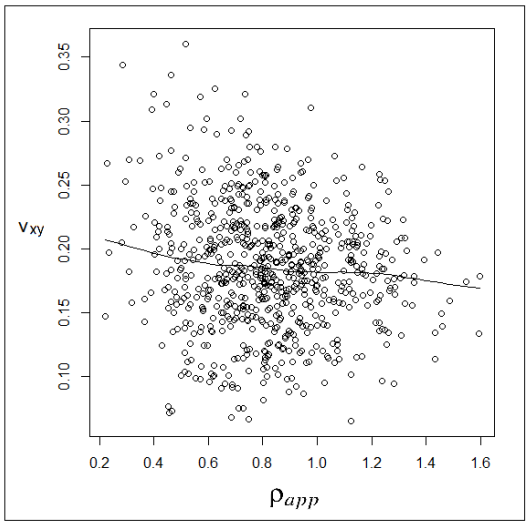

Figure 74: ν_{xy} correlation with "Apparent denstiy"

Anisotropic ratio was found only significant to NT (r=0.061, p=0.0007) but not correlated and not significant to LT (r=0.061, p=0.085). Also, it was only significant to some extent to ρapp (r=0. 061, p=0.048), (see Figure 75 and Figure 76).

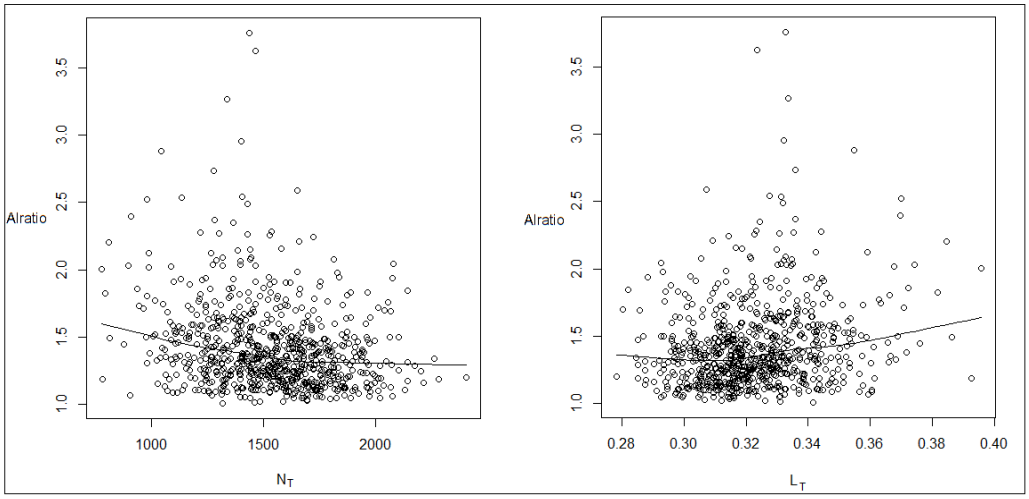

Figure 75: AIratio correlations with “No. of trabeculae” and “Trabeculae length”

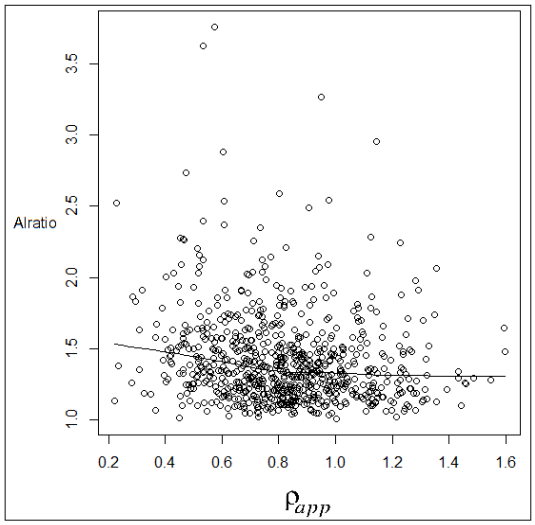

Figure 76: AIratio correlation with “Apparent denstiy”

A comparison between the results of the current work and the literature was made. Some of the FE models that simulated trabecular bone in chapter 2 are reported in this chapter, Table 11. This comparison may support the findings of the current study. Gross Young module was

found close to its values in the literature. Also, the trabecular length and cross section area were found close and similar, Table 11:

Table 11: Comparison between literature FE model and current study FE model

	Zhao et al. [36]	**Wang et al. [35]**	**Vanderoost et al. [23]**	**Wirth et al. [34]**	**Current study [16]**
Young Modulus (MPa)	N/A	E_{xx} (10-600), E_{yy} (10-800), E_{zz} (10-3000)	5-1750	96 - 384	27 - 340
Trabecular Length (mm)	0.1 - 1	N/A	N/A	N/A	0.198 – 0.88
Cross section Area (mm^2)	0.0007 - 0.041	N/A	N/A	N/A	0.01 – 0.0225

4.7.2 Proposed clinical procedure results

" N_S " and " A_T " were imported to the model; that was per each required apparent density, see equation (1) in section (4.4 Identifying FE model parameters). Hence, only five apparent densities have been targeted; (0.2, 0.4, 0.6, 0.8 and 1) g/cm^3. Per each apparent density, this procedure resulted intermediate and output parameters reported in Table 12. For further visualization, images of trabecular bone were provided for the five targeted apparent densities in Appendix (B). Every time the stochastic model was run, the model gave partially different random outcome. That was because of the randomness of voronoi diagram used in the current work. The similarity on average of the three normal elastic constants suggested a lack of bias in the random algorithm, though bias could be intentionally introduced to replicate spatially varying load dependent anisotropy.

Table 12: Model input / intermediate / output parameters*

Input Parameters		Intermediate Parameters			Some Output Parameters	
N_S	A_T	ρ_{app}	N_T	L_T	E_{xx}	G_{yz}
270	0.01	0.19	2177	0.7	26.44	7.4285
635	0.01	0.38	5872	0.55	81	21.23
390	0.02	0.59	3357	0.6	149.89	39.99
580	0.02	0.81	5298	0.57	217.82	56.02
800	0.02	1.04	7621	0.45	330.02	85.61

*All values are "mean". $A_T(mm^2)$, $\rho_{app}(g/cm^3)$, E-G(MPa), most ocurring.L_T (mm)

The difference among the elastic constants within a single model exhibited anisotropy consistent with localized trabecular architecture [49]. This study was conducted to cover the range of the apparent density of the literature, ($0.1 \sim 1$ g/cm^3) [51] [52].

Once the medical doctor asks for a certain apparent density, the apparent density can be matched with its equivalent from Table 13. Then the input parameters are known to be set and input to the model. As a result the model will represent trabecular bone of the same provided density, see Figure 56 (C).

Table 13: Apparent density / model input*

Provided ρ_{app}	Input Parameters		Delivered ρ_{app} by the model
	N_S	A_T	
0.2	270	0.01	0.19
0.4	635	0.01	0.38
0.6	390	0.02	0.59
0.8	580	0.02	0.81
1	800	0.02	1.04

*All values are "mean". $A_T(mm^2)$, $\rho_{app}(g/cm^3)$

4.8 Discussion

The facts that trabecular bone has a complicated porous random micro-structure and its microstructural properties govern its overall behavior; indicating that micromechanical simulations may provide advantages over traditional homogenized continuum models. The trabecular bone has been mostly modeled as a continuum substance in the literature. The most frequently utilized method for mimicking the spongy bone microstructure is the conversion of CT images into a FE model using volume elements. In the current study, beam elements were used instead to simulate trabecular bone microstructure. The current method might be inexpensive because beams elements were easier to mesh and less prone to negative jacobian errors, which might occur when using extremely thin solid features. Also, beam elements were more efficient in capturing bending loads as one element.

This method could provide more than one model by controlling numbers of seeds and trabeculae cross-section area. The resulted homogenized mechanical properties and apparent densities showed a good agreement with the expectations. The models illuminated the stochastic relationship among the model input, the intermediate model parameters and model output. The intermediate model parameters (the number of trabeculae; trabeculae length and apparent densities) were quasi-stochastically dependent on the model inputs (number of seeds and trabecula cross-section area). In addition, the mechanical properties (model output) were dependent on the intermediate model parameters.

The results showed that the number of seeds was directly proportional to the number of trabeculae and apparent densities. Simultaneously, the number of seeds was inversely proportional to the length of trabeculae. While, trabeculae cross-sectional area was directly proportional to only the apparent densities. As would be expected in two random variables, trabeculae cross-sectional area was not proportional to the number of trabeculae and length of trabeculae. The apparent moduli of trabecular bone were directly proportional to the number of trabeculae and apparent densities. On the contrary, they were inversely proportional to the length of trabeculae. Generally, Poisson's ratios were not significantly affected by model inputs.

In the current models, anisotropic ratio correlation to the length of the trabeculae was weak; however, anisotropic ratio could be dependent on the number of the trabeculae in a model. The anisotropic ratio might increase considerably above 1 for a high number of trabeculae. As if a larger specimen (larger than the 4 mm^3 cube) was considered, anisotropic ratio might approach one. The reason was due to the distribution of the trabeculae lengths in a bigger space. Since, the length of trabeculae was inversely proportional to the number of seeds and the apparent density;

this supported the fact that anisotropic ratio was also inversely proportional to the number of seeds and the apparent density. The advantages and disadvantages of the present methodology are listed below:

Advantages**:**

1. The method provides an automatic process to generate a stochastic model with simplified structural elements, i.e., beam elements.
2. This method requires only minimal parameters from the patient to generate the model. The minimum required input is the bone density distribution of the patient obtainable from CT, bone density scan, or assumption.
3. For the model calibration as described, the boundary conditions and setup of the model is automatic and require very little interaction to run.
4. Parameter and sensitivity studies can be implemented by adding relatively simple functions to the mesh generation algorithm.
5. Different material properties can be applied to the beams and explore multiple scenarios as appropriate for different patient populations in different clinical studies.
6. The method is likely less costly to run than detailed microstructural models generated using continuum elements. Further, the method can be repeated many times generating a distribution of expected outcomes, whereas a distribution of conventional microstructural model cannot be easily generated.

Disadvantages:

1. The mesh generated by this model is only loosely dependent on medical imaging (through density). In other words, it does not replicate the exact trabecular bone micro structure of the patient. However, it does provide a stochastic distributions of response (when several models are run) that can be generalized to provide patient specific clinical recommendations.
2. Depending on the FEA solver, the code may require some changes to address the syntax of boundary conditions, application of loads, and generation of the elements.
3. The method is likely more costly to run than traditional continuum methods which may have fewer nodes and fewer degrees of freedom due to homogenization.

In addition to the methodological disadvanges described above, the limitations of this study are as follows: (1) the trabeculae were assumed as linear elastic isotropic though they might have non-linear responses near damage initiation. (2) Damage is not modeled. Damage is an important part of fracture and other morbidities. (3) The meshing algorithm had two problems which were not identified early enough for fixes to be incorporated into the results presented in this dissertation. First, there were some extremely small trabeculae "beams" that do not have a physical analog. These small elements occurred when random seed locations were very close to each other. Second, the boundary of the mesh had some gaps were elements were not generated to cross the boundary. The impact of these algorithmic deficiencies is expected to be small, however, it has not been quantified. (4) Only an apparent density target of (0.8 g/cm^3) has been thoroughly investigated using normally distributed inputs. A uniform distribution of seeds would provide a broader spectrum of resulting apparent densities (5) The cross sectional areas of the trabecula are assumed constant at fixed values per density target. This is not an accurate

representation of patient trabecular architecture and thus limits the generalizability of the results. (6) No clear method of choosing algorithm inputs (number of seeds, cross sectional area) based on patient inputs has been described.

4.9 Conclusions

A method of stochastic modeling of trabecular bone is presented. The proposed stochastic model produces homogenized mechanical properties that are within the range of literature. Hence, the model can provide a good distribution of bone mechanical properties based on bone density. Beam elements give a well representation of trabeculae and their reaction to applied loads. This method may incorporate several advantages of high fidelity methods but at computationally lower cost and requiring only clinical imaging. The apparent mechanical properties and apparent densities are found to be sensitive to number of trabeculae; trabeculae lengths and trabeculae cross-sectional area. The stochastically driven beam element approach may prove useful for efficiently modeling the microstructure of trabecular bone, structural open cell foams and grid stiffened core composites. Consequently, this model can be a baseline for further modeling investigations through biasing the model parameters; such as interaction with mechanical fasteners, bonding, damage evolution, the modeling of osteoporosis and bone remodeling (Wolff's law).

CHAPTER V

CONCLUSIONS AND FUTURE WORK

5.1 Introduction

In the present dissertation, the biomechanics of subtalar joint arthrodesis with the use of screws was explored in chapter 3. As individual tissues “such as trabecular bone” influence the biomechanics of subtalar joint; a new method of modeling trabecular bone was discussed in chapter 4. Subsequently, this chapter addresses the summary of contributions of the current work and presents some proposals/recommendations for future research.

5.2 Present work contributions

The contributions of the present work are described as follows: (1) Fused subtalar joint synthetic specimens were tested about eversion/inversion axis of rotation including different screw configurations to estimate joint torsional stiffness. Fused subtalar joint mechanics is a complex contact problem and surrogate testing models are essential for validation and investigation of simultaneously loaded models in different axes of rotations, as opposed to only in the eversion/inversion axis. There are many models in the literature about the joint mechanics, i.e., the fused joint tested about other axes of rotations (adduction/abduction, external / internal … etc); all of which did not fully addressed all other important mechanical considerations. In addition, the axes of rotation of the joint are difficult to identify and vary from patient to patient. Also, this study supports the hypothesis: double divergent screw configuration is a biomechanically more effective and potentially safe replacement for fusion and fixation goals.

These considerations and others, have critical clinical implications in sports medicine and recovery. (2) In the current study, structural beam elements were used to simulate trabeculae at the micro scale, instead of solid volume continuum elements. The current study provides an initial structural model to simulate trabecular bone using a stochastic method to generate a random mesh. The method provides homogenized mechanical properties and estimated clinical measurements (i.e. averaged density). The model does require further improvements to create a high fidelity model, validating the model, and enhancing material modeling capabilities to accurately predict bone mechanical properties. The revised literature still has shortcomings in creating a high fidelity model that fully simulates the trabecular bone with accurate results, low cost and computational time.

5.3 Recommendations

Despite of the contributions and the limitations of the current work, recommendations for the future work are discussed in the next following subsections.

5.3.1 Extreme small beams

The extreme small beams in the mesh can be eliminated. That may be done by merging the nodes of those small beams. Also, a conditional statement that determines the minimum beams length can be imposed in the code that generates the mesh.

5.3.2 Boundary mesh

The non-homogenous beams orientations at the boundary of the mesh exist because there was a problem in cutting the (4 mm X 4 mm X 4 mm) specimen. Some of the beams were

normally cut and others were entirely removed. This problem has been resolved but the model results have not been regenerated due to time limitations, see Figure 77. Whenever further research improvements may conduct, the corrected mesh has to be used when running the models. Futher, it is recommended that the results published in this work be confirmed through rerunning the models with improved boundary meshes.

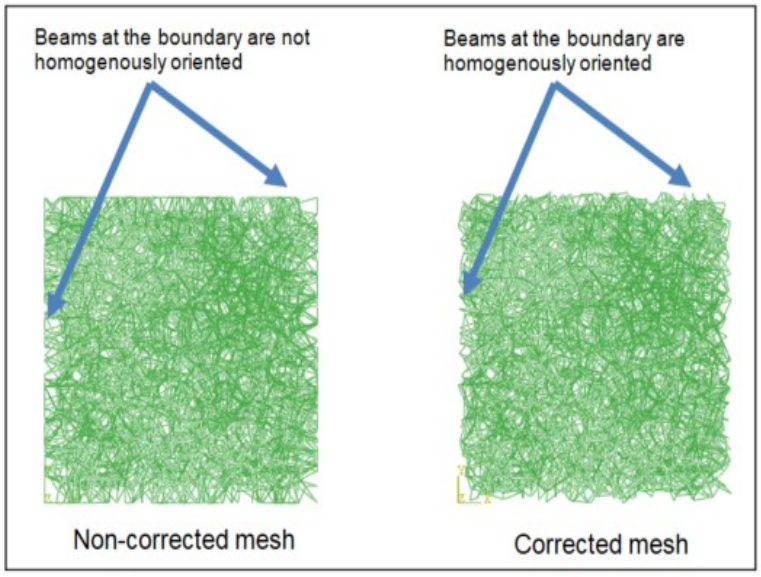

Figure 77: Correcting mesh boundaries

5.3.3 High order beams elements

The 2 noded beam elements used in this work are likely insufficient for capturing buckling phenomena. Beam elements of higher order can be used and would provide more flexibility within the single element trabula model. That may increase the quality of capturing the bending and buckling response of the trabecula.

5.3.4 Shell elements

Trabecular bone contains rod-like and plate-like microstructures, however, the currently reported method does not explicitly provide plate-like structural model. Simulating trabeculae using shell elements in addition to beam elements may be useful in better mimicking real bone structure.

5.3.5 Osteoporosis modeling

The stochastic beam element approach may be useful for patient specific musculo-skeletal biomechanical models (e.g. osteoporosis, osteoarthritis, joint replacement and implants interface). For instance, osteoporosis can be modeled by reducing cross section area of the trabeculae where osteoporosis exists. Cross section area reduction would mimic the trabeculae become thinner. Depending on osteoporosis severity, trabeculae can vanish which could be modeled via element elimination.

5.3.6 Wolff's law modeling

Bone remodels in response to applied load (Wolff's law). This can be modeled using the stochastic beam element technique if a set of remodeling rules is constructed to define the mechanism and rate of the remodeling process. Using a set of relations or equations, the stochastic beams can be biased such that they can be enforced to orient toward the load direction in space. Further, the cross sectional areas can adapt to the localized load transmission. This might provide insight triggering mechanisms for bony adaptation.

5.3.7 Bone failure modeling

Modeling bone failure was not been implemented in the current work. Failure modeling is highly recommended to be modeled because damage accumulation enhances model predictions.

5.3.8 Trabeculae cross section area modeling

In real trabecular bone, trabeculae cross-section areas vary both within individual trabecula and across different trabecula. However, area has been assumed constant (within and across trabecula) in the current study. Nevertheless, the method in the present study is flexible to add variable cross-section area of trabeculae (beams). Ultimately, stochastic distributions of area can be employed to determine its overall impact, see Figure 78. Furthermore, the currently method of target density with number of seeds does not cover the entire apparent density range (0.1~1.1 g/cm^3). Additional models should be run with a uniform density of number of seeds to more clearly identify the impact on mechanical property outputs.

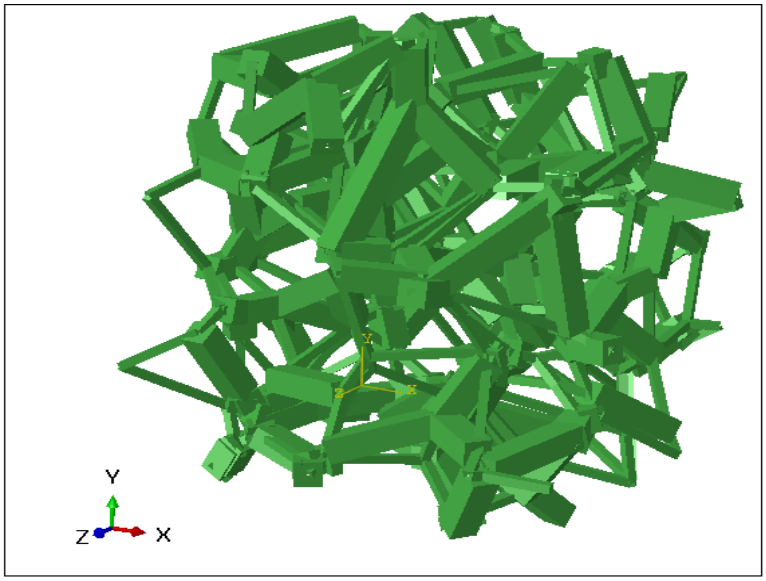

Figure 78: Trabecular bone model with variable cross-section area (A_T)

5.3.9 Cortical/trabecular bone modeling

Modeling cortical and trabecular bones as a “hybrid” structure. A computer tomography, CT scan, of a healthy foot and ankle of an adult was provided by Kalamazoo Orthopaedic Clinic / Borgess Medical Center. The anatomical details of the foot and ankle bone specimen were obtained using a CT, Figure 79. Scanning was conducted such that the slice to slice distance was approximately 0.5 mm. The data from the CT scan were processed by the CT medical imaging software, 3D Slicer (V 4.8.1), and converted into STL files, Figure 80. The anatomical surfaces were obtained from Digital Imaging and Communications in Medicine (DICOM) files of the CT scan.

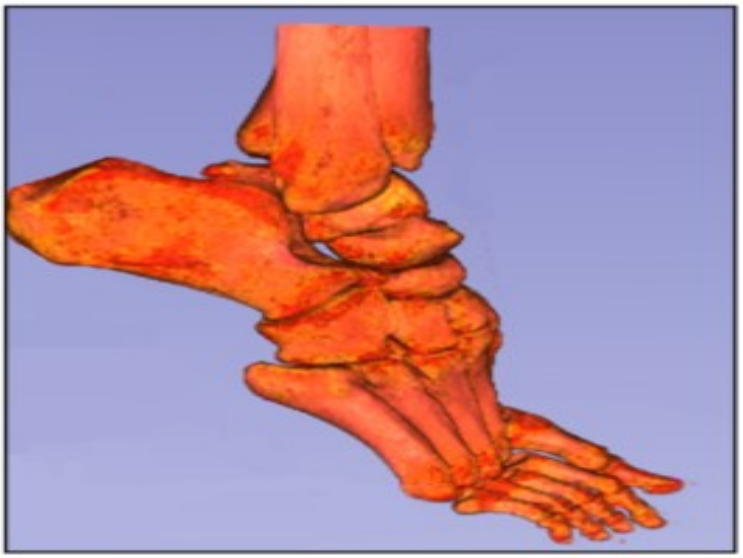

Figure 79: Foot and ankle medical image

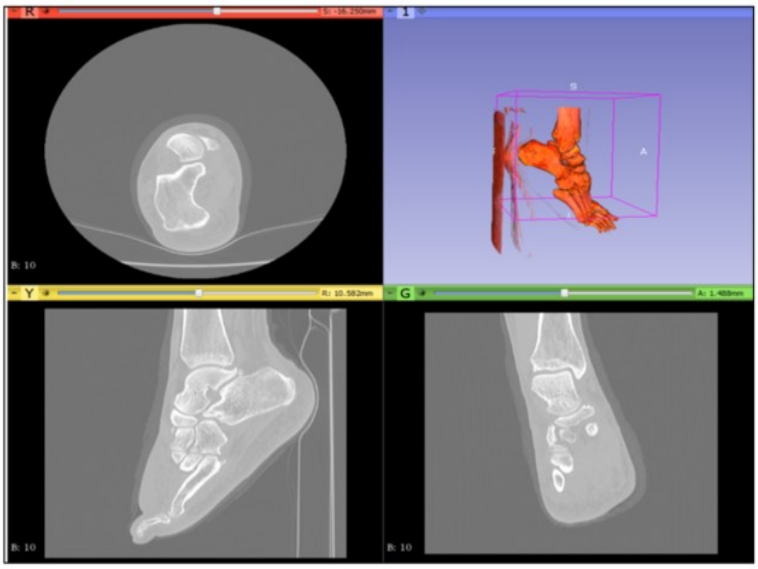

Figure 80: CT scan of foot and ankle (3D slicer)

The subtalar joint was manually segmented from the entire structure of the foot using 3D Slicer, Figure 81 and Figure 82. Segmentation was employed to differentiate each anatomical volume by creating voxels. Cortical bone was kept and considered as continuum. Trabecular bone was removed and would be replaced later by a structural (non-continuum) structure. Structural trabecular bone was taken from chapter 4. Also, subtalar joint surface was smoothed by a series of surface smoothing processes using 3D Slicer. Smoothing processes removed rough undesired ridges and spikes of the surface and provided a softer topology analogues to the joint anatomy, Figure 83. After performing segmentations and smoothing operations, the subtalar joint specimen was of only the cortical bone. In this case, cortical bone consisted of two separated surfaces within the volume space of subtalar joint. Next, the subtalar joint was separated into two parts; Calcaneus and Talus, Figure 84.

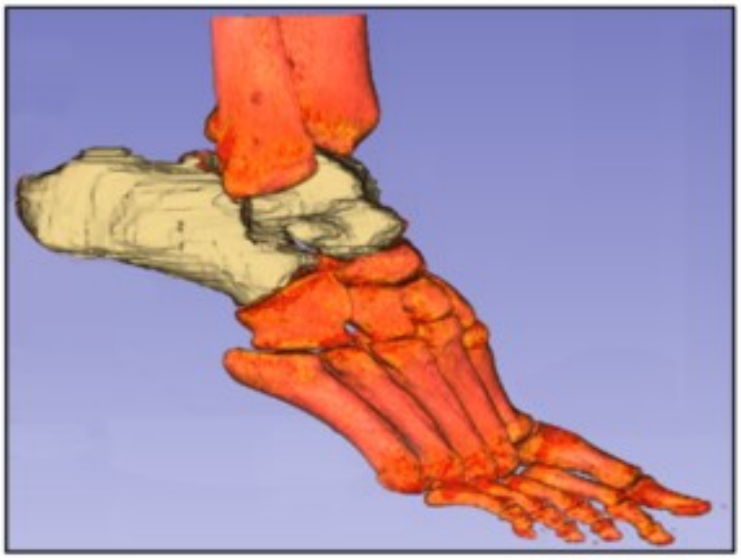

Figure 81: Segmenting subtalar joint

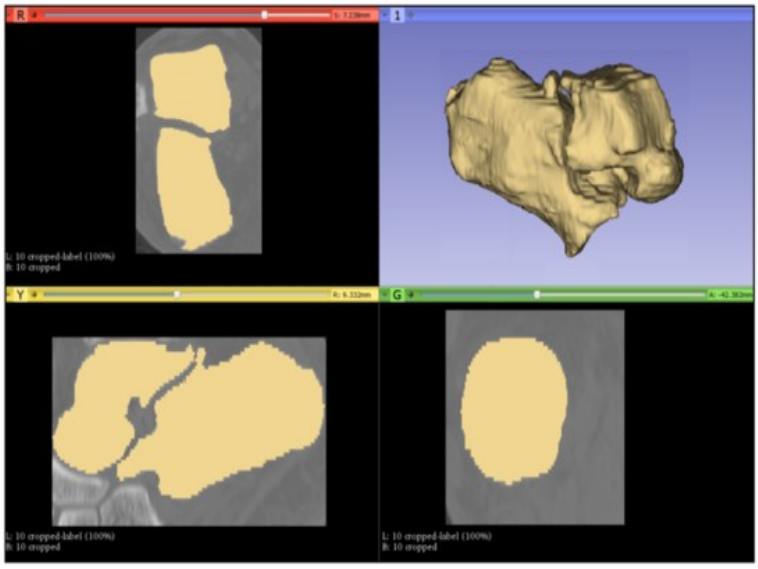

Figure 82: Segmenting subtalar joint (3D slicer)

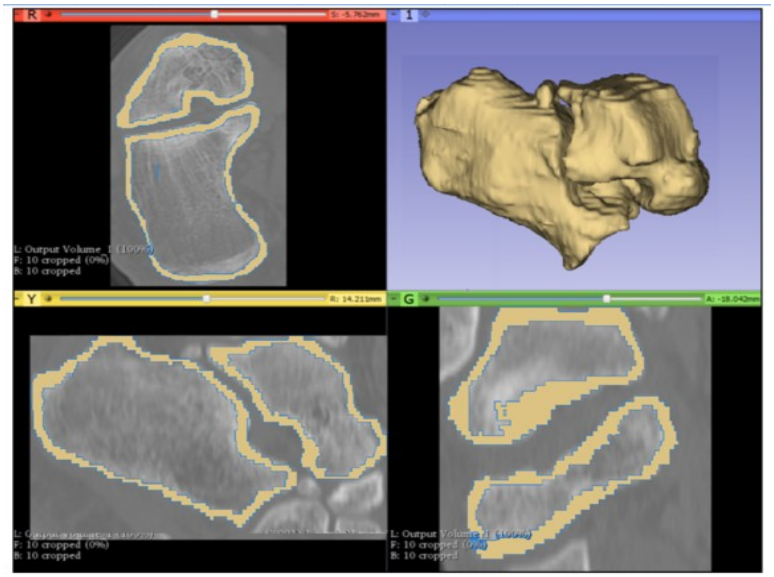

Figure 83: Segmenting trabecular bone (leaving cortical)

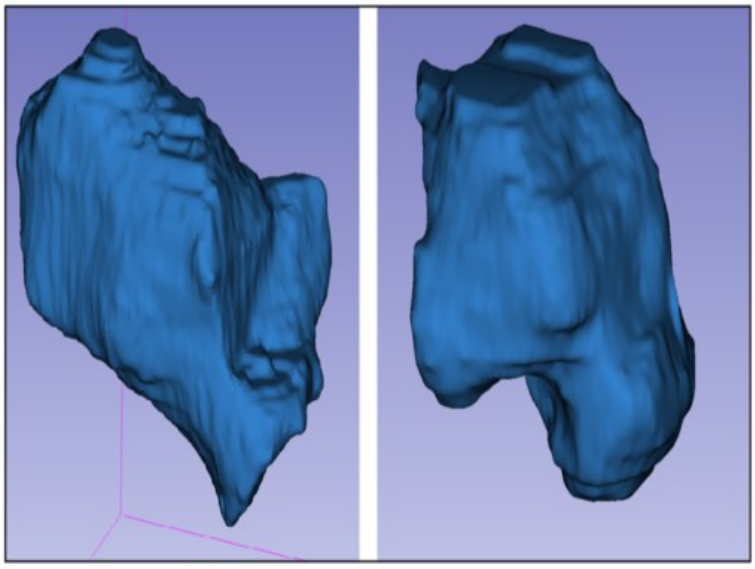

Figure 84: Calcaneus and talus (medical image)

Utilizing 3D Slicer, Calcaneus and Talus were exported as STL files for further processing. The surfaces of the cortical bone of the Calcaneus and the Talus were composed of a triangular elements mesh within the STL files. The STL files were imported to Gmsh (V. 3.0.6). Gmsh is software used for handling triangular and tetrahedral meshes. A 3D tetrahedral mesh was generated between both surfaces of the cortical bone; that was for both Calcaneus and Talus. The last procedure helped to end with Calcaneus and Talus consisting of only cortical bone; hence the cortical bone was meshed with tetrahedral elements, Figure 85. Calcaneus and Talus were exported from Gmsh as INP files.

Figure 85 shows the empty space resulting from cortical bone segmentation. The empty space is dedicated for implementing structural trabecular bone. Once the cortical bone is

modeled with trabecular bone, the final mesh may appear as in the mesh shown in Figure 86 and Figure 87.

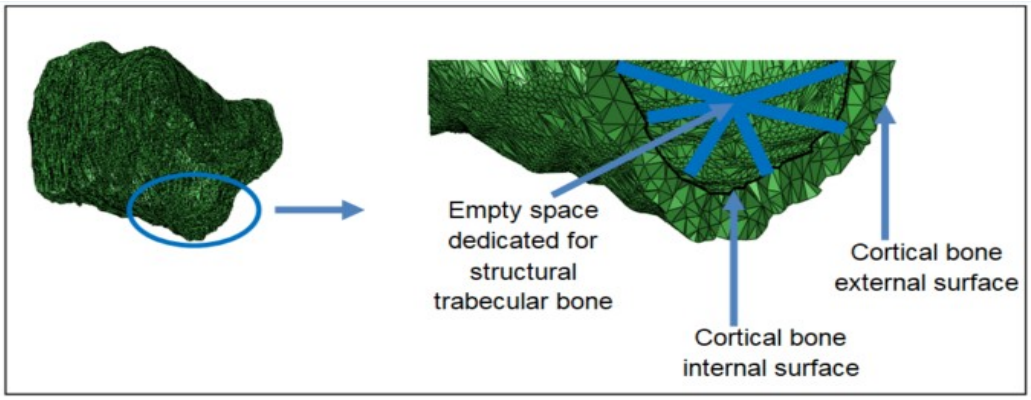

Figure 85: Calcaneus with only cortical bone (mesh)

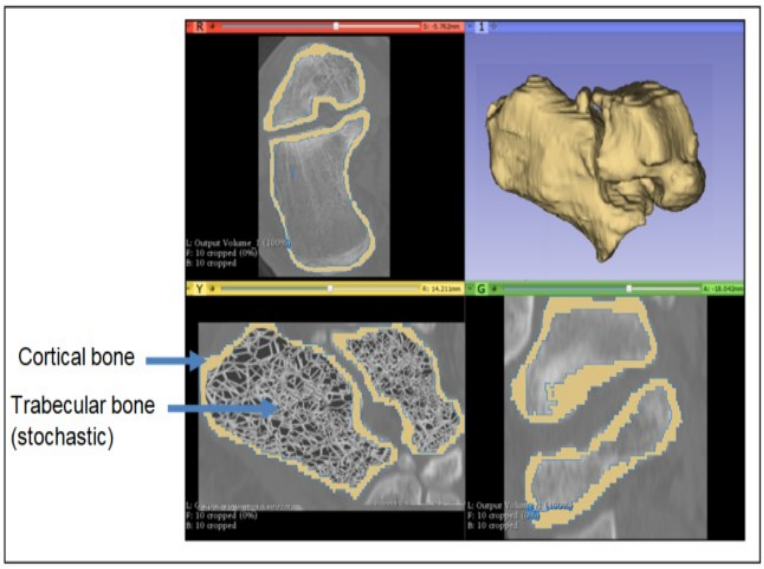

Figure 86: Representative image of continuum / structural "hybrid" model of subtalar joint

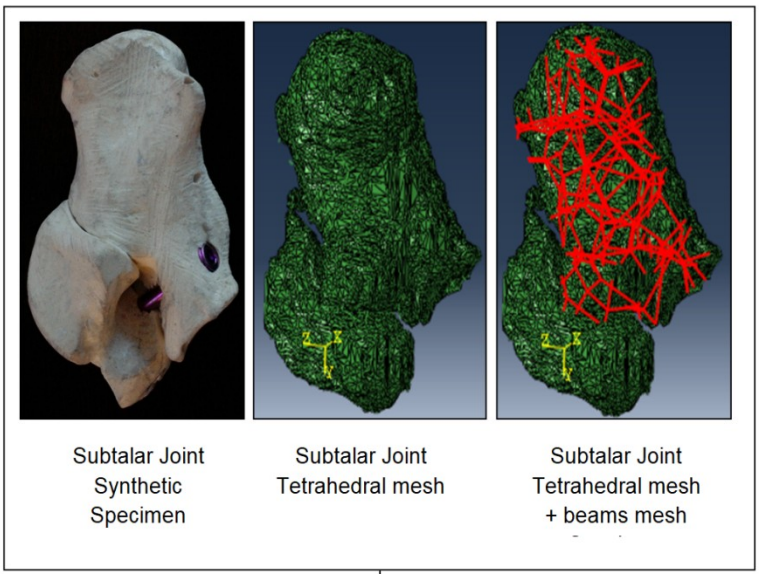

Figure 87: Subtalar joint preliminary mesh (continuum / structural)

5.3.10 Cortical/trabecular bone and screw modeling

Modeling of cortical and trabecular bones with screws. Typically, screws are inserted into a bone where cortical and trabecular bones are modeled together as one unit to better represent screw insertion in bones. Hence, the hybrid model has not been modeled yet. Therefore, a preliminary model was created to anticipate future work. Cortical bone was modeled as continuum cylinder while trabecular bone was modeled as a set of unit cells constructed from beams "repetitive unitcell". In addition, the screw was modeled as continuum, see Figure 88 and Figure 89. The contact between the screw and the trabecular bone was modeled as a tie constrain.

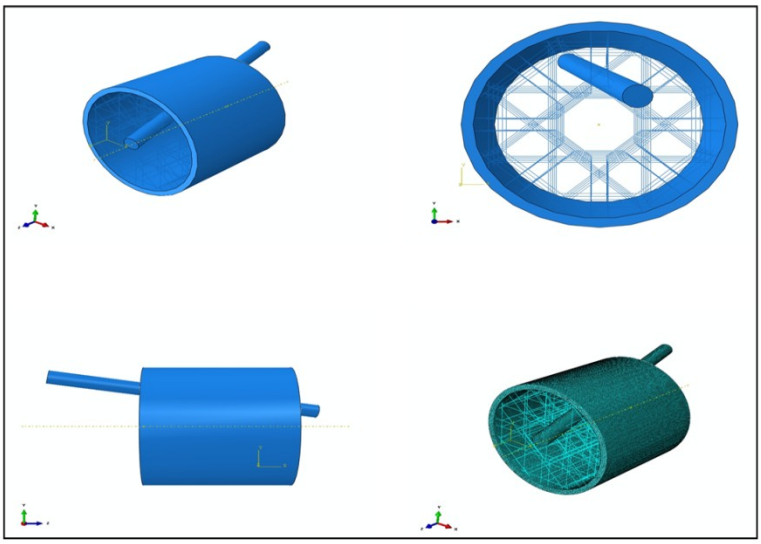

Figure 88: Modeling of cortical and trabecular bones with screws

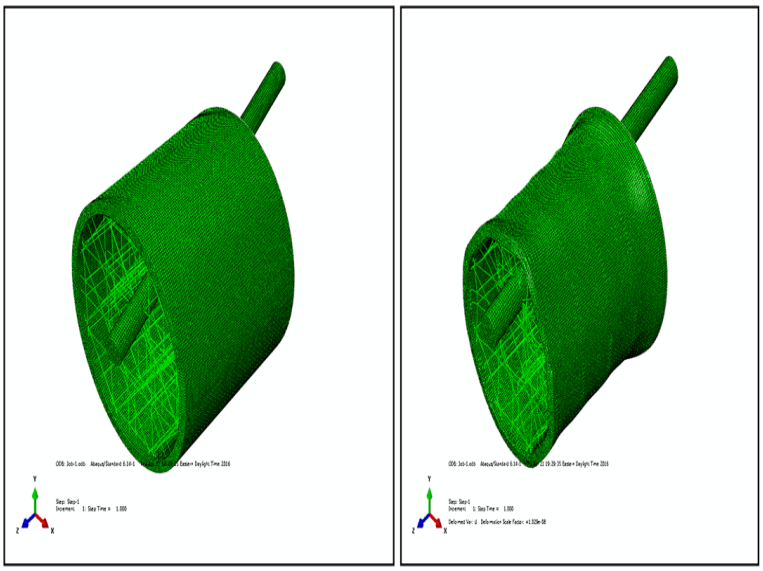

Figure 89: Preliminary results of modeling bone and screws

REFERENCES

[1] A. Asadi, “How it works. Book of The Human Body,” *Imagine Publishing Ltd*, UK, 2014.

[2] A. Pernet, “Biomechanics of the hand.,” *Int. Surg.*, vol. 60, no. 1, pp. 9–11, 1975.

[3] G. B. Wilkerson, “Ankle Derotation and Subtalar Stabilization Orthosis,” US 2008 / 0082034 A1, 2008.

[4] T. M. K. Donald L. Bartel, Dwight T. Davy, *Orthopedic biomechanics (mechanics and design in musculoskeletal systems)*, 1st ed. Michigan: Pearson Education Inc., 2006.

[5] “Vector - Long bone structure.” [Online]. Available: https://www.123rf.com/photo_52435816_stock-vector-long-bone-structure.html.

[6] M. Tanaka, S. Wada, and M. Nakamura, *Computational biomechanics: Theoretical background and biological/biomedical problems*. 2012.

[7] L. Podshivalov, A. Fischer, and P. Z. Bar-Yoseph, “On the Road to Personalized Medicine: Multiscale Computational Modeling of Bone Tissue,” *Arch. Comput. Methods Eng.*, 2014.

[8] S. Park, S. W. Chae, J. Park, S. H. Han, J. Hong, and Y. E. Kim, “Finite element modeling to estimate the apparent material properties of trabecular bone,” *Int. J. Precis. Eng. Manuf.*, 2013.

[9] T. R. Chandrupatla and A. D. Belegundu, *Introduction to finite elements in engineering*, 3rd ed. Prentice Hall, 2002.

[10] A. Erdemir, T. M. Guess, J. Halloran, S. C. Tadepalli, and T. M. Morrison, “Considerations for reporting finite element analysis studies in biomechanics,” *Journal of Biomechanics*. 2012.

[11] P. K. Zysset, E. Dall'Ara, P. Varga, and D. H. Pahr, "Finite element analysis for prediction of bone strength," *Bonekey Rep.*, 2013.

[12] R. De Borst, L. J. Sluys, H. B. Mühlhaus, and J. Pamin, "Fundamental issues in finite element analyses of localization of deformation," *Engineering Computations*. 1993.

[13] "Theoretical and computational poromechanics laboratory." [Online]. Available: https://poromechanics.weebly.com/research.html.

[14] T. Adachi, Y. Tomita, and M. Tanaka, "Three - Dimensional Lattice Continuum Model of Cancellous Bone for Structural and Remodeling Simulation," *JSME* , vol. 42, no. 3, pp. 470–480, 1999.

[15] J. R. Jastifer, S. Alrafeek, P. Howard, P. A. Gustafson, and M. J. Coughlin, "Biomechanical Evaluation of Strength and Stiffness of Subtalar Joint Arthrodesis Screw Constructs," *Foot Ankle Int.*, 2016.

[16] S. Alrafeek, J. R. Jastifer, and P. A. Gustafson, "A Stochastic Structural Finite Element Model for Trabecular Bone and other Structural Foam," 2018.

[17] W. C. H. Parr, U. Chamoli, A. Jones, W. R. Walsh, and S. Wroe, "Finite element micro-modelling of a human ankle bone reveals the importance of the trabecular network to mechanical performance: New methods for the generation and comparison of 3D models," *J. Biomech.*, 2013.

[18] C. N. S. Yuan, W. Chen, C. Chen, G. N. H. Yang, C. Hu, and K. N. L. Tang, "Effects on Subtalar Joint Stress Distribution After Cannulated Screw Insertion at Different Positions and Directions," *J. Foot Ankle Surg.*, 2015.

[19] B. Chuckpaiwong, M. E. Easley, and R. R. Glisson, "Screw Placement in Subtalar

Arthrodesis: A Biomechanical Study," *Foot Ankle Int.*, 2009.

[20] S. Hungerer *et al.*, "Biomechanical Evaluation of Subtalar Fusion: The Influence of Screw Configuration and Placement," *J. Foot Ankle Surg.*, 2013.

[21] M. Riedl, R. R. Glisson, T. Matsumoto, S. G. Hofstaetter, and M. E. Easley, "Torsional stiffness after subtalar arthrodesis using second generation headless compression screws: Biomechanical comparison of 2-screw and 3-screw fixation," *Clin. Biomech.*, 2017.

[22] D. Ulrich, B. Van Rietbergen, H. Weinans, and P. Rüegsegger, "Finite element analysis of trabecular bone structure: A comparison of image-based meshing techniques," *J. Biomech.*, 1998.

[23] J. Vanderoost *et al.*, "A validated skeleton-based finite element mesh for parametric analysis of trabecular bone competence," in *IFMBE Proceedings*, 2008.

[24] M. A. M. Althomali, M. L. Wille, M. P. Shortell, and C. M. Langton, "Estimation of mechanical stiffness by finite element analysis of ultrasound computed tomography (UCT-FEA); a comparison with X-ray μCT based FEA in cancellous bone replica models," *Appl. Acoust.*, 2018.

[25] S. P. Evans, W. C. H. Parr, P. D. Clausen, A. Jones, and S. Wroe, "Finite element analysis of a micromechanical model of bone and a new 3D approach to validation," *J. Biomech.*, vol. 45, pp. 2702–2705, 2012.

[26] B. Depalle, R. Chapurlat, H. Walter-Le-Berre, B. Bou-Sa, and H. Follet, "Finite element dependence of stress evaluation for human trabecular bone $," *J. Mech. Behav. Biomed. Mater.*, vol. 18, pp. 200–212, 2013.

[27] J. Schwiedrzik, T. Gross, M. Bina, M. Pretterklieber, P. Zysset, and D. Pahr,

"Experimental validation of a nonlinear μFE model based on cohesive-frictional plasticity for trabecular bone," *Int. j. numer. method. biomed. eng.*, 2016.

[28] I. Goda, M. Assidi, S. Belouettar, and J. F. Ganghoffer, "A micropolar anisotropic constitutive model of cancellous bone from discrete homogenization," *J. Mech. Behav. Biomed. Mater.*, 2012.

[29] I. Goda, M. Assidi, and J. F. Ganghoffer, "A 3D elastic micropolar model of vertebral trabecular bone from lattice homogenization of the bone microstructure," *Biomech. Model. Mechanobiol.*, 2014.

[30] T. J. Vaughan, C. T. McCarthy, and L. M. McNamara, "A three-scale finite element investigation into the effects of tissue mineralisation and lamellar organisation in human cortical and trabecular bone," *J. Mech. Behav. Biomed. Mater.*, 2012.

[31] S. Ilic, K. Hackl, and R. Gilbert, "Application of the multiscale FEM to the modeling of cancellous bone," *Biomech. Model. Mechanobiol.*, 2010.

[32] M. Tanaka and T. Adachi, "Lattice Continuum Model for Bone Remodeling Considering Microstructural Optimality of Trabecular Architecture," in *IUTAM Symposium on Synthesis in Bio Solid Mechanics*, .

[33] J. Vanderoost *et al.*, "Fast and accurate specimen-specific simulation of trabecular bone elastic modulus using novel beam-shell finite element models," *J. Biomech.*, vol. 44, no. 8, pp. 1566–1572, 2011.

[34] A. J. Wirth, R. Müller, and G. Harry van Lenthe, "The discrete nature of trabecular bone microarchitecture affects implant stability," *J. Biomech.*, 2012.

[35] J. Wang *et al.*, "Trabecular plates and rods determine elastic modulus and yield strength of

human trabecular bone," *Bone*, 2015.

[36] F. Zhao, M. Kirby, A. Roy, Y. Hu, X. Edward Guo, and X. Wang, "Commonality in the microarchitecture of trabecular bone: A preliminary study," *Bone*, 2018.

[37] L. Podshivalov, A. Fischer, and P. Z. Bar-Yoseph, "3D hierarchical geometric modeling and multiscale FE analysis as a base for individualized medical diagnosis of bone structure," *Bone*, 2011.

[38] Y. W. Kwon and B. R. Clumpner, "Multiscale modeling of human bone," *Multiscale Multidiscip. Model. Exp. Des.*, vol. 1, pp. 133–143, 1939.

[39] T. D. Rozental, F. Johannesdottir, K. C. Kempland, and M. L. Bouxsein, "Characterization of trabecular bone microstructure in premenopausal women with distal radius fractures."

[40] W. C. H. Parra, H. J. Chatterjee, and C. Soligo, "Calculating the axes of rotation for the subtalar and talocrural joints using 3D bone reconstructions," *J. Biomech.*, 2012.

[41] J. R. Jastifer and P. A. Gustafson, "The subtalar joint: Biomechanics and functional representations in the literature," *Foot*. 2014.

[42] J. M. Michael, A. Golshani, S. Gargac, and T. Goswami, "Biomechanics of the ankle joint and clinical outcomes of total ankle replacement," *Journal of the Mechanical Behavior of Biomedical Materials*. 2008.

[43] F. H. Netter, *Atlas of Human Anatomy*, 6th ed. Elsevier SAUNDERS, 2014.

[44] G. J. M. Tuijthof, L. Beimers, G. M. M. J. Kerkhoffs, J. Dankelman, and C. N. van Dijk, "Overview of subtalar arthrodesis techniques: Options, pitfalls and solutions," *Foot and Ankle Surgery*. 2010.

[45] M. J. Silva, L. J. Gibson, and M. J. Silva, “Modeling the Mechanical Behavior of Vertebral Trabecular Bone: Effects of Age-Related Changes in Microstructure,” 1997.

[46] Y. Tanaka, S. Kokubun, T. Sato, M. Iwamoto, and I. Sato, “Trabecular domain factor and its influence on the strength of cancellous bone of the vertebral body,” *Calcif. Tissue Int.*, 2001.

[47] W. X. Niu, L. J. Wang, T. N. Feng, C. H. Jiang, Y. B. Fan, and Y. B. Fan, “Effects of bone Young’s modulus on finite element analysis in the lateral ankle biomechanics,” *Appl. Bionics Biomech.*, 2013.

[48] B. Van Rietbergen, H. Weinans, R. Huiskes, and A. Odgaardt, “A New Method To Determine Trabecular Bone Elastic Properties And Loading Using Micromechanical Finite-Element Models,” 1995.

[49] B. Van Rietbergen, A. Odgaard, J. Kabel, and R. Huiskes, “Relationships between Bone Morphology and Bone Elastic Properties can be Accurately Quantified using High - Resolution Computer Reconstructions.,” *J. Orthop. Res.*, vol. 16, pp. 23–28, 1998.

[50] M. De Berg, O. Cheong, M. Van Kreveld, and M. Overmars, *Computational Geometry (Algorithms and Applications)*, Third Edition. Springer, 2008.

[51] I. H. Parkinson and N. L. Fazzalari, “Characterisation of Trabecular Bone Structure,” 2013.

[52] C. J. Hernandez, “Cancellous bone,” in *Handbook of Biomaterial Properties, Second Edition*, 2016.

[53] M. Brickley and P. G. T. Howell, “Measurement of Changes in Trabecular Bone Structure with Age in an Archaeological Population,” *J. Archaeol. Sci.*, vol. 26, pp. 151–157, 1999.

[54] M Dalstra, R. Huiskes, A. Odgaard, and L. van Erning, “Mechanical and textural properties of pelvic trabecular bone,” *J. Biomech.*, vol. 26, no. 4/5, pp. 523–535, 1993.

APPENDICES

A1. Mechanical properties correlations with (apparent density, No. of trabeculae, length of trabeculae)

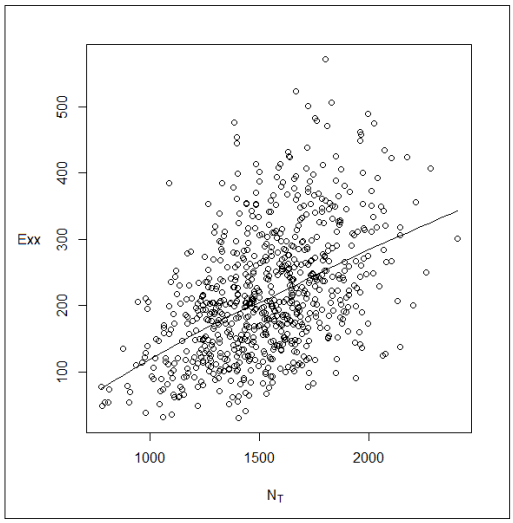

A1.1: Identified distributions of E_{xx} and its relationship to No. of trabeculae (N_T)

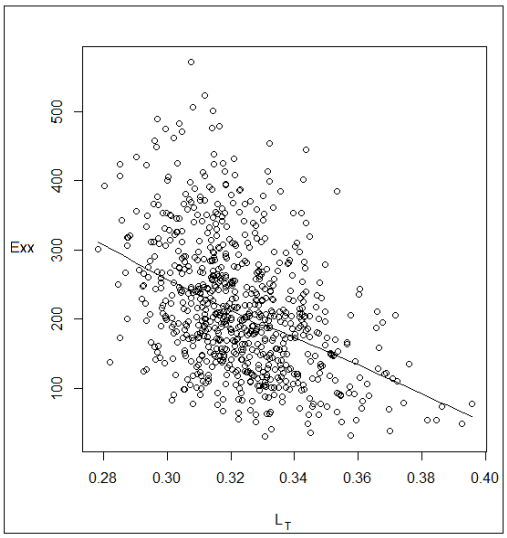

A1.2: Identified distributions of E_{xx} and its relationship to length of trabeculae (L_T)

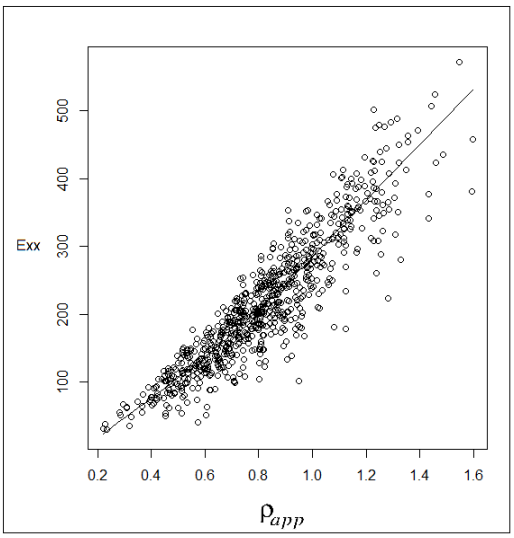

A1.3: Identified distributions of E_{xx} and its relationship to apparent density (ρ_{app})

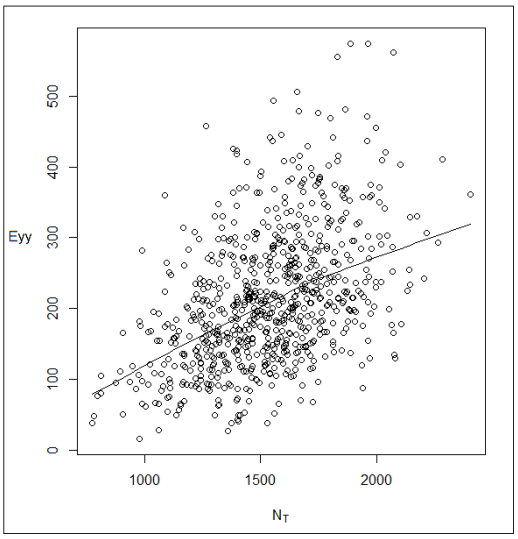

A1.4: Identified distributions of E_{yy} and its relationship to No. of trabeculae (N_T)

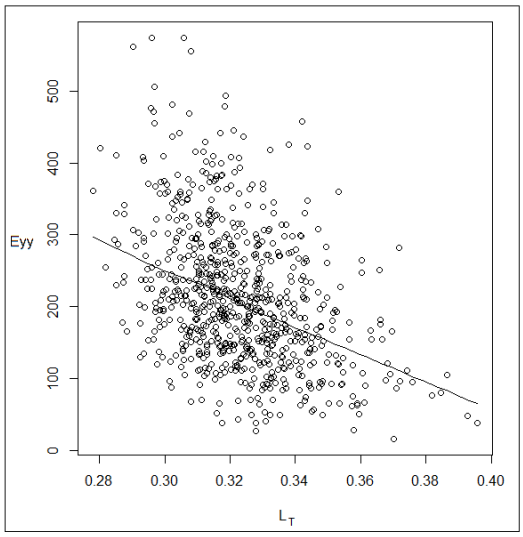

A1.5: Identified distributions of E_{yy} and its relationship to length of trabeculae (L_T)

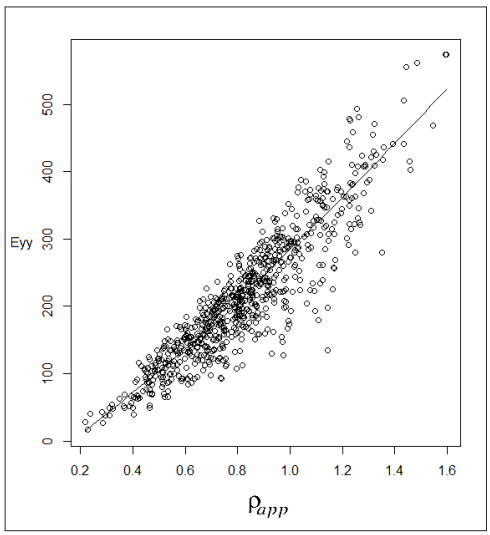

A1.6: Identified distributions of E_{yy} and its relationship to apparent density (ρ_{app})

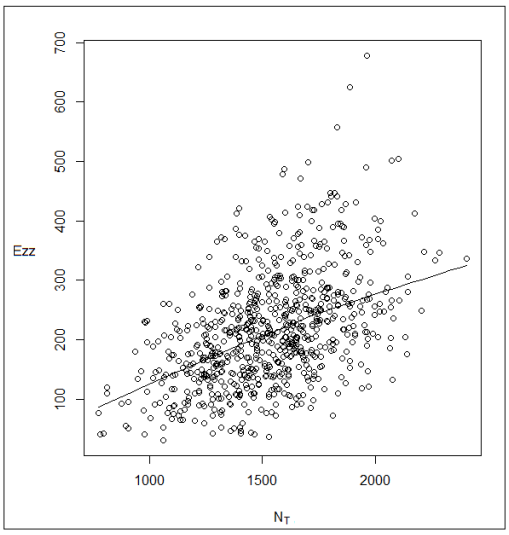

A1.7: Identified distributions of E_{zz} and its relationship to No. of trabeculae (N_T)

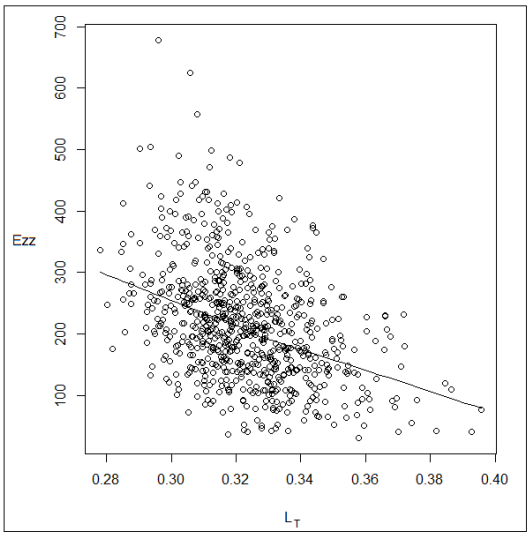

A1.8: Identified distributions of E_{zz} and its relationship to length of trabeculae (L_T)

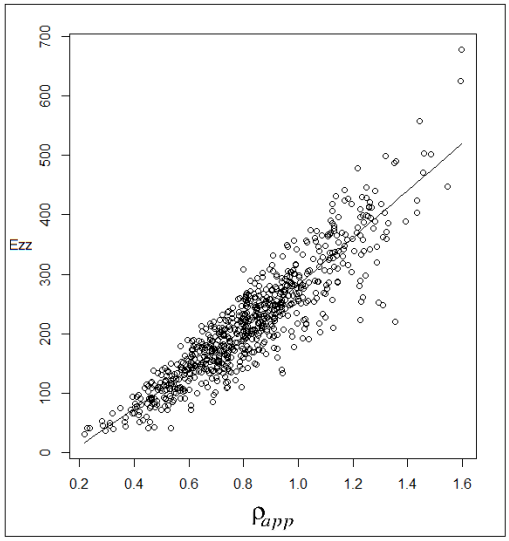

A1.9: Identified distributions of E_{zz} and its relationship to apparent density (ρ_{app})

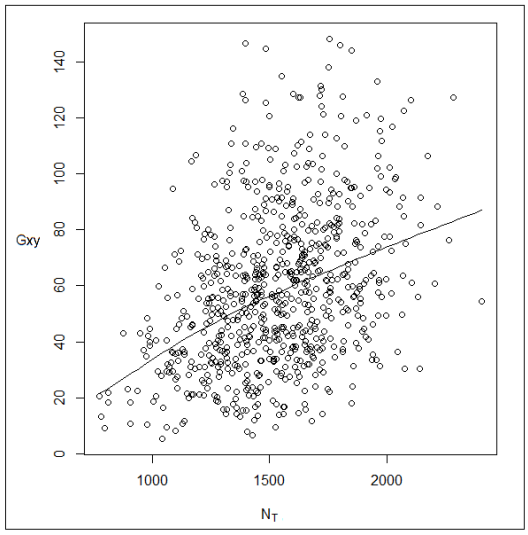

A1.10: Identified distributions of G_{xy} and its relationship to No. of trabeculae (N_T)

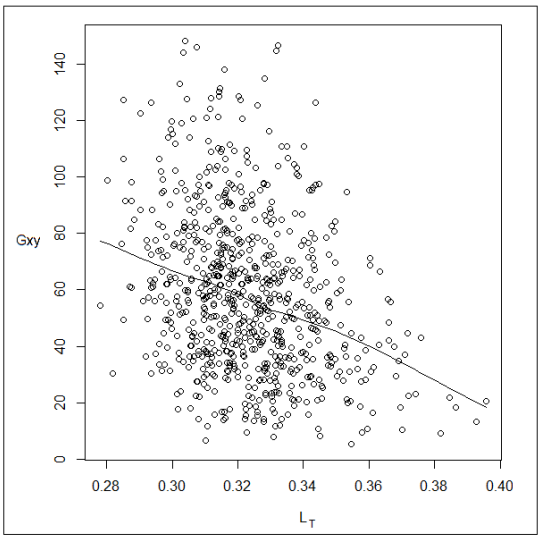

A1.11: Identified distributions of G_{xy} and its relationship to length of trabeculae (L_T)

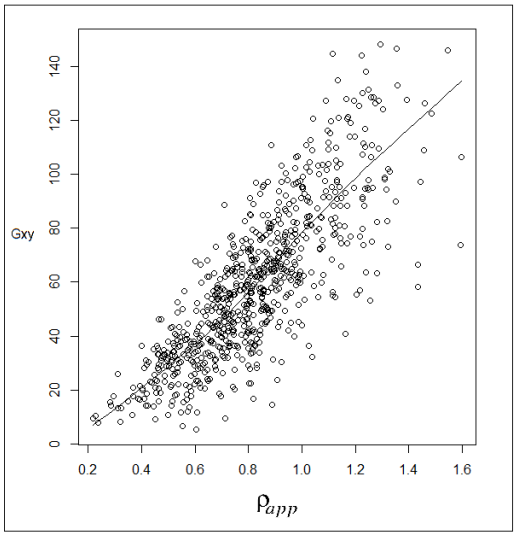

A1.12: Identified distributions of G_{xy} and its relationship to apparent density (ρ_{app})

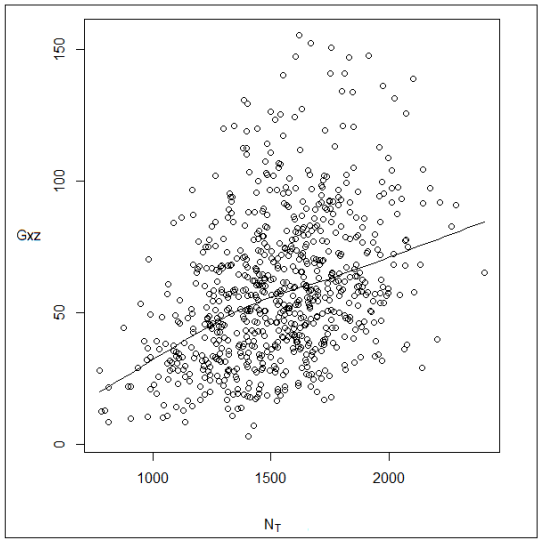

A1.13: Identified distributions of G_{xz} and its relationship to No. of trabeculae (N_T)

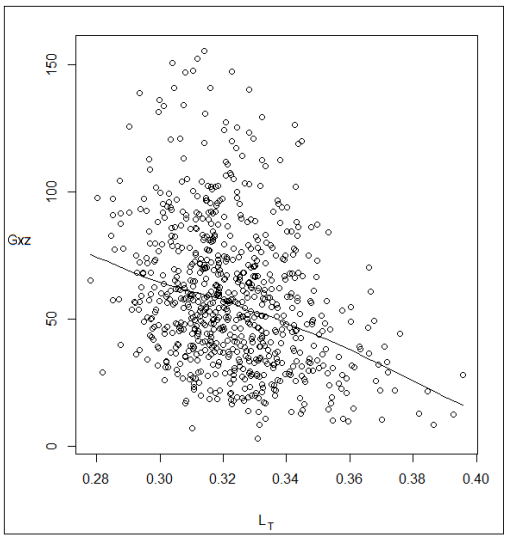

A1.14: Identified distributions of G_{xz} and its relationship to length of trabeculae (L_T)

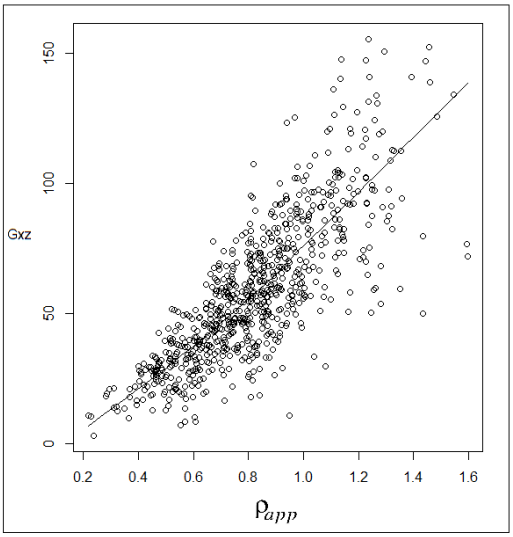

A1.15: Identified distributions of G_{xz} and its relationship to apparent density (ρ_{app})

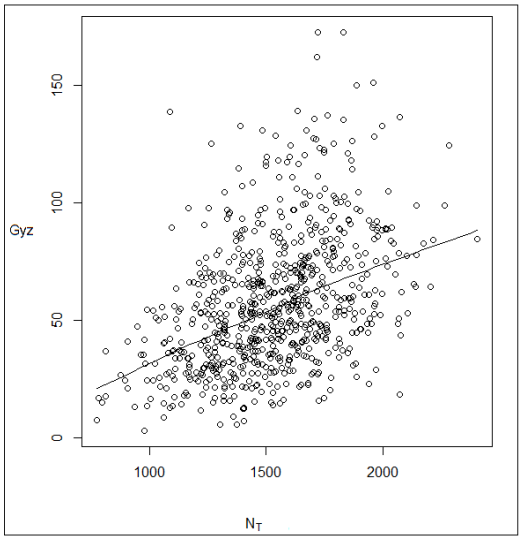

A1.16: Identified distributions of G_{yz} and its relationship to No. of trabeculae (N_T)

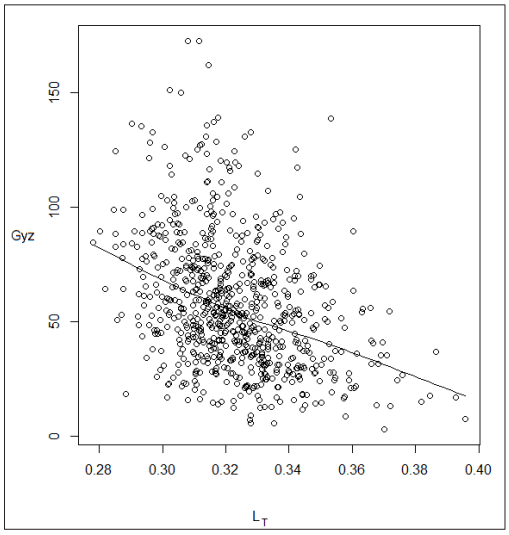

A1.17: Identified distributions of G_{yz} and its relationship to length of trabeculae (L_T)

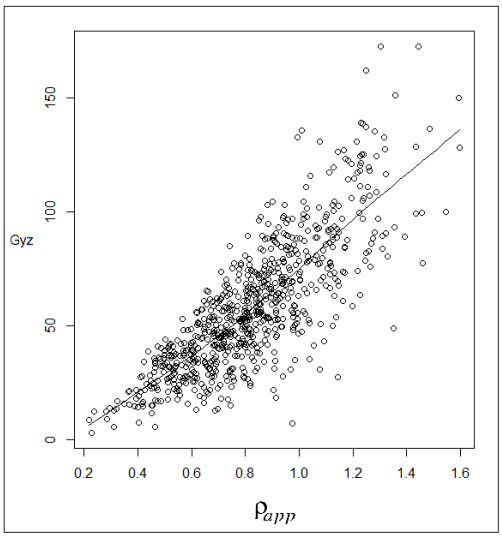

A1.18: Identified distributions of G_{yz} and its relationship to apparent density (ρ_{app})

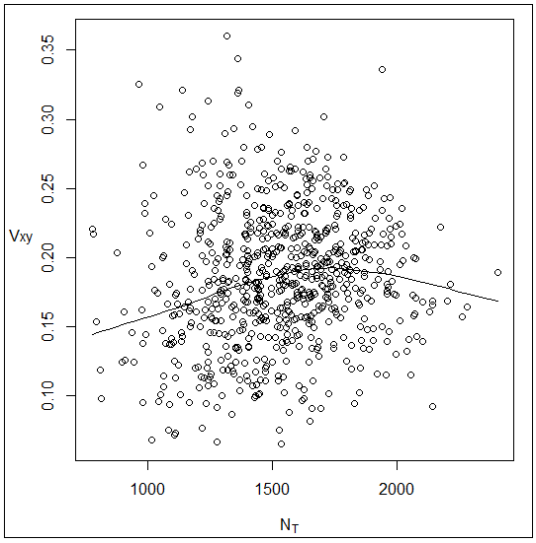

A1.19: Identified distributions of ν_{xy} and its relationship to No. of trabeculae (N_T)

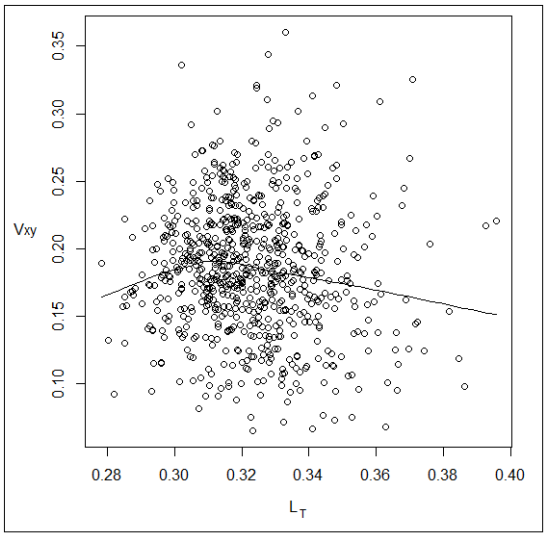

A1.20: Identified distributions of ν_{xy} and its relationship to length of trabeculae (L_T)

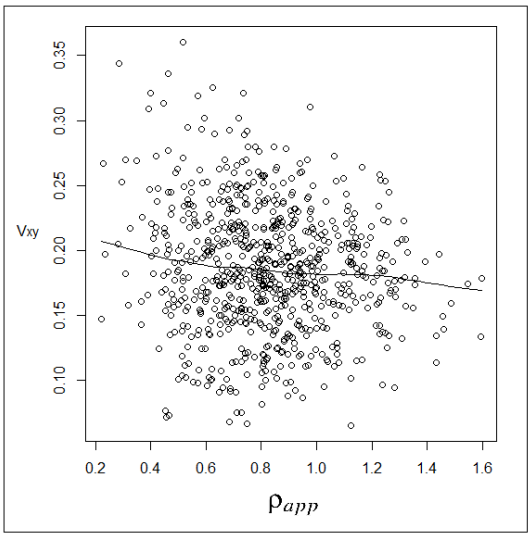

A1.21: Identified distributions of ν_{xy} and its relationship to apparent density (ρ_{app})

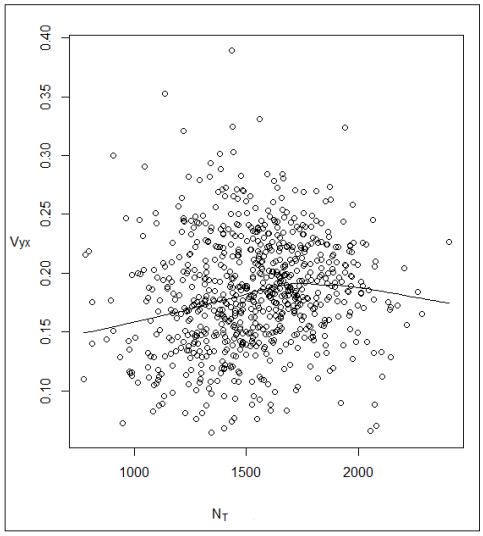

A1.22: Identified distributions of ν_{yx} and its relationship to No. of trabeculae (N_T)

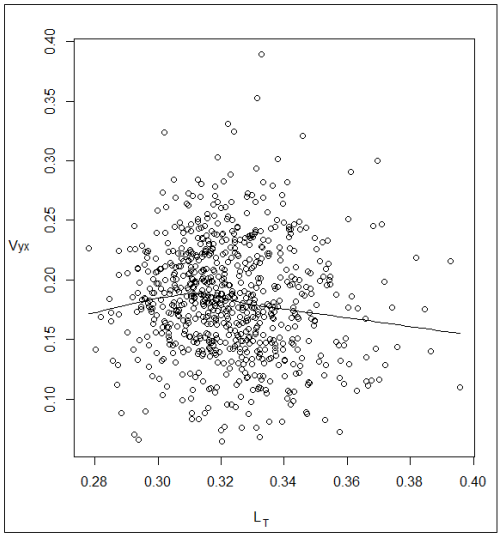

A1.23: Identified distributions of ν_{yx} and its relationship to length of trabeculae (L_T)

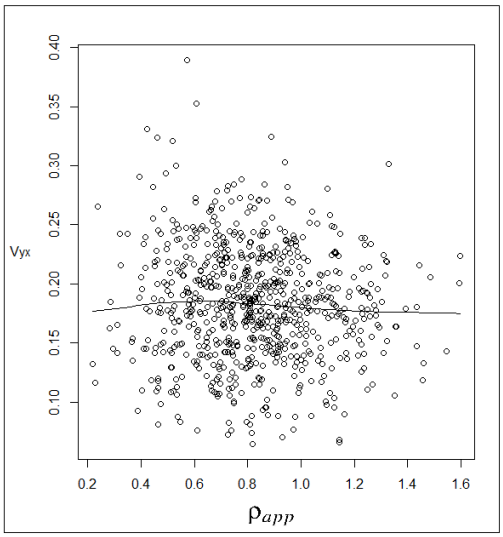

A1.24: Identified distributions of ν_{yx} and its relationship to apparent density (ρ_{app})

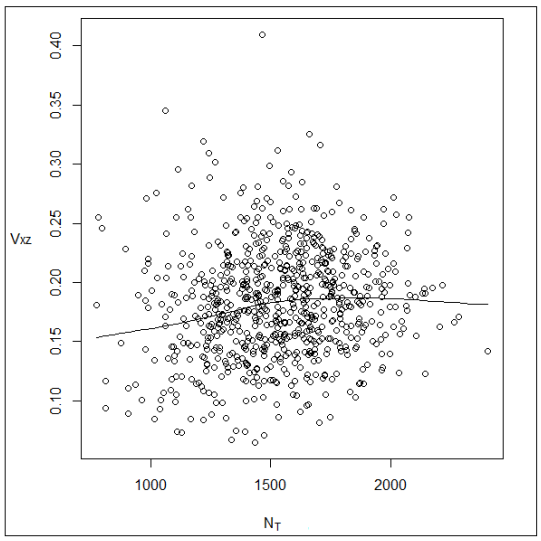

A1.25: Identified distributions of ν_{xz} and its relationship to No. of trabeculae (N_T)

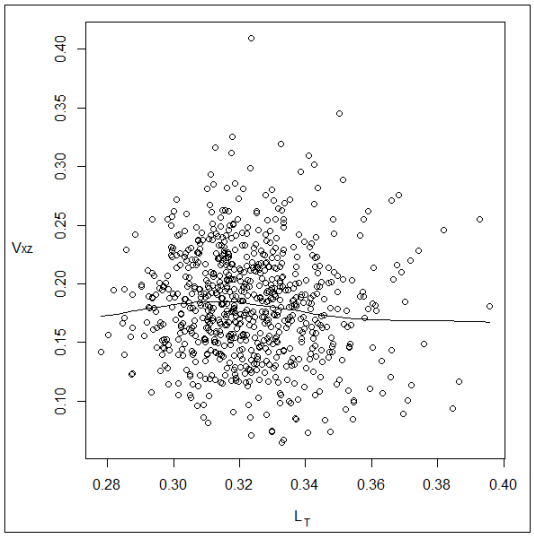

A1.26: Identified distributions of ν_{xz} and its relationship to length of trabeculae (L_T)

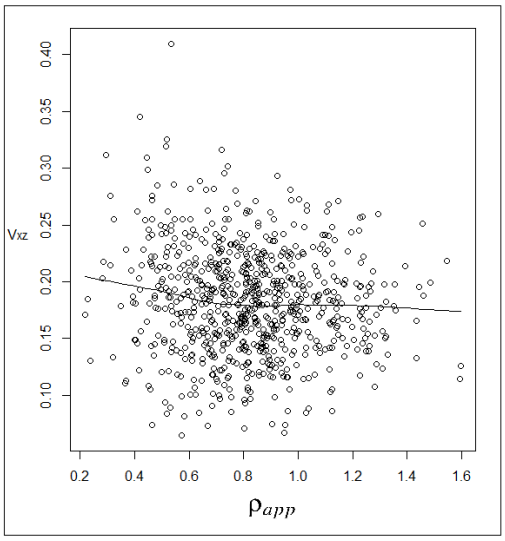

A1.27: Identified distributions of ν_{xz} and its relationship to apparent density (ρ_{app})

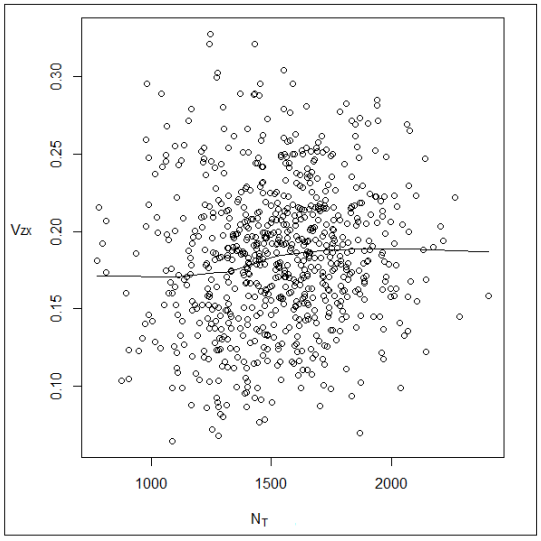

A1.28: Identified distributions of ν_{zx} and its relationship to No. of trabeculae (N_T)

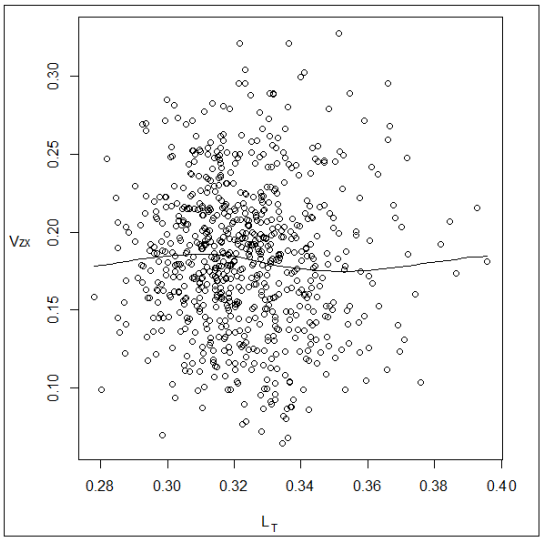

A1.29: Identified distributions of ν_{zx} and its relationship to length of trabeculae (L_T)

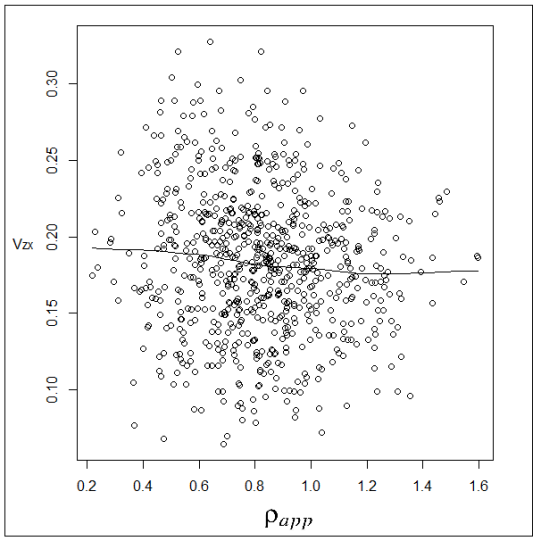

A1.30: Identified distributions of ν_{zx} and its relationship to apparent density (ρ_{app})

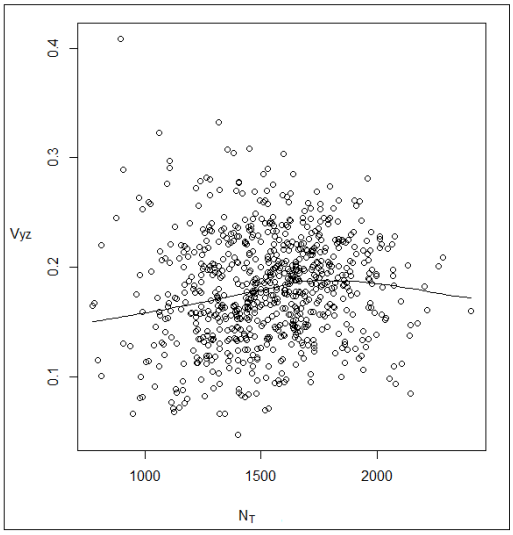

A1.31: Identified distributions of ν_{yz} and its relationship to No. of trabeculae (N_T)

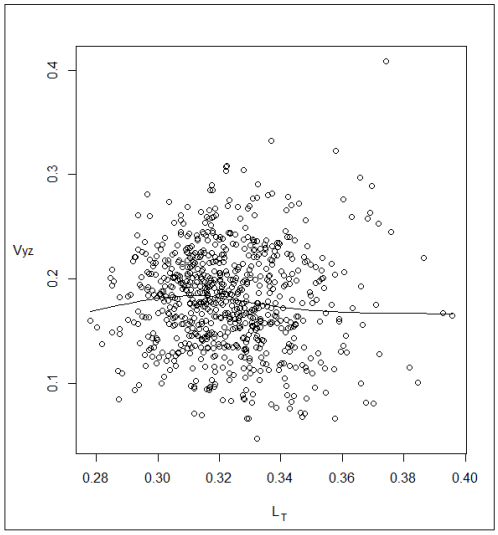

A1.32: Identified distributions of ν_{yz} and its relationship to length of trabeculae (L_T)

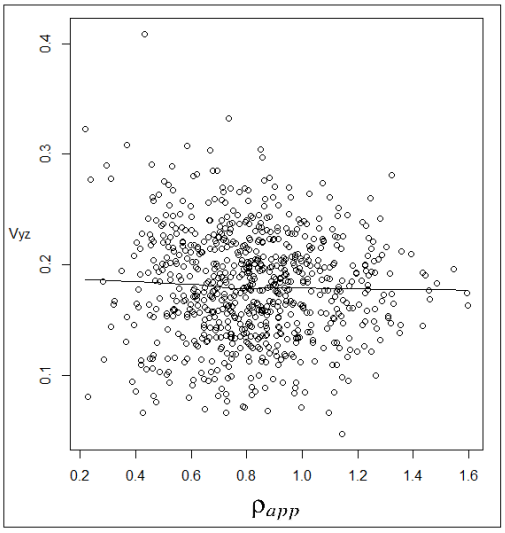

A1.33: Identified distributions of ν_{yz} and its relationship to apparent density (ρ_{app})

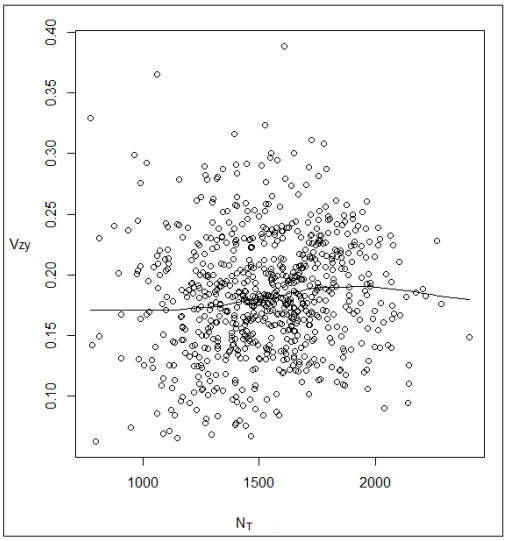

A1.34: Identified distributions of ν_{zy} and its relationship to No. of trabeculae (N_T)

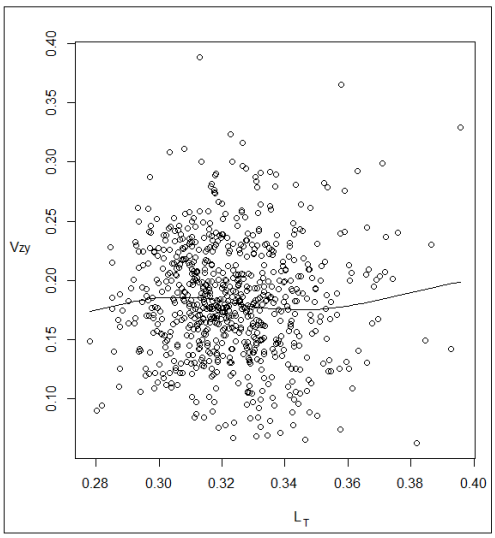

A1.35: Identified distributions of ν_{zy} and its relationship to length of trabeculae (L_T)

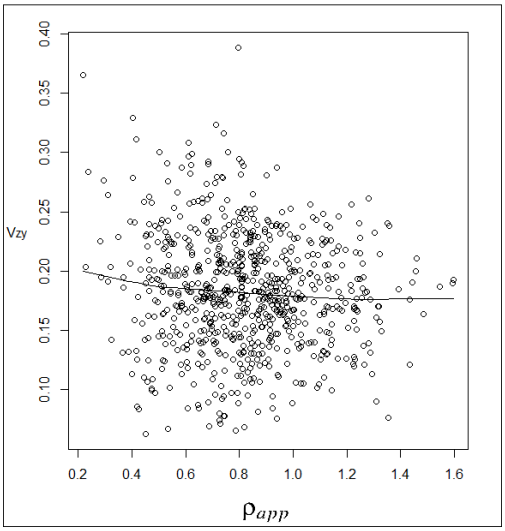

A1.36: Identified distributions of ν_{zy} and its relationship to apparent density (ρ_{app})

A2. Regression analysis summary

A.2.1: Model Input Parameters – Intermediate Parameters

Response ρ_{app}:
$\rho_{app} \sim$ -7.010e-01 + 3.546e-03 N_S + 1.508e+01 A_T
P-value: <2e-16
Adjusted R-squared: 0.978

Response N_T:
$N_T \sim$ -334.46101 + 9.25909 N_S + 79.84583 A_T
P-value: <2e-16
Adjusted R-squared: 0.969

Response L_T:
$L_T \sim$ 4.412e-01 -5.859e-04 N_S -1.377e-02 A_T
P-value: <2e-16
Adjusted R-squared: 0.8633

A.2.2: Intermediate Parameters – Model Output Parameters

Response E_{xx}:
$E_{xx} \sim$ -572.29201 + 344.88717 ρ_{app} - 0.09938 N_T + 1094.62232 L_T
P-value: <2e-16
Adjusted R-squared: 0. 8381

Response E_{yy}:
$E_{yy} \sim$ -570.57273 + 347.66127 ρ_{app} + 0.09669 N_T +1088.35485 L_T
P-value: <2e-16
Adjusted R-squared: 0. 8318

Response E_{zz}:
$E_{zz} \sim$ -678.91995 + 342.30345 ρ_{app} + 0.11653 N_T + 1351.97368 L_T
P-value: <2e-16
Adjusted R-squared: 0. 8366

Response G_{yz}:
$G_{yz} \sim$ -2.219e+02 + 9.138e+01 ρ_{app} + 3.787e-02 N_T + 4.554e+02 L_T
P-value: <2e-16
Adjusted R-squared: 0. 6642

Response G_{xz}:
$G_{xz} \sim$ -2.378e+02 + 9.071e+01 ρ_{app} + 3.608e-02 N_T + 5.159e+02 L_T

P-value: <2e-16
Adjusted R-squared: 0. 6479

Response G_{xy}:
$G_{xy} \sim$ -2.554e+02 + 9.352e+01 ρ_{app} + 3.804e-0 N_T + 5.559e+02 L_T
P-value: <2e-16
Adjusted R-squared: 0. 6668

Response ν_{xy}:
$\nu_{xy} \sim$ -2.750e-01 -4.345e-02 ρ_{app} + 1.021e-04 N_T + 1.054e+00 L_T
P-value: <2e-16
Adjusted R-squared: 0. 05901

Response ν_{yx}:
$\nu_{yx} \sim$ -3.243e-01 -3.210e-02 ρ_{app} + 1.077e-04 N_T + 1.143e+00 L_T
P-value: <2e-16
Adjusted R-squared: 0. 05274

Response ν_{xz}:
$\nu_{xz} \sim$ -3.620e-01 -3.599e-02 ρ_{app} + 1.117e-04 N_T + 1.249e+00 L_T
P-value: <2e-16
Adjusted R-squared: 0. 05832

Response ν_{zx}:
$\nu_{zx} \sim$ -4.860e-01 -3.500e-02 ρ_{app} + 1.290e-04 N_T + 1.551e+00 L_T
P-value: <2e-16
Adjusted R-squared: 0. 06826

Response ν_{zy}:
$\nu_{zy} \sim$ -5.706e-01 -3.645e-02 ρ_{app} + 1.414e-04 N_T + 1.757e+00 L_T
P-value: <2e-16
Adjusted R-squared: 0. 07438

Response ν_{yz}:
$\nu_{yz} \sim$ -5.235e-01 -2.665e-02 ρ_{app} + 1.316e-04 N_T + 1.624e+00 L_T
P-value: <2e-16
Adjusted R-squared: 0. 05829

Response AIratio:
AIratio ~ 3.2525170 -0.1062181 ρ_{app} -0.0004431 N_T -3.3073872 L_T
P-value: <2e-16
Adjusted R-squared: 0. 05752

B. Trabecular bone representative models